

DISS. ETH NO. 20917

**CUTTING-EDGE HIGH-POWER ULTRAFAST OSCILLATORS:
PUSHING THE LIMITS OF SESAM MODELOCKED THIN-DISK LASERS**

A dissertation submitted to

ETH ZURICH

for the degree of

Doctor of Sciences

presented by

CLARA JODY SARACENO

Diplôme d'Ingénieur, Institut d'Optique Graduate School (Palaiseau, France)

born on September 13, 1983

citizen of

Argentina, Italy, and United States of America

accepted on the recommendation of

Prof. Dr. U. Keller, Supervisor

Prof. Dr. P. Georges, Co-Examiner

Prof. Dr. T. Südmeyer, Co-Examiner

December 2012

Table of Contents

<i>List of Figures</i>	V
<i>List of Tables</i>	IX
<i>List of Abbreviations</i>	X
<i>List of Symbols</i>	XIII
<i>List of Publications</i>	XIV
<i>Abstract</i>	XXI
<i>Résumé</i>	XXIV
Chapter 1 - Introduction	1
Chapter 2 - Modelocked high-power thin-disk lasers: challenges and milestones	7
2.1 Thin-disk laser technology	8
2.1.1 Thermal management: the key for high-power operation	8
2.1.2 Power scaling of transverse fundamental mode thin-disk lasers	11
2.1.3 Gain materials: thermo-mechanical and spectroscopic properties	16
2.2 Soliton modelocking of solid-state lasers using SESAMs	18
2.2.1 Soliton modelocking with slow saturable absorbers	19
2.2.2 Q-switched modelocking vs. cw modelocking	22
2.2.3 Semiconductor saturable absorber mirrors	23
2.3 Challenges for high-power modelocking	26
2.3.1 Q-switching instabilities	26
2.3.2 Excessive nonlinearities	27
2.3.3 Thermal effects and damage	30
2.4 Outlook	31
Chapter 3 - SESAMs for high-power femtosecond oscillators	33
<i>Part I - Damage thresholds, lifetime and design guidelines</i>	<i>36</i>
3.1 Experimental setup and SESAM characterization	36
3.1.1 Experimental Setup	36
3.1.2 Characterization of the nonlinear reflectivity parameters	37
3.1.3 Importance of the induced absorption coefficient F_2	37
3.2 Design of the SESAMs under test	39
3.2.1 SESAM structures grown for damage investigations	40
3.2.2 Topcoating section	41

3.3	Nonlinear reflectivity, damage thresholds and lifetimes.....	42
3.3.1	Nonlinear reflectivity	42
3.3.2	Damage fluence and time-to-damage measurement procedure	44
3.3.3	Damage threshold measurements	46
3.3.4	Lifetime measurements	47
3.3.5	Extension of lifetime curves to lower fluences	48
3.4	Damage mechanism	50
3.4.1	Influence of the absorber section on the lifetime.....	50
3.4.2	Approximate expression of the energy absorbed by IA	51
3.4.3	Experimental verification	52
3.5	Guidelines for SESAMs with high damage thresholds.	54
<i>Part II - Influence of nonsaturable losses and absorber growth temperature on damage</i>		56
3.1	Experimental setup and structures used for this study.....	57
3.1.1	Experimental setup.....	57
3.1.2	Structure used for this study	59
3.2	Experimental results	60
3.2.1	Influence of growth temperature on recovery parameters and damage threshold	60
3.2.2	Topcoated sample for use in high-power thin-disk laser	63
3.2.3	Comparison with previous uncoated SESAM with similar parameters	64
3.3	Additional guidelines for high damage threshold SESAMs with fast recovery times.....	65
<i>Part III - Summary and outlook</i>		67
3.1	Summary and guidelines for SESAMs with high damage thresholds ...	67
3.2	Outlook: future SESAM designs	68
3.2.1	More QWs, more layers for the topcoatings	68
3.2.2	QW absorbers embedded in AIAs	70
3.3	Novel mirror structures	71
3.3.1	Upside-down growth of large-scale SESAMs for improved thermal management	71
Chapter 4 - New pulse duration limits of modelocked thin-disk lasers		73
4.1	Broadband materials for high-power thin-disk lasers.....	74
4.1.1	State-of-the art	74
4.1.2	Sesquioxide materials for efficient high-power operation	78
4.2	Short pulses from Yb:LuO	80
4.2.1	Yb:LuO : a promising candidate for outperforming Yb:YAG ...	80
4.2.2	Yb:LuO modelocked thin-disk laser with 7 W, 142 fs [85]	82

4.2.3	Power scaling to 25 W, 185 fs	85
4.3	Short pulses from Yb:LuScO	88
4.3.1	Mixed cubic sesquioxide Yb:LuScO	88
4.3.2	High-power modelocked Yb:LuScO thin-disk laser	89
4.3.3	Sub-100 Yb:LuScO thin disk laser [40]	92
4.4	Short pulses from Yb:ScYLO.....	94
4.5	Summary and discussion	96
Chapter 5 - Carrier-envelope offset frequency detection of a modelocked thin-disk laser.....		100
5.1	Towards high-harmonic generation inside a thin-disk laser	101
5.2	Frequency combs and carrier-envelope offset frequency detection	102
5.2.1	Frequency combs	102
5.2.2	Carrier-envelope frequency detection schemes: f-to-2f interferometer.....	104
5.2.3	Supercontinuum generation and coherence properties	106
5.2.4	High-power frequency combs	107
5.3	Carrier-envelope frequency of a modelocked thin-disk laser	108
5.3.1	Experimental Setup	108
5.3.2	Results	109
5.3.3	Towards full stabilization of high-power thin-disk lasers	111
Chapter 6 - Average power scaling of modelocked thin-disk lasers		113
6.1	Harnessing intracavity nonlinearity	114
6.1.1	State-of-the-art: different suggested approaches	114
6.1.2	Oscillator in vacuum	116
6.2	High-power fundamental mode cavity.....	117
6.3	Femtosecond modelocked oscillator with 275 W of average power	118
6.3.1	Experimental Setup	118
6.3.2	SESAM design	120
6.3.3	Results	121
6.4	Discussion	122
6.4.1	Sources of nonlinearity	122
6.4.2	Mode degeneracies and beam quality degradation	123
6.5	Conclusion and outlook	130
Chapter 7 - Pulse compression of modelocked thin-disk lasers		132
7.1	Pulse compression of modelocked thin-disk lasers using rod-type fiber amplifiers	134
7.1.1	Seed laser used for both experimental setups.....	134
7.1.2	First amplifier system: 55-cm rod	135
7.1.3	Second stretcher-free amplifier system: 36-cm rod	140
7.1.4	Discussion on further scaling of these systems.....	144

Table of Contents

7.1.5	Summary and outlook.....	147
7.2	Pulse compression of modelocked thin-disk lasers using gas-filled hollow-core photonics-crystal fibers	149
7.2.1	Experimental setup.....	150
7.2.2	Experimental results	152
7.3	Conclusion and outlook	154
Chapter 8 -	Conclusion	156
<i>References</i>	158
<i>Curriculum Vitæ</i>	167

List of Figures

Figure 1.1:	Evolution of average power and pulse duration of modelocked thin disk lasers in the last 12 years.	4
Figure 1.2:	Pulse duration of modelocked TDLs versus their average power.	5
Figure 2.1:	Schematic of cooling scheme of thin-disk gain medium.	8
Figure 2.2:	Simulation of surface temperature of an Yb:YAG thin disk	9
Figure 2.3:	Multiple pump pass geometry of a thin-disk laser.	10
Figure 2.4:	Resonator stability zones for different laser spot diameters.	13
Figure 2.5:	Influence of different heatsinks and different thermal conductivity of the gain medium on the temperature profile of the disk.	14
Figure 2.6:	Comparison of thermal lensing of different disks.	15
Figure 2.7:	Schematic of a typical SESAM.	19
Figure 2.8:	Absorber stabilization mechanism in soliton modelocked lasers.	21
Figure 2.9:	Different regimes of pulsed operation.	22
Figure 2.10:	Typical nonlinear reflectivity response of a SESAM, and important macroscopic parameters.	24
Figure 2.11:	Typical layout of a modelocked thin-disk laser.	27
Figure 2.12:	Stability zones of resonators with increasing number of passes through the thin-disk gain medium.	32
Figure 3.1:	Nonlinear reflectivity characterization setup.	36
Figure 3.2:	Influence of F_2 parameter on nonlinear reflectivity.	39
Figure 3.3:	SESAM structure with no topcoating used for the damage study.	41
Figure 3.4:	Different SESAM structures used for the damage study.	42
Figure 3.5:	Nonlinear reflectivity measurement of different topcoated samples used for the damage study	43
Figure 3.6:	Typical time-to-damage measurement.	45
Figure 3.7:	Damage thresholds of the different SESAMs, together with their nonlinear reflectivity.	46

List of Figures

Figure 3.8:	Lifetime curves of different SESAMs.	47
Figure 3.9:	SESAM lifetime extended to low saturation parameters.	49
Figure 3.10:	Nonlinear reflectivity and lifetime curves of a DBR and SESAMs with 1 and 3 QWs.	50
Figure 3.11:	Ratio F_d/F_0 for samples with same absorber section.	52
Figure 3.12:	Ratio $\sqrt{F_2}/F_0$ for samples with different absorber sections.....	53
Figure 3.13:	Influence of pulse duration on SESAM nonlinear reflectivity response.....	57
Figure 3.14:	Pump-probe setup.	58
Figure 3.15:	SESAM structure used for the study of the influence of growth temperature on damage.	59
Figure 3.16:	Recovery time measurements.	60
Figure 3.17:	Influence of different recovery parameters with absorber growth temperature.	61
Figure 3.18:	Dependence of damage threshold and nonsaturable losses on absorber growth temperature.	62
Figure 3.19:	Influence of topcoating on nonlinear reflectivity of fastest sample.	63
Figure 3.20:	Nonlinear reflectivity of two samples with similar saturation parameters. ...	65
Figure 3.21:	Fabrication steps for upside-down SESAMs.	72
Figure 4.1:	Thermal conductivity of different gain materials used in modelocked thin-disk lasers and overview of pulse duration versus average power	75
Figure 4.2:	Cross-sections of Yb:LuO and Yb:YAG.	81
Figure 4.3:	Laser setup for the Yb:LuO thin-disk laser with 7W and 142 fs.....	82
Figure 4.4:	SESAM linear reflectivity versus wavelength for different temperatures.	83
Figure 4.5:	SESAM nonlinear reflectivity for different temperatures	83
Figure 4.6:	Autocorrelation and spectrum of the pulses for the 7-W, 142 fs Yb:LuO modelocked laser.....	85
Figure 4.7:	Laser setup for the Yb:LuO thin-disk laser with 25 W and 185 fs	86
Figure 4.8:	Autocorrelation and spectrum of the pulses for the 25-W, 185-fs Yb:LuO modelocked laser.....	87

Figure 4.9:	Emission cross-section of Yb:LuScO	88
Figure 4.10:	Output power slopes in CW operation	89
Figure 4.11:	Laser setup for the Yb:LuScO thin-disk laser with 23 W and 235 fs.....	91
Figure 4.12:	Autocorrelation and spectrum of the pulses for the 23-W, 235 fs Yb:LuScO modelocked laser	91
Figure 4.13:	Laser setup for the Yb:LuScO thin-disk laser with 5 W and 96 fs.....	93
Figure 4.14:	Autocorrelation and spectrum of the pulses for the 5-W, 96 fs Yb:LuScO modelocked laser.....	94
Figure 4.15:	Emission cross-section of Yb:ScYLO.....	95
Figure 4.16:	Autocorrelation and spectrum of the pulses for the 5-W, 101 fs Yb:ScYLO modelocked laser.....	96
Figure 4.17:	Emission bandwidth and modelocked spectrum of shortest achieved pulses for different gain materials	98
Figure 4.18:	Effect of inversion level on gain cross section of Yb:LuO and Yb:LuScO	98
Figure 5.1:	Intralaser HHG.	102
Figure 5.2:	Frequency combs.	103
Figure 5.3:	f -to- $2f$ carrier-envelope offset frequency detection scheme.	105
Figure 5.4:	Beat signals observed in f -to- $2f$ interferometer detection.....	105
Figure 5.5:	Setup and performance of thin-disk laser system used for carrier-envelope frequency detection experiment.....	108
Figure 5.6:	Experimental results: octave-spanning super-continuum and carrier- envelope offset frequency beats.	109
Figure 6.1:	Schematic of the cavity for the Yb:YAG thin-disk laser delivering 427 W in cw fundamental-mode operation.....	117
Figure 6.2:	Cw results obtained with high-power Yb:YAG system.	118
Figure 6.3:	Schematic of the cavity for the Yb:YAG thin-disk laser delivering 275 W and 583 fs	119
Figure 6.4:	Beam quality and cw performance of thin-disk laser used for the modelocking experiment.	119
Figure 6.5:	High-damage threshold, large-scale SESAM designed for high-power modelocking.	121

List of Figures

Figure 6.6:	Vacuum chamber.....	121
Figure 6.7:	Autocorrelation and spectrum of the pulses at the maximum power of 275 W.	122
Figure 6.8:	Effect of thermal lensing on the spot sizes throughout the cavity used for the 275 W modelocked laser.....	127
Figure 6.9:	Gouy phase versus intracavity power for cavities with different thermal loads.	128
Figure 6.10:	Intracavity peak power versus pulse duration of modelocked thin-disk lasers.	130
Figure 7.1:	Experimental layout of the first rod-type fiber based compression setup.	135
Figure 7.2:	Influence of the input chirp of the pulses on the compression system. ..	136
Figure 7.3:	Power slope and observed spectral broadening in the first compression setup.	137
Figure 7.4:	Retrieved compressed pulses using SHG FROG (first setup).	138
Figure 7.5:	Experimental layout of the second stretcher-free compression setup. ..	140
Figure 7.6:	Power slope and observed spectral broadening in the second stretcher-free compression setup.	141
Figure 7.7:	Retrieved compressed pulses using SHG FROG (second stretcher-free setup).	143
Figure 7.8:	Simulations towards higher peak powers.	147
Figure 7.9:	Experimental layout of the gas-filled HC-PCF compression setup.	151
Figure 7.10:	Spectral broadening observed after the Xenon-filled HC-PCF	153
Figure 7.11:	Retrieved compressed pulses using SHG FROG (Xenon-filled HC-PCF setup)	154

List of Tables

Table 3.I:	Typical operation points of SESAMs in high-power TDLs.	34
Table 3.II:	Saturation parameters of SESAMs used for the damage study.	42
Table 3.III:	Comparison between measured and calculated F_2 coefficient.....	44
Table 3.IV:	Damage thresholds of different SESAMs used for the damage study.	46
Table 3.V:	Lifetime curve fit parameters.	48
Table 3.VI:	Nonlinear reflectivity fit parameters and damage thresholds of samples with different absorber sections.	50
Table 3.VII:	Recovery parameters of representative SESAMs.....	60
Table 3.VIII:	Nonlinear reflectivity, recovery and damage parameters of the sample with fastest recovery time.	64
Table 3.IX:	Comparison of nonlinear reflectivity, recovery and damage parameters of two samples with similar saturation parameters.	65
Table 4.I:	Parameter overview of modelocked thin-disk lasers demonstrated to date.	76
Table 4.II:	Important material properties of sesquioxide materials for modelocked thin-disk lasers.....	78
Table 4.III:	Results of cw multimode experiments performed with sesquioxide materials.	79
Table 4.IV:	Summary of results obtained during this thesis in the context of short pulse generation from modelocked thin-disk lasers.	96
Table 7.I:	Retrieved pulse parameters with first rod-type fiber amplifier based compression setup.	138
Table 7.II:	Retrieved pulse parameters with second stretcher-free rod-type fiber amplifier based compression setup.	143
Table 7.III:	Operation points at maximum output power and reported damage thresholds.	144
Table 7.IV:	Summary of results obtained with the two rod-type fiber amplifier compression setups.	147

List of Abbreviations

$^{\circ}\text{C}$	degree Celsius
AOM	acousto optic modulator
AIAs	aluminum arsenide
AR	anti-reflective
at. %	atomic percent
β_{TPA}	two-photon absorption coefficient
CALGO	calcium gadolinium aluminum oxide (CaGdAlO_4)
CEO	carrier-envelope offset
CPA	chirped pulse amplification
cw	continuous wave
d	thickness
D	dispersion
DBR	distributed Bragg reflector
DPSSL	diode-pumped solid-state laser
E_p	pulse energy
$E_{\text{sat,A}}$	saturation energy of the absorber
$E_{\text{sat,L}}$	saturation energy of the laser
F_0	rollover fluence
F	fluence
F_2	induced absorption coefficient
f_{rep}	repetition rate
FROG	frequency resolved optical gating
fs	femtosecond
F_{sat}	saturation fluence of absorber
$F_{\text{sat,L}}$	pulse fluence on absorber
F_t	transparency fluence
FWHM	full-width half maximum
g	gain
GaAs	gallium arsenide
GDD	group delay dispersion
GW	gigawatt
h	Planck's constant
HC-PCF	hollow-core photonic crystal fiber
He	helium
HEM	heat exchanger method
HHG	high harmonic generation
HR	highly-reflective
IA	induced absorption

I_{abs}	absorbed intensity
I_{inc}	incident intensity
I_{pk}	peak intensity
InGaAs	indium gallium arsenide
J	Joule
K	Kelvin
kHz	kilohertz
KLM	Kerr-Lens mode locking
KYW	potassium yttrium tungstate ($\text{KY}(\text{WO}_4)_2$)
kW	kilowatt
L	length
LT	low temperature ($< 400^\circ\text{C}$)
LuO	lutetium oxide (Lu_2O_3)
LuScO	lutetium scandium oxide (LuScO_3)
M^2	M-squared factor
MBE	molecular beam epitaxy
MHz	megahertz
mJ	milijoule
MW	megawatt
N	doping concentration
n	refractive index
n_2	non-linear refractive index
nJ	nanojoule
nm	nanometer
ns	nanosecond
N_t	transparency density
P_{av}	average power
PECVD	plasma enhanced chemical vapor deposition
PCF	photonic crystal fiber
P_{peak}	peak power
PM	polarization maintaining
ps	picoseconds
q	complex radius of curvature
q_{axial}	axial-mode index
QD	quantum dot
Q-factor	quality factor
QML	Q-switched mode locking
QW	quantum well
R	radius of curvature
R_{lin}	linear reflectivity
R_{max}	maximum reflectivity
R_{ns}	reflectivity at full saturation

List of Abbreviations

s	optical sagitta
S	saturation parameter
ScO	scandium oxide (Sc_2O_3)
sech	hyperbolic secant
SESAM	semiconductor saturable absorber mirror
SHG	second-harmonic generation
Si_3N_4	silicon nitride
SiO_2	silicon dioxide
ScYLO	scandium yttrium lutetium oxide ($(\text{Sc}, \text{Y}, \text{Lu})_2\text{O}_3$)
SNR	signal-to-noise ratio
SPM	self-phase modulation
Ta_2O_5	tantalum pentoxide
TDL	thin-disk laser
TEM_{00}	fundamental transverse mode
TPA	two-photon absorption
T_R	round-trip time
VBG	volume Bragg grating
VUV	vacuum ultraviolet
w	beam radius
W	watts
Xe	xenon
XUV	extreme ultraviolet
YAG	yttrium aluminum garnet ($\text{Y}_3\text{Al}_5\text{O}_{12}$)
YCOB	calcium yttrium borate ($\text{Ca}_3\text{YO}(\text{BO}_3)_3$)
YO	yttrium oxide (Y_2O_3)
z_R	Rayleigh range

List of Symbols

β	level of inversion
Δf_g^c	gain bandwidth
ΔR	modulation depth
ΔR_{ns}	non-saturable losses
γ	self-phase modulation coefficient
κ	thermal conductivity
λ	wavelength
μJ	microjoule
μm	micrometer
η	efficiency
ν	optical frequency
ϕ_{Gouy}	Gouy phase shift
ϕ	phase shift
$\sigma_{\text{abs,L}}$	absorption cross section of the laser
$\sigma_{\text{em,L}}$	emission cross section of the laser
$\tau_{1/e}$	recovery time at 1/e
τ_{rad}	radiation or fluorescence life time
τ_p	FWHM pulse duration
ω	$1/e^2$ beam radius
ξ_{abs}	field enhancement factor

List of Publications

Parts of this thesis are published in the following journal papers and conference proceedings:

Journal Papers:

1. C. J. Saraceno, C. Schriber, F. Emaury, O. H. Heckl, C. R. E. Baer, M. Hoffmann, K. Beil, C. Kränkel, M. Golling, T. Südmeyer, U. Keller “Cutting-edge high-power ultrafast thin disk oscillators” – Invited Review Paper: *Applied Sciences*, accepted for publication, 2013
 2. F. Emaury, C. Fourcade Dutin, C. J. Saraceno, M. Trant, O. H. Heckl, Y.Y. Wang, C. Schriber, F. Gerome, T. Südmeyer, F. Benabid, and U. Keller “Beam delivery and pulse compression to sub-50 fs of a modelocked thin-disk laser in a gas-filled Kagome-type HC-PCF fiber” *Optics Express*, vol. 21, No. 4, pp. 4987-4994, 2013
 3. C. J. Saraceno, F. Emaury, O. H. Heckl, C. R. E. Baer, M. Hoffmann, C. Schriber, M. Golling, T. Südmeyer, U. Keller “275 W average output power from a femtosecond thin disk oscillator operated in a vacuum environment” *Optics Express*, vol. 20, no.21, pp. 23535-23541, 2012
 4. C. J. Saraceno, S. Pekarek, O. H. Heckl, C. R. E. Baer, C. Schriber, M. Golling, K. Beil, C. Kränkel, G. Huber, U. Keller, T. Südmeyer “Self-referenceable frequency comb from an ultrafast thin disk laser” *Optics Express*, vol. 20, No. 9, pp. 9650-9656, 2012
 5. C. J. Saraceno, O. H. Heckl, C. R. E. Baer, C. Schriber, M. Golling, K. Beil, C. Kränkel, T. Südmeyer, U. Keller “Sub-100 femtosecond pulses from a SESAM modelocked thin disk laser” *Appl. Phys. B*, vol. 106, No.3, pp. 559-562, Rapid Communication, 2012
 6. C. J. Saraceno, C. Schriber, M. Mangold, M. Hoffmann, O. H. Heckl, C. R. E. Baer, M. Golling, T. Südmeyer, U. Keller “SESAMs for high-power oscillators: design guidelines and damage thresholds” – Invited Paper *IEEE J. Selected Topics in Quantum Electronics (JSTQE)*, vol. 18, No. 1, pp. 29-41, 2012 (published online 13. Jan. 2011)
 7. C. R. E. Baer, O. H. Heckl, C. J. Saraceno, C. Schriber, C. Kränkel, T. Südmeyer, U. Keller “Frontiers in passively modelocked thin disk laser oscillators” – Invited Paper *Optics Express*, vol. 20, No. 7, pp.7054-7065, 2012
-

-
8. C. J. Saraceno, O. H. Heckl, C. R. E. Baer, M. Golling, T. Südmeyer, K. Beil, C. Kränkel, K. Petermann, G. Huber, U. Keller “SESAMs for high-power femtosecond modelocking: power scaling of an Yb:LuScO₃ thin disk laser to 23 W and 235 fs” *Optics Express*, vol. 19, No. 21, pp. 20288-20300, 2011
 9. C. J. Saraceno, O. H. Heckl, C. R. E. Baer, T. Südmeyer, U. Keller “Pulse compression of a high-power thin disk laser using rod-type fiber amplifiers” *Optics Express*, vol. 19, No. 2, 1395-1407, 2011
 10. O. H. Heckl, C. J. Saraceno, C. R. E. Baer, T. Südmeyer, Y. Y. Wang, Y. Cheng, F. Benabid, U. Keller “Temporal pulse compression in a Xenon-filled Kagome-type hollow core photonic crystal fiber at high average power” *Optics Express*, vol. 19, No. 20, pp. 19142-19149, 2011
 11. R. Peters, C. Kränkel, S. T. Fredrich-Thornton, K. Beil, K. Petermann, G. Huber, O. H. Heckl, C. R. E. Baer, C. J. Saraceno, T. Südmeyer, U. Keller “Thermal analysis and efficient high power continuous-wave and mode-locked thin disk laser operation of Yb-doped sesquioxides” – Invited Paper *Appl. Phys. B*, vol. 102, Nr. 3, pp. 509-514, 2011 (published online Feb. 15, 2011)
 12. O. H. Heckl, C. Kränkel, C. R. E. Baer, C. J. Saraceno, T. Südmeyer, K. Petermann, G. Huber, U. Keller “Continuous wave and mode-locked Yb:YCOB thin disk laser: first demonstration and future prospects” *Opt. Express*, vol. 18, No. 18, pp. 19201-19208, 2010
 13. C. R. E. Baer, C. Kränkel, C. J. Saraceno, O. H. Heckl, M. Golling, R. Peters, K. Petermann, T. Südmeyer, G. Huber, U. Keller “Femtosecond thin-disk laser with 141 W of average power” *Optics Lett.*, vol. 35, No. 13, pp. 2302-2304, 2010
 14. T. Südmeyer, C. Kränkel, C. R. E. Baer, O. H. Heckl, C. J. Saraceno, M. Golling, R. Peters, K. Petermann, G. Huber, U. Keller “High-power ultrafast thin disk laser oscillators and their potential for sub-100-femtosecond pulse generation” – Invited Paper *Appl. Phys. B*, vol. 97, Issue 2, pp. 281-295, 2009 (published online Sept. 15, 2009)
 15. C. R. E. Baer, C. Kränkel, C. J. Saraceno, O. H. Heckl, M. Golling, T. Südmeyer, R. Peters, K. Petermann, G. Huber, U. Keller “Femtosecond Yb:Lu₂O₃ thin disk laser with 63 W of average power” *Optics Lett.*, vol. 34, pp. 2823-2825, 2009

Conference publications

1. C. J. Saraceno, F. Emaury, O. H. Heckl, C. R. E. Baer, M. Hoffmann, C. Schriber, M. Golling, T. Südmeyer, and U. Keller “275 W average power from an Yb:YAG modelocked thin disk oscillator operated in a vacuum environment” *Ultrafast Optics (UFO VIII)*, Davos, Switzerland, Mar. 4-8, 2013
-

2. F. Emaury, C. Fourcade, C. J. Saraceno, M. Trant, O. H. Heckl, Y. Y. Wang, C. Schriber, F. Gerome, T. Südmeyer, F. Benabid, U. Keller "Beam delivery and pulse compression to sub-50 fs of a modelocked thin disk laser in a gas-filled Kagome-type HC-PCF fiber" *Ultrafast Optics (UFO VIII)*, Davos, Switzerland, Mar. 4-8, 2013
 3. C. Schriber, C. J. Saraceno, F. Emaury, M. Golling, K. Beil, C. Kränkel, T. Südmeyer, G. Huber, U. Keller "Passively modelocked thin disk lasers in the short pulse duration regime" *Ultrafast Optics (UFO VIII)*, Davos, Switzerland, Mar. 4-8, 2013
 4. C. J. Saraceno, C. Schriber, M. Mangold, M. Hoffmann, O. H. Heckl, C. R. E. Baer, M. Golling, T. Südmeyer, U. Keller "SESAM designs for ultrafast lasers" – **Invited talk** *SPIE Photonics West 2013*, LASE, Conference 8601-25 San Francisco, California, USA, Feb 2-6, 2013
 5. C. J. Saraceno, F. Emaury, M. Hoffmann, O. H. Heckl, C. R. E. Baer, M. Golling, C. Schriber, T. Südmeyer, U. Keller "Femtosecond Yb:YAG thin disk laser with 200 W of average power" - Postdeadline Paper - *5th EPS-QEOD Europhoton Conference*, Stockholm, Aug. 26 – Aug. 31, 2012
 6. C. J. Saraceno, C. Schriber, O. H. Heckl, C. R. E. Baer, M. Golling, K. Beil, C. Kränkel, T. Südmeyer, G. Huber, U. Keller "25 W, 185 fs from an Yb: Lu₂O₃ modelocked TDL" *5th EPS-QEOD Europhoton Conference*, Stockholm, Aug. 26 – Aug. 31, 2012
 7. F. Emaury, C. Fourcade, C. J. Saraceno, O. H. Heckl, Y. Y. Wang, C. Schriber, C. R. E. Baer, T. Südmeyer, F. Benabid, U. Keller "Pulse compression of a modelocked TDL to 10 MW, sub-50 fs in a gas-filled Kagome type HC-PCF" *5th EPS-QEOD Europhoton Conference*, Stockholm, Aug. 26 – Aug. 31, 2012
 8. C. J. Saraceno, S. Pekarek, O. H. Heckl, C. R. E. Baer, C. Schriber, M. Golling, K. Beil, C. Kränkel, G. Huber, T. Südmeyer, U. Keller "Ultrafast thin disk lasers: recent progress in short pulse generation (<100 fs) and carrier envelope offset phase detection" *XVIIIth International Conference on Ultrafast Phenomena (UP2012)*, Lausanne, Switzerland, 8-13 July, 2012
 9. C. Schriber, C. J. Saraceno, S. Pekarek, O. H. Heckl, C. R. E. Baer, M. Golling, K. Beil, C. Kränkel, G. Huber, T. Südmeyer, U. Keller "High power SESAM modelocked thin disk lasers: access to sub-100 fs pulses and first CEO beat frequency detection" *Annual Meeting of the Swiss Physical Society (SPG Jahrestagung 2012)*, ETH Zurich, Switzerland, June 21-22, 2012
 10. C. J. Saraceno, S. Pekarek, O. H. Heckl, C. R. E. Baer, C. Schriber, M. Golling, K. Beil, C. Kränkel, G. Huber, U. Keller, T. Südmeyer "Ultrafast thin disk lasers for intralaser extreme nonlinear optics" – Invited talk – CM1D.6 *CLEO 2012*, San Jose, CA, USA, 6-11 May 2012
-

-
11. F. Emaury, C. Fourcade, C. J. Saraceno, O. H. Heckl, Y. Y. Wang, C. Schriber, C. R. E. Baer, T. Südmeyer, F. Benabid, U. Keller “Sub-100-fs pulse compression in a hollow-core photonic crystal fiber (HC-PCF)” – Talk CTh4B.3 *CLEO 2012*, San Jose, CA, USA, 6-11 May 2012
 12. V. J. Wittwer, O. D. Sieber, M. Mangold, M. Hoffmann, C. J. Saraceno, M. Golling, B. W. Tilma, T. Südmeyer, U. Keller “First MIXSEL with a quantum well saturable absorber: shorter pulse durations and higher repetition rates” – Talk CW1N.2 *CLEO 2012*, San Jose, CA, USA, 6-11 May 2012
 13. Kolja Beil, Clara J. Saraceno, Oliver H. Heckl, Cyrill R. E. Baer, Cinia Schriber, Matthias Golling, Thomas Südmeyer, Christian Kränkel, Günter Huber und Ursula Keller “Bandbreitenlimitierte Pulse mit Yb:Lu₂O₃ im Scheibenlaser” – *DPG Stuttgart, March 2012*
 14. C. J. Saraceno, S. Pekarek, O. H. Heckl, C. R. E. Baer, C. Schriber, M. Golling, T. Südmeyer, K. Beil, C. Kränkel, G. Huber, U. Keller “Self-referencable high-power frequency comb from a 7-W, 142-fs Yb:Lu₂O₃ thin disk laser oscillator” *Advanced solid-state photonics (ASSP 2012)*, San Diego, California, USA, 29. Jan. – 1. Feb. 2012
 15. C. J. Saraceno, M. Hoffmann, C. Schriber, O. H. Heckl, C. R. E. Baer, M. Golling, T. Südmeyer, U. Keller “SESAMs for high-power femtosecond modelocking: influence of growth temperature on damage and nonsaturable losses” – Poster Session 1, Poster AM4A.13 *Advanced solid-state photonics (ASSP 2012)*, San Diego, California, USA, 29. Jan. – 1. Feb. 2012
 16. C. J. Saraceno, O. H. Heckl, C. R. E. Baer, M. Golling, T. Südmeyer, U. Keller, K. Beil, C. Kränkel, K. Petermann, G. Huber “Power scaling of an Yb:LuScO₃ thin disk laser to 23 W and 235 fs” *SPIE Photonics West 2012*, LASE, Solid-State Lasers: Technology and Devices, Conference LA101, San Francisco, California, USA, Jan. 21-26, 2012
 17. C. Kränkel, C. J. Saraceno, O. H. Heckl, C. R. E. Baer, M. Golling, T. Südmeyer, K. Beil, K. Petermann, G. Huber and U. Keller – Invited talk – “Ultrafast and high power thin disk lasers” *2nd EOS Topical Meeting on Lasers (ETML’11)*, Capri, Italy, 26. Sept. – 28. Sept. 2011
 18. S. Pekarek, C. J. Saraceno, O. H. Heckl, C. R. E. Baer, C. Schriber, M. Golling, T. Südmeyer, K. Beil, C. Kränkel, G. Huber, U. Keller “Self-referencable high-power frequency comb from a 7-W, 142-fs Yb: Lu₂O₃ thin disk laser oscillator” – Postdeadline Paper *Ultrafast Optics (UFO VIII)*, Monterey, USA, Sept. 26-30, 2011
 19. C. J. Saraceno, O. H. Heckl, C. R. E. Baer, M. Golling, T. Südmeyer, K. Beil, C. Kränkel, K. Petermann, G. Huber, U. Keller “High damage threshold SESAMs for high power femtosecond modelocking: 23 W, 235 fs Yb:LuScO₃ thin disk laser” - Postdeadline Paper – PDA.9 *Conference on Lasers and Electro-Optics – European*
-

- Quantum Electronics Conference (CLEO Europe – EQEC 2011)*, Munich, Germany, 22-26 May 2011
20. C. J. Saraceno, O. H. Heckl, C. R. E. Baer, T. Südmeyer, Y. Cheng, Y. Y. Wang, F. Benadbid, U. Keller “High average power temporal pulse compression in a Xe-filled Kagome-type hollow-core photonic crystal fiber (HC-PCF)” – Talk CD7.1 *Conference on Lasers and Electro-Optics – European Quantum Electronics Conference (CLEO Europe – EQEC 2011)*, Munich, Germany, 22-26 May 2011
 21. C. R. E. Baer, C. J. Saraceno, O. H. Heckl, M. Golling, T. Südmeyer, K. Beil, C. Kränkel, K. Petermann, G. Huber and U. Keller “CW and modelocked operation of an Yb:(ScYLu)₂O₃ thin-disk laser” – Talk CA11.3 *Conference on Lasers and Electro-Optics – European Quantum Electronics Conference (CLEO Europe – EQEC 2011)*, Munich, Germany, 22-26 May 2011
 22. O. H. Heckl, C. J. Saraceno, C. R. E. Baer, T. Südmeyer, U. Keller “Active rod-type fiber compressor for high-power thin disk lasers” – Talk CJ4.4 *Conference on Lasers and Electro-Optics – European Quantum Electronics Conference (CLEO Europe – EQEC 2011)*, Munich, Germany, 22-26 May 2011
 23. C. J. Saraceno, O. H. Heckl, C. R. E. Baer, M. Golling, T. Südmeyer, K. Beil, C. Kränkel, K. Petermann, G. Huber and U. Keller “CW and modelocked operation of an Yb:(ScYLu)₂O₃ thin-disk laser” – Talk CWP1 *CLEO 2011, Laser Science to Photonics Applications*, Baltimore, Maryland, USA, May 1-6, 2011
 24. C. J. Saraceno, C. Schriber, M. Mangold, O. H. Heckl, C. R. E. Baer, M. Golling, T. Südmeyer and U. Keller “SESAMs for high power oscillators: damage thresholds and design guidelines” – Talk CFO1 *CLEO 2011, Laser Science to Photonics Applications*, Baltimore, Maryland, USA, May 1-6, 2011
 25. O. H. Heckl, C. J. Saraceno, C. R. E. Baer, T. Südmeyer, Y. Chang, Y. Y. Wang, F. Benabid, U. Keller “Temporal pulse compression in a Xe-filled Kagome-type hollow core photonic crystal fiber at high average power” – Talk CMJ1 *CLEO 2011, Laser Science to Photonics Applications*, Baltimore, Maryland, USA, May 1-6, 2011
 26. T. Südmeyer, C. R. E. Bär, C. Kränkel, C. J. Saraceno, O. H. Heckl, M. Golling, R. Peters, K. Petermann, G. Huber, U. Keller – Invited Talk – “Power scaling of femtosecond thin disk lasers” Invited Talk *Advanced Solid-State Photonics (ASSP’11)*, Istanbul, Turkey, Feb. 13-16, 2011
 27. C. R. E. Baer, C. Kränkel, C. J. Saraceno, O. H. Heckl, M. Golling, T. Südmeyer, U. Keller, R. Peters, K. Petermann, G. Huber “Efficient femtosecond Yb: Lu₂O₃ thin disk laser with an average power of 141 W” *6th International Conference on Laser Assisted Net Shape Engineering (LANE 2010)*, Erlangen, Germany, Sept. 21-24, 2010
-

-
28. C. J. Saraceno, C. Schriber, M. Mangold, M. Hoffmann, O. H. Heckl, C. R. E. Baer, M. Golling, T. Südmeyer, U. Keller “Low-loss, high-damage threshold SESAMs for high pulse energy oscillators” – Talk TuC5 *4th EPS-QEOD Europhoton Conference*, Hamburg , Aug. 29 – Sept. 3, 2010
 29. C. J. Saraceno, C. R. E. Baer, C. Kränkel, O. H. Heckl, M. Golling, T. Südmeyer, U. Keller, R. Peters, K. Petermann, G. Huber “120 W average power from a modelocked Yb:Lu₂O₃ thin disk laser” – Talk CThA4 (Thursday 9 am) *Conference on Lasers and Electro-Optics (CLEO 2010)*, San Jose, USA, May 16 -21, 2010
 30. C. J. Saraceno, O. H. Heckl, C. R. E. Baer, C. Kränkel, T. Südmeyer, U. Keller “Pulse compression of a high power modelocked thin disk oscillator using a rod-type fiber amplifier” –Talk CFD2 (Friday 8:15 am) *Conference on Lasers and Electro-Optics (CLEO 2010)*, San Jose, USA, May 16 -21, 2010
 31. C. Kränkel, O. H. Heckl, R. Peters, C. R. E. Baer, C. J. Saraceno, K. Beil, T. Südmeyer, U. Keller, K. Petermann, G. Huber “High power Yb-doped thin disk lasers pumped with a volume Bragg grating stabilized laser diode at the zero-phonon line” – Poster *4th EPS-QEOD Europhoton Conference*, Hamburg , Aug. 29 – Sept. 3, 2010
 32. C. R. E. Baer, C. Kränkel, O. H. Heckl, C. J. Saraceno, M. Golling, R. Peters, K. Petermann, T. Südmeyer, G. Huber, U. Keller “Modelocked Yb:Lu₂O₃ thin disk laser with an average power of 140 W” – Talk TuA2 *4th EPS-QEOD Europhoton Conference*, Hamburg , Aug. 29 – Sept. 3, 2010
 33. C. Kränkel, C. R. E. Baer, O. H. Heckl, C. J. Saraceno, K. Beil, M. Golling, K. Petermann, G. Huber, T. Südmeyer, U. Keller - Invited talk -“Record high output powers from modelocked and continuous wave Yb:Lu₂O₃ thin disk lasers” *International Laser Physics Workshop 2010 (LPHYS'10)*, *Seminar on Modern Trends in Laser Physics*, Foz do Iguacu, Brazil, July 5 - 9, 2010
 34. T. Südmeyer, C.R.E. Baer, C. Kränkel, C.J. Saraceno, O.H. Heckl, M. Golling, R. Peters, K. Petermann, G. Huber, and U. Keller, - Invited Talk - "Recent advances in high power ultrafast thin disk laser oscillators", *14th International Conference "Laser Optics 2010"*, St.Petersburg, Russia, June 28 - July 02, 2010.
 35. T. Südmeyer, C. R. E. Baer, C. Kränkel, C. J. Saraceno, O. H. Heckl, M. Golling, R. Peters, K. Petermann, G. Huber, U. Keller - Invited talk - “Recent advances in high power ultrafast thin disk laser oscillators” *Stuttgarter Lasertagen 2010 (SLT 2010)*, Stuttgart, Germany, June 8-10, 2010
 36. C. Kränkel, R. Peters, O. H. Heckl, C. R. E. Baer, C. J. Saraceno, K. Beil, T. Südmeyer, K. Petermann, U. Keller, G. Huber “Yb-doped sesquioxide thin disk lasers exceeding 300 W of output power in continuous-wave operation” – Talk
-

- CTuQQ2 (Tuesday 5:45 pm) *Conference on Lasers and Electro-Optics (CLEO 2010)*, San Jose, USA, May 16 -21, 2010
37. O. H. Heckl, C. R. Kränkel, C. R. E. Baer, C. J. Saraceno, T. Südmeyer, K. Petermann, G. Huber, U. Keller “Power scaling of an Yb:YCOB thin disk laser to 101 W cw and initial modelocking experiments” – Oral Talk CThA5 (Thursday 9:15 am) *Conference on Lasers and Electro-Optics (CLEO 2010)*, San Jose, USA, May 16 -21, 2010
38. C. Kränkel, C. Bär, O. H. Heckl, C. J. Saraceno, K. Beil, R. Peters, M. Golling, T. Südmeyer, K. Petermann, G. Huber, U. Keller “Yb:Lu₂O₃-Scheibenlaser mit 120 W in 800-fs Pulsen und 301 W im cw-Betrieb” *Verhandlungen der Deutschen Physikalischen Gesellschaft (DPG-Tagung)*, Sektion AMOP der DPG, Hannover, March 8-12, 2010
39. C. R. E. Bär, C. Kränkel, C. J. Saraceno, O. H. Heckl, M. Golling, T. Südmeyer, U. Keller, R. Peters, K. Petermann, G. Huber - Talk AMD2 “Efficient modelocked Yb:Lu₂O₃ thin disk laser with an average power of 103 W” *Advanced Solid-State Photonics (ASSP'10)*, San Diego, USA, Feb. 1-3, 2010
40. O. H. Heckl, R. Peters, C. Kränkel, C. R. E. Baer, C. J. Saraceno, T. Südmeyer, K. Petermann, U. Keller, G. Huber “Continuous-wave Yb-doped sesquioxide thin disk lasers with up to 300 W output power and 74% efficiency” – Talk AMD1 *Advanced Solid-State Photonics (ASSP'10)*, San Diego, USA, Feb. 1-3, 2010
41. T. Südmeyer, C. R. E. Baer, C. Kränkel, O. H. Heckl, C. J. Saraceno, M. Golling, R. Peters, K. Petermann, G. Huber and U. Keller “High power femtosecond thin disk lasers” *17th International Conference on Advanced Laser Technologies (ALT-2009)*, Antalya, Turkey, Sept. 26-Oct. 1, 2009
42. T. Südmeyer, C. R. E. Baer, C. Kränkel, O. H. Heckl, C. J. Saraceno, M. Golling, R. Peters, K. Petermann, G. Huber, U. Keller - Invited talk - “High power ultrafast laser oscillators” *Ultrafast Optics and High Field Short Wavelength (UFO VII & HFSW XIII 2009)*, Arcachon, France, Aug. 31 – Sept. 4, 2009
43. T. Südmeyer, C. Kränkel, C. R. E. Baer, O. H. Heckl, C. J. Saraceno, M. Golling, R. Peters, K. Petermann, G. Huber, U. Keller - Invited talk - “Shorter pulses from femtosecond thin disk lasers” *International Laser Physics Workshop 2009 (LPHYS'09)*, Seminar on Modern Trends in Laser Physics, Barcelona, Spain, July 13-17, 2009
44. C. R. E. Baer, C. Kränkel, C. J. Saraceno, O. H. Heckl, M. Golling, T. Südmeyer, R. Peters, K. Petermann, G. Huber, U. Keller “63-W average power from femtosecond Yb:Lu₂O₃ thin disk laser” – Talk CA2.3 *Conference on Lasers and Electro-Optics – European Quantum Electronics Conference (CLEO Europe – EQEC 2009)*, Munich, Germany, June 14-19, 2009
-

Abstract

Ultrafast lasers sources are one of the main scientific achievements of the past decades. Finding new avenues to obtain higher average powers from these sources is currently a topic of important research efforts. Such high peak power and high repetition rate sources have a strong impact on a wide range of applications both in industry - for high-speed and high-precision micromachining - and in scientific research - for example for experiments in strong-field physics. One prominent application field in this area is the generation of high-harmonic radiation at increased photon flux, which is an elegant way of extending current coherent sources to the vacuum ultraviolet and extreme ultraviolet wavelength regions. This very rich application field is one of many strong motivations to push the limits of existing and emerging ultrafast laser technologies.

The main technological challenges that arise from the combination of high average and peak powers are mainly an excessive heat deposition in the gain medium and a too large nonlinearity accumulated by the pulses during propagation. In the past few years, several clever geometries have been suggested to overcome these limitations. Most of them are based on amplification schemes that require a low-power seed oscillator and several amplifying stages to reach the targeted high average power. In this thesis, we focus on pushing the performance of semiconductor saturable absorber mirror (SESAM) modelocked thin-disk lasers (TDLs). These power-scalable ultrafast lasers enable high average powers and femtosecond operation directly from a single oscillator, without the need for additional amplification stages. Several important steps were performed during this thesis to push this technology to new limits.

Up-to-date, the limitations of SESAM technology in terms of damage and lifetime were not thoroughly investigated and contradictory information on damage thresholds was reported. During this thesis, we carried out a detailed study of damage and lifetime of SESAMs designed for high-power femtosecond oscillators. We established simple guidelines to design robust SESAMs with high-damage thresholds and optimized

parameters for operation at extreme intracavity conditions. The SESAMs developed following these guidelines were key to the demonstration of all the cutting-edge lasers presented in this work.

The scientific applications targeted by the sources developed during this thesis require short pulse durations (sub-100 fs). Current state-of-the-art TDLs are restricted in this aspect to > 500 fs. Extending the high-power capabilities of TDLs to the sub-100 fs regime is, therefore, a major milestone, which is intimately linked to the development of novel broadband materials suitable for this geometry. During this thesis, we explored the limits in terms of pulse duration of modelocked TDLs based on different gain materials and achieved a first important step in this direction, with the demonstration of sub-100 fs pulses from a TDL based on the sesquioxide gain material Yb:LuScO_3 (LuScO). In these first experiments, sub-100 fs operation was achieved at moderate average output powers (5 W). However, preliminary power scaling experiments indicate that much higher output powers are within reach. Furthermore, the intracavity peak power levels achieved are already high enough for preliminary intralaser nonlinear optics experiments.

The progress achieved in terms of pulse duration enabled us to explore for the first time the carrier-envelope phase properties of these sources. We measured the carrier-envelope offset (CEO) frequency of a TDL, which will allow us to fully stabilize such a source. This experiment shows that TDLs are excellent candidates for applications in spectroscopy and metrology, where high-power frequency combs are of interest.

In addition to exploring the pulse duration limits of TDLs, we pushed the average power of modelocked oscillators to a new limit with the demonstration of a femtosecond oscillator with 275 W – the highest average power reported from an ultrafast oscillator to date. The laser was based on the gain material Yb:YAG , operated with a pulse duration of 583 fs and had a pulse energy of 16.9 μJ . This performance was obtained by operating the laser oscillator in a vacuum environment to eliminate the parasitic nonlinearity of the air inside the oscillator. This new approach is an important step forward to reaching the kilowatt average power level milestone.

The results presented in this thesis indicate that short enough pulses

and sufficient peak power to drive strong-field physics experiments directly from a single high-power TDL should be within reach. In the meantime, temporal pulse compression of state-of-the-art TDLs is essential. Two promising pulse compression techniques – using rod-type fiber amplifiers and gas-filled hollow-core Kagome-type photonic crystal fibers (PCF) – were explored during this thesis.

The cutting-edge lasers developed during this thesis enable exciting new applications, and open the door to further extending the current performance milestones.

Résumé

Les sources lasers à impulsions ultra-courtes représentent l'une des inventions les plus importantes de ces dernières décennies. De nombreux efforts de recherche visent actuellement à augmenter la puissance moyenne de ces sources. Cette thématique est portée par le grand nombre d'applications nécessitant des sources laser de puissance crête élevée et à haute cadence. Le secteur industriel montre, en effet, un intérêt croissant pour ces sources dans le domaine du micro-usinage rapide et de haute précision. Pour des applications de physique fondamentale, ce type de source se révèle également la clé de nouvelles avancées, comme par exemple dans le domaine de l'interaction laser-matière. Un exemple majeur concerne la génération d'harmoniques d'ordre élevé à haut flux de photons, représentant une alternative élégante pour étendre les sources cohérentes actuelles dans le domaine de longueur d'onde de l'ultraviolet extrême. La richesse des champs d'application ouverts par de telles sources est l'une des motivations essentielles qui ont conduit à développer les technologies existantes.

Les principaux défis technologiques pour combiner une puissance moyenne élevée et une puissance crête importante résident dans une extraction efficace de la chaleur générée dans le milieu à gain, et dans la réduction des nonlinéarités engendrées lors de la propagation des impulsions. Au cours des décennies passées, plusieurs géométries ont été suggérées afin de réduire au mieux ces limitations. Dans cette thèse, nous nous intéressons à la technologie des lasers à disque mince, pour lesquels le verrouillage des modes en phase est effectué passivement à l'aide d'absorbants saturables à semiconducteur (SESAM). Cette technologie permet de combiner des puissances moyennes élevées avec des impulsions ultra-courtes directement en sortie d'oscillateur. Plusieurs avancées cruciales ont été réalisées dans le cadre de cette thèse, repoussant une fois de plus les limites de ce type de sources.

L'obtention de puissances moyennes plus élevées et de durées d'impulsion plus courtes avec cette technologie repose sur les capacités des

SESAMs à opérer à des niveaux de puissance crête élevés. De nombreuses informations contradictoires ont été reportées dans la littérature à ce sujet. Cette thèse a permis une étude détaillée de la durée de vie et des seuils de dommage de SESAMs conçus spécialement pour des oscillateurs à haute puissance. Nous en avons déduit des règles simples pour la fabrication de SESAMs optimisés pour opérer dans des conditions intra-cavité extrêmes. Les SESAMs ainsi développés ont été l'un des facteurs clés dans la démonstration des résultats obtenus dans le cadre de cette thèse.

Les sources développées pendant cette thèse visaient principalement à des applications scientifiques où l'obtention d'impulsions courtes (< 100 fs) est un point essentiel. Les lasers ultra-rapides à disque mince atteignent de nos jours des puissances crête de l'ordre de plusieurs dizaines de MW mais restent typiquement limités à des durées d'impulsion supérieures à 500 fs. D'importants efforts de recherche visent à réduire la durée d'impulsion de ces sources. Cet objectif est étroitement lié au développement de nouveaux matériaux laser à large bande spectrale de gain, appropriés pour cette géométrie laser. Au cours de cette thèse, nous avons exploré les limites de ces sources en terme de durée d'impulsion, et nous avons démontré que cette technologie peut atteindre des durées d'impulsion inférieures à 100 fs, grâce à un laser à disque mince basé sur le milieu à gain Yb:LuScO_3 . Bien que cette première réalisation atteigne des puissances moyennes de sortie modérées (5 W), les premières expériences visant à augmenter la puissance moyenne sont prometteuses. De plus, les performances intracavité obtenues constituent déjà une alternative intéressante à exploiter dans le cadre d'expériences non-linéaires.

Le progrès ainsi réalisé en terme de durée d'impulsion nous a permis d'explorer pour la première fois les propriétés du décalage enveloppe-porteuse de ce type de source. Par cette première mesure de la fréquence de décalage enveloppe-porteuse d'un laser à disque mince, nous démontrons l'un des points essentiels à la stabilisation de ce type de source et à son utilisation en tant que peigne de fréquence. Ceci prouve que cette technologie représente un excellent candidat pour des applications de spectroscopie et de métrologie optique.

Nous avons également réalisé un laser femtoseconde à disque mince atteignant une puissance moyenne de 275 W. Ce laser correspond à

l'oscillateur femtoseconde délivrant la plus haute puissance moyenne jamais démontrée à ce jour. Ce laser, basé sur le milieu classique à gain Yb:YAG, permet d'atteindre une durée d'impulsion de 583 fs et une énergie de 16.9 μ J. Une telle performance a été rendue possible grâce à la mise sous vide de l'oscillateur, permettant de réduire les effets non-linéaires parasites dans l'air au sein de la cavité laser. Cette approche représente une étape importante dans le développement d'oscillateurs femtoseconde d'une puissance moyenne de l'ordre du kilowatt.

La compression temporelle des impulsions en sortie du laser est essentielle pour atteindre les durées d'impulsion visées. Deux approches seront présentées dans cette thèse, basées sur différentes géométries fibrées.

Les systèmes laser développés pendant cette thèse ouvrent la voie vers de nouvelles applications et de nouveaux développements permettant d'améliorer les performances actuelles.

Chapter 1 - Introduction

“If you were offered \$1000 to go an entire day without interacting with lasers, do you think you could do it? What if you also couldn't use anything that had been built with the help of lasers?” [1]. This question was posed recently in an article on the Internet entitled *Life without lasers* in a special issue celebrating the recent 50-year anniversary of the laser invention [2]. As a laser physicist, one would most likely not take this bet, knowing in advance that this “day without lasers” would certainly be a very uncomfortable day, without cell-phones, internet, computers, smartphones, flatscreens and DVDs. Furthermore, these example do not include a massive number of laser-fabricated devices that surrounds us, for example parts used in cars, trains, airplanes.

In addition to an important number of industrial applications, lasers have tremendous impact on many disciplines of scientific research (for example in biology, chemistry, physics, materials science and medicine) where they have become essential tools for better understanding some of nature's secrets, and will most likely keep unveiling mysteries and solving technological challenges. This makes laser physics an exciting research topic, where pushing the limits of existing laser sources opens up new applications that were previously impossible or restricted to very complex driving systems.

A striking example is the fast development of ultrafast lasers, which have progressed in the past years from complex and specialized systems to widely used scientific and industrial instruments [3-5]. These sources generate intense and very short laser light bursts (with durations of femtoseconds = 10^{-15} s to picoseconds = 10^{-12} s) and can be tightly focused in space, reaching electric field strengths comparable to those binding electrons to atoms and molecules. This enables the study of the interaction of matter with these strong fields and allows us to temporally resolve complex dynamic processes that occur on this timescale. This research topic is most widely referred to as strong-field physics.

In the work presented in this thesis, we focus on the development of state-of-the-art ultrafast oscillators for such strong-field applications. Ideally, sources for these applications would combine

- short pulse durations $\tau_p < 100$ fs
- sufficiently high pulse energy E_p to achieve the required electric field peak intensity (a reference value corresponding to typical values of the atomic binding force is $I_{pk} > 10^{14}$ W/cm²)
- and high repetition rates $f_{rep} > 1$ MHz (therefore high average power since $P_{av} = E_p \cdot f_{rep}$).

Nowadays, most laboratory-based ultrafast laser systems for such applications rely on complex amplifier systems based on Ti:sapphire technology that can deliver few-cycle pulses with GWs of peak power, sufficient to reach the necessary electric field strength to carry out the targeted experiments. However, in addition to being complex and expensive, these sources are limited to repetition rates in the kilohertz range, corresponding to only a few watts of average power.

Therefore, the development of novel ultrafast sources that operate at higher average power is currently a topic of active investigation. The combination of high peak power and high average power is very attractive for the targeted strong-field applications. Photoionization studies in noble gases show that driving high-field science experiments at multimegahertz repetition rate, results in a reduced measurement time, a higher signal-to-noise ratio, and partial elimination of space charge issues [6]. An important example where such sources would have major impact is high harmonic generation (HHG) [7, 8] where driving the experiments with high-average power sources opens new avenues for increasing the vacuum ultraviolet and extreme ultraviolet (VUV/XUV) photon flux [9], possibly in combination with enhanced phase-matching techniques (such as hollow-core photonic crystal fibers (HC-PCF) [10], or resonant field enhancement in nanostructured targets [11]). Such compact megahertz sources of coherent radiation in the VUV/XUV spectral region would enable coherent sources to be available at a wavelength range where laser transitions are not known to date.

Several groundbreaking technologies are currently pushing the limits in terms of average power of ultrafast sources: slab amplifiers [12], fiber based chirped pulse amplifiers (CPA) [13], and thin-disk laser (TDLs) oscillators [14] and amplifiers [15]. The common key points of these technologies are:

- a geometry that enables outstanding heat removal capabilities
- a clever layout to avoid excessive nonlinearities during propagation.

During this thesis, we focused on modelocked thin-disk laser oscillators, which have the potential to reach the targeted performance directly from a table-top high-power oscillator with a similar footprint to a low-power oscillator.

In contrast to bulk oscillators, where thermal aberrations that occur in the gain medium limit the achievable output power, the TDL concept [16, 17] is based on a very thin disk-shaped gain medium that can be efficiently cooled through the backside. The resulting outstanding heat removal capabilities allows for high average powers and excellent beam quality. In addition, the very thin gain medium is ideally suited for small amounts of accumulated nonlinearity even at very high peak powers.

Furthermore, modelocking using semiconductor saturable absorber mirrors (SESAMs) is currently the best-suited approach for high-power ultrafast laser oscillators. The invention of the SESAM nearly 20 years ago [4, 18, 19] represented an important breakthrough in the development of more convenient and robust ultrafast laser sources. It enabled the first stable and self-starting passive modelocking of diode-pumped solid-state lasers (DPSSLs), resolving the long-standing Q-switching problem [6]. Today, SESAMs have become key devices for modelocking numerous laser types, including DPSSLs, fiber lasers, and semiconductor lasers. Semiconductors are ideally suited for saturable absorbers because they can cover a broad wavelength range and yield short recovery times, supporting the generation of ultrashort pulse durations. The macroscopic nonlinear optical parameters for modelocking can be optimized over a wide range by the design of the mirror structure and the choice of the semiconductor absorber.

The combination of these two concepts results in a power scalable ultrafast technology. The output power of TDLs can be increased simply by increasing the pump power with both an increased pump spot size on the disk and laser spot size on the SESAM by the same factor. This resulted in a steady increase of the average power and pulse energy available from such sources since their first demonstration in the year 2000 [20] (Figure 1). Currently, SESAM modelocked TDLs achieve higher average powers (> 275 W [14]) and pulse energies (> 40 μ J [21]) than any other oscillator technology.

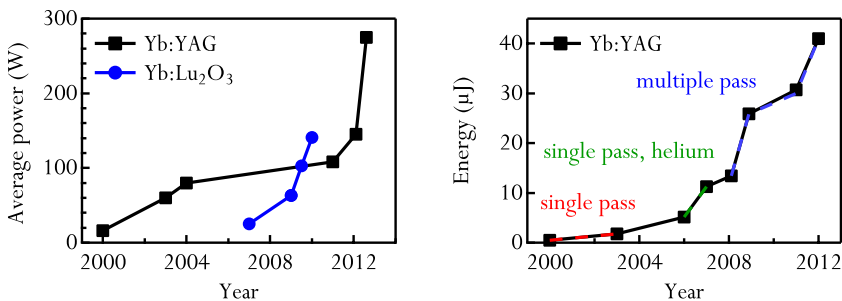


Figure 1.1: Evolution of average power (left) and pulse energy (right) of ultrafast modelocked TDLs. Most power and energy scaling was achieved using the well-established gain material Yb:YAG, but promising new materials for this application are currently the topic of important research efforts.

This thesis is organized as follows. In Chapter 1, we will present general aspects of SESAM modelocked TDLs, with a particular focus on the specific challenges of modelocking at high power levels.

In Chapter 2, we present a detailed study of damage threshold and lifetime of SESAMs designed for high-power femtosecond oscillators. We present guidelines to design and fabricate SESAMs with specific parameters and high-damage threshold, a crucial point towards kW-level TDLs.

In Chapter 3, we investigate the pulse duration limits of modelocked TDLs based on promising sesquioxide gain materials. Prior to the work presented in this thesis, modelocked TDLs were limited to pulse durations >200 fs. Here we demonstrate that they can access the sub-100 fs regime,

opening promising doors for driving highly nonlinear experiments directly from a high-power oscillator (Figure 1.2).

In Chapter 4, we present the first measurement of the carrier envelope-offset (CEO) frequency of a TDL, opening the door to unamplified high-power frequency combs. The record-short pulses of the thin-disk source used for this experiment (presented in Chapter 3) was one of the key requirements to achieve this result.

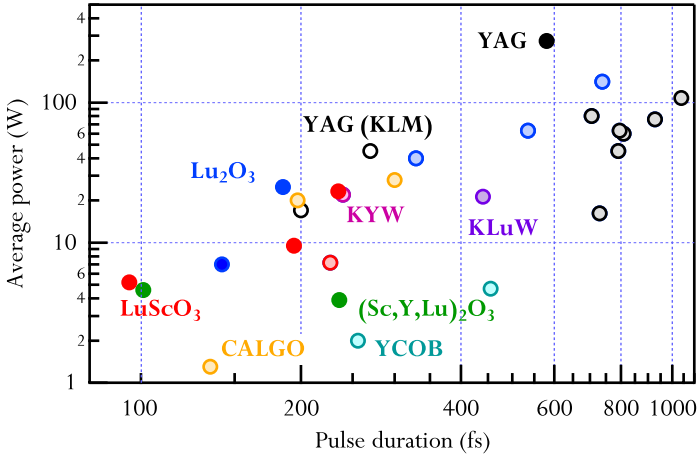


Figure 1.2: Pulse duration of modelocked TDLs demonstrated to date using different gain materials versus their average power, illustrating the difficulty of combining high average power and short pulse durations. The filled-in characters are results that will be presented in this thesis.

In Chapter 5, we present the latest power scaling result obtained with a TDL based on the gain material Yb:YAG, which was operated in a vacuum environment. We demonstrated an oscillator with 275 W and 583 fs pulse duration, which is, to the best of our knowledge, the highest average power obtained to-date from a passively modelocked oscillator.

Finally we discuss pulse compression of modelocked TDLs in Chapter 6. State-of-the-art TDL systems with sufficiently high peak power for the targeted applications typically operate with pulse durations of >500 fs (Figure 1.2). Therefore, different techniques to efficiently reduce the pulse duration of such sources are currently being investigated. We will

present results obtained with two pulse compression techniques, based on rod-type fiber amplifiers and on HC-PCF, and will discuss their capabilities.

Finally, this thesis concludes with an outlook towards higher average powers, higher pulse energies and higher peak powers from SESAM modelocked TDLs.

The sources developed during this thesis open the door to further extending the performance of this ultrafast technology, and to exciting experiments to come. One exciting possibility is making use of the very high intracavity peak powers inside a TDL to drive highly nonlinear experiments such as HHG, following the model of the well-established passive enhancement cavities [22]. The results presented in Chapters 3 and 4 are important steps towards the realization of such experiments. Furthermore, the system presented in Chapter 5 already reaches 26 MW of output peak power, at an average power of 275 W and a pulse duration of 583 fs. We expect to enhance the peak power of this system to >100 MW and obtain sub-50 fs pulse duration with a simple passive external compression stage based, for example, on a short gas-filled HC-PCFs such as the one presented in Chapter 6. This temporally compressed source will be ideally suited for strong-field experiments.

Chapter 2 - Modelocked high-power thin-disk lasers: challenges and milestones

As we highlighted in the introduction, novel femtosecond sources that combine high peak power and high repetition rate are currently the subject of important research efforts. In the past years, several technological breakthroughs resulted in the demonstration of energetic multi-100 W average power (up to 1 kW) femtosecond sources such as slab amplifiers [12] and fiber based CPA [13]. These amplifier-based systems are most commonly seeded by low power oscillators. Modelocked thin-disk lasers (TDLs) have the potential to reach the targeted performance directly from a table-top oscillator, which would significantly simplify the targeted complex experimental setups.

The outstanding heat removal capability of the thin-disk geometry [16, 17] enables us to achieve excellent beam quality at high average powers, a key requirement for passive modelocking. In addition, SESAMs can be designed for operation at extreme intracavity conditions, and over a wide range of absorber parameters. The combination of these two technologies results in a power scalable ultrafast technology that has enabled a steady rise of both energy and average power of these sources since their first demonstration in the year 2000 [20].

In this Chapter, we will summarize the basic concepts of modelocked TDLs with a focus on the specific challenges of modelocking at high-power levels. We will first review the advantages in terms of heat management of TDLs. In a second part, we will summarize the basic concepts of soliton modelocking, and will discuss corresponding challenges for high-power TDLs. We will conclude with an outlook towards future kilowatt level TDLs.

2.1 Thin-disk laser technology

2.1.1 Thermal management: the key for high-power operation

The TDL approach is based on a gain material that has the shape of a thin disk with a highly reflective (HR) coating on one side and an anti-reflective (AR) coating on the other side for both pump and laser wavelengths (Figure 2.1, right). Typically, the thin gain medium has a thickness of some hundred micrometers, whereas pump spot size diameters are in the order of several millimeters. Unlike other bulk geometries, efficient heat removal can be achieved by mounting the HR side of the disk onto a heatsink (typically based on copper, copper-tungsten or diamond) that can be cooled, for example, with water (Figure 2.1, left). The resulting nearly one-dimensional heat flow along the beam axis leads to small thermal distortions and aberrations at very high pump power intensities. In addition to supporting high average powers, the thin-disk geometry is ideally suited for applications involving ultrashort pulses, because the very short interaction length of the pulses with the gain medium results in very low accumulated nonlinearities.

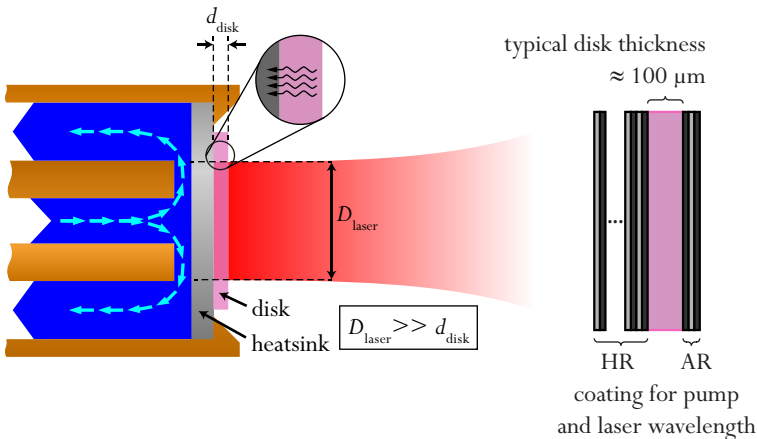


Figure 2.1: Schematic of the cooling scheme of a thin disk gain medium. In this schematic illustration, the disk is contacted to a heatsink that is water-cooled through the back. Typically, the disk thickness d_{disk} is much smaller than the laser spot size D_{laser} , leading to a nearly one-dimensional heatflow, which is crucial for power scaling.

In a typical laser cavity, the disk is used in a comparable way to a highly reflective mirror, as a folding or end-mirror. For this reason, the thin disk concept is also sometimes referred to as the “active mirror concept”.

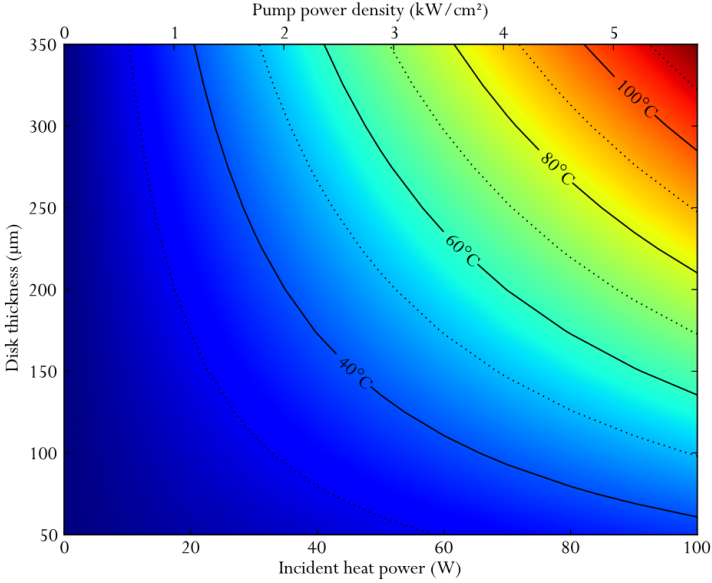


Figure 2.2: Simulation of the surface temperature of an Yb:YAG thin disk (color profile) on a diamond heatsink as a function of incident heat power on a pump spot diameter of 4.6 mm and disk thickness. The thermo-mechanical parameters for Yb:YAG are taken from reference [23].

We simulated the surface temperature of an Yb:YAG disk on a diamond heatsink as a function of its thickness and the pump power density using finite element analysis, in order to illustrate the outstanding heat removal capabilities of the TDL concept (Figure 2.2). These simulations were performed using the steady-state heat conduction equation and using the above-mentioned finite-element analysis to calculate the heat distribution in the disk. In this simplified model we neglected laser operation, and assumed that the power deposited into heat is $\approx 11\%$ of the applied pump power [24]. For a typical thickness of $\approx 200 \mu\text{m}$, the temperature rise of the surface of the disk is insignificant even at pump

power densities of $> 5 \text{ kW/cm}^2$. The advantage of using disks as thin as possible is clearly illustrated. However, an obvious compromise between heat removal, efficient absorption and manufacturing possibilities needs to be found for a given material.

Due to the very small thickness of the disk and at typical doping levels, the single-pass pump absorption is limited to a few percent (in the order of 10%). In order to overcome this limitation, a multiple pump pass arrangement was suggested by Giesen et al. in 1994 [16]. This concept is illustrated in Figure 2.3. The pump beam from a highly multimode fiber (typically fiber diameters used in our experiments have a diameter of $\approx 600 \mu\text{m}$ to $\approx 1 \text{ mm}$) is usually homogenized and then imaged on the disk with a set of collimating optics and a parabolic mirror. The disk is placed at the focus of this parabolic mirror and is pumped at an angle. The remaining pump light after each pass is recycled and reimaged on the disk by the parabolic mirror and a set of rooftop mirrors. In this figure, a 24-pass scheme is illustrated. Commercial thin-disk pumping modules are available with up to 32 passes and for pump powers up to 30 kW (Dausinger+Giesen GmbH).

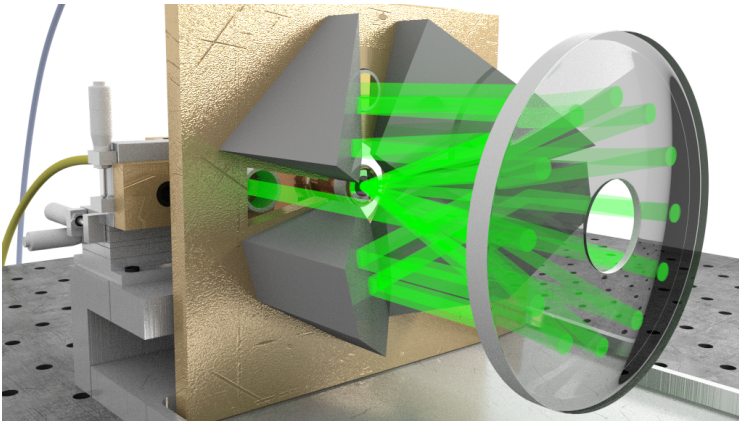


Figure 2.3: Illustration of the multiple pump pass geometry of thin-disk lasers. The pump beam is collimated and imaged on the disk at an angle. The disk is placed at the focus of a parabolic mirror. The remaining pump light after one pass is “recycled” and reimaged on the disk, allowing for efficient absorption. In this illustration, 24 pump passes through the disk are shown.

Using thinner disks and increasing the number of pump passes allows for better heat removal while maintaining a sufficient level of absorption of the pump light. However, manufacturing, coating and contacting large disks (>10 mm) suitable for power scaling with thicknesses significantly smaller than $100\ \mu\text{m}$ is challenging. In addition to the mechanical properties required to manufacture such disks, the gain material should support high doping concentrations and large absorption cross-sections for efficient pump absorption in a multi-pass pumping scheme. Furthermore, a broad gain bandwidth supporting short pulses is crucial for the targeted modelocking experiments.

In addition to the necessary spectroscopic and thermo-mechanical properties of the gain medium, transverse fundamental mode operation is required for passive modelocking, which poses extra challenges in terms of disk quality, contacting to the heatsink and resonator design.

2.1.2 Power scaling of transverse fundamental mode thin-disk lasers

Single transverse-mode operation is crucial for stable passive modelocking. One reason for this is that different transverse modes that could be supported in a laser cavity have different peak intensities and saturate the absorber at different levels. Therefore, if several transverse modes circulate in the laser cavity, this can lead to competing effects that can destabilize the modelocking process. The fundamental Gaussian mode (TEM_{00}) offers an advantage compared to other transverse modes because it exhibits the highest peak intensity and therefore benefits from lower losses of the absorber. Another important point that will be discussed in more detail in Chapter 6 is resonant coupling of transverse fundamental modes. In certain cavity configurations, coupling can occur between different transverse modes and result in beam degradation and modelocking instabilities. A strongly selective single-fundamental mode cavity should minimize these resonant coupling effects.

In this Paragraph, we will focus on the challenges of obtaining high-power fundamental transverse mode operation from TDLs. Nevertheless, it is worth noting that for certain applications, modelocking in a single higher order transverse mode, such as the TEM_{01} mode, could be of

interest. For example, modelocking in a hybrid donut mode represents an interesting option for coupling out UV light generated by intracavity HHG.

It is therefore not surprising that average power and energy scaling of passively modelocked TDLs goes hand-in-hand with progress in power scaling of TDLs operating in single fundamental transverse mode. Up-to-date, 500 W of CW power with diffraction limited beam quality ($M^2 < 1.1$) have been demonstrated using one disk [25]. During this thesis, a comparable result (430 W) was obtained, enabling the demonstration of the highest average power from a passively modelocked oscillator (Chapter 6). In the following Paragraphs, we will address in more detail different crucial points to achieve fundamental transverse mode operation from high-power TDLs.

- Resonator stability and thermal lensing

Power scaling of TDLs can be achieved by increasing both the pump power and the pump spot size at constant pump intensity. Constant pump intensity in the one-dimensional heat flow approximation does not increase the thermal load per unit area, as the cooling surface is also increased by the same amount. This scaling method has already been demonstrated successfully in the past and theoretical limits have been discussed in [17]. For very simple resonators where the output beam quality is not of primary importance, this scaling law works almost without restrictions. However, when it comes to fundamental mode operation, some resonator stability considerations have to be taken into account. In 1987, V. Magni investigated stability zones for resonators containing a variable lens [26]. He found that the tolerable variation of this lens – which in the case of a TDL mostly originates in the thermal lens of the disk – is inversely proportional to the square of the minimum spot size on this lens given by the cavity design.

For fundamental mode operation this minimum spot size corresponds experimentally to approximately 60% to 80% of the flat-top pump spot size. This stability behavior is illustrated in Figure 2.4 where one can clearly see the reduced resonator stability zones with increasing beam spot size diameters, ranging from 1 mm to 4 mm. Although in TDLs thermal

lensing arises most commonly from the gain medium, ultimately, the same effect can occur on cavity optics and the SESAM.

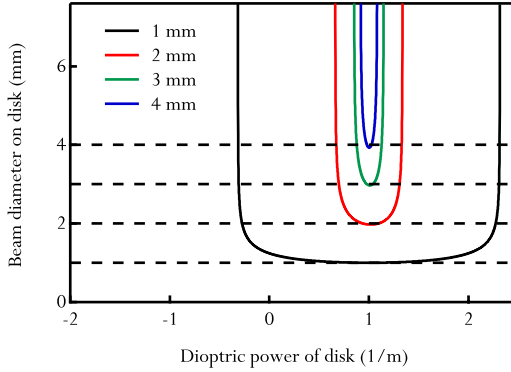
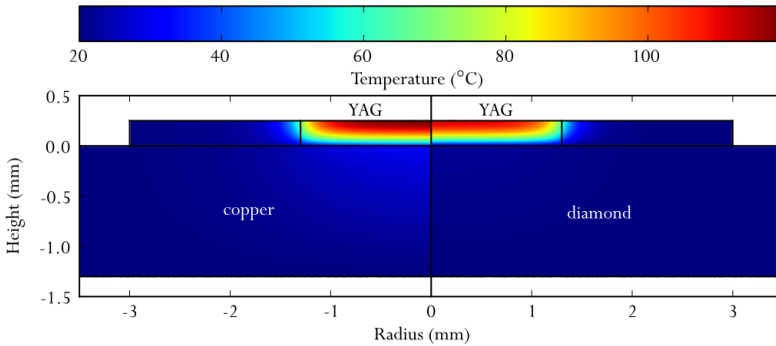


Figure 2.4: Simulations of resonator stability zone for different laser spot size diameters ranging from 1 mm to 4 mm. The width of the stability zone decreases inversely proportionally to the square of the minimum cavity mode size in this zone, which typically corresponds to 60-80% of the pump spot diameter.

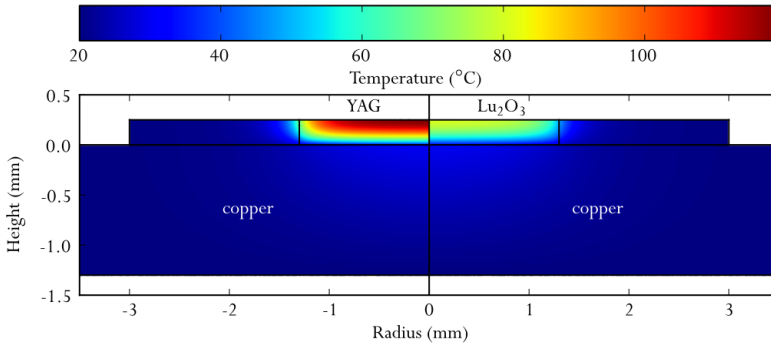
- Mounting of thin disks

The thermal lensing of a thin-disk crystal is an accumulation of different thermally induced effects like a temperature dependence of the refractive index (dn/dT), bulging, and stress due to the different thermal expansion of crystal and heatsink. Some parameters are determined by the gain material employed in the TDL, whereas others can be influenced by the choice of the mounting technique and the heatsink material. The most standard mounting technique on copper heatsinks is achieved by metallizing the HR coated side of the thin disk and using indium-tin solder. For Yb:YAG, heatsinks from copper-tungstate alloys with matched thermal expansion coefficients have been developed. Contacting Yb:YAG onto these heatsinks with indium-gold solder shows excellent performance [17].

Regarding efficient heat removal, a heatsink with a higher thermal conductivity is favorable. However, the bottleneck for efficient heat removal is the thermal conductivity of the gain material.



a) Comparison of the temperature profile of two 250 μm thick disks based on Yb:YAG on a diamond heatsink (right) and on a copper heatsink (left).



b) Comparison of the temperature profile of two 250 μm thick disks based on different materials (Yb:Lu₂O₃ (Yb:LuO) on the right and Yb:YAG on the left) but on the same copper heatsink.

Figure 2.5: Temperature profile comparison for a) two disks based on the same material but on different heatsinks, and b) disks based on materials with different thermal conductivities but on the same copper heatsink. In both simulations, a typical pump spot diameter of 2.6 mm was used. The thermo-mechanical parameters for both materials were taken at equivalent doping concentration (5at.% for LuO and 10at.% for Yb:YAG) from reference [23].

In order to illustrate this point, we simulated the temperature distribution of an Yb:YAG disk under the same pumping conditions but using different heatsink materials (copper and diamond) (Figure 2.5a). The obtained temperature profiles indicate that the heatsink has only a small

influence on the maximum temperature reached by the disk. On the other hand, we compare two materials with different thermal conductivities (Yb:YAG and Yb:Lu₂O₃ (Yb:LuO)) on the same copper heatsink (Figure 2.5b). At the equivalent doping concentration taken for these simulations, Yb:LuO has nearly double the thermal conductivity than Yb:YAG.

The choice of the heatsink and contacting method mostly influences the stiffness of the bond and the resulting thermal lensing of the thin gain medium under high pump power densities. Recently, a procedure was developed to glue disks directly on a diamond heatsink [27]. The combination of thin disks and a very thin layer of glue can result in a very stiff compound that shows only very little lensing in dependence of the incident pump power. However, the glue does not yield to any thermal stress and fatal breaking can occur if the temperature gradients within the disk or the temperature difference between disk and heatsink become too large.

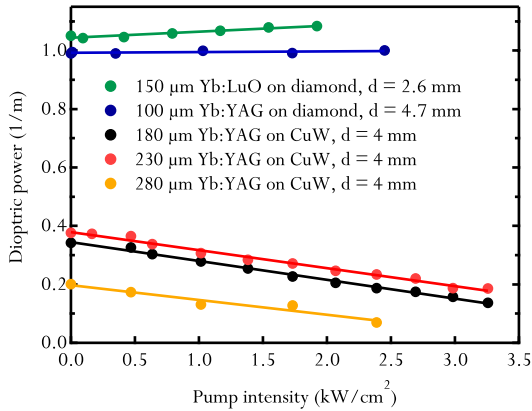


Figure 2.6: Thermal lensing measured with a polarized Michelson interferometer of different disks contacted with different methods.

Figure 2.6 shows the dioptric power of different disks contacted with different methods in dependence of increasing pump power (without laser operation) measured with a polarized Michelson interferometer. It compares gold-tin soldered Yb:YAG crystals with a thickness in the range of 180 μm to 280 μm on copper-tungstate heatsinks with a Yb:YAG disk

with a thickness of 100 μm and Yb:LuO disk with a thickness of 150 μm glued on a diamond heatsink. All Yb:YAG disks presented here were pumped at 940 nm. The Yb:LuO disk was pumped with a volume Bragg grating (VBG) [28] stabilized pump diode at 976 nm. Unfortunately, we did not have exactly the same disk parameters for these measurements but it is clearly visible that the glued disks on diamond exhibit nearly no thermal lens over a large pump intensity range. For all these measurements, we used 24 pump passes through the disk. The 100- μm thick Yb:YAG disk glued on diamond shows no variation within the measurement accuracy of 0.01 m^{-1} for a pump power intensity between 0-2.5 kW/cm^2 whereas the thicker Yb:YAG disks (180 μm to 280 μm) on copper-tungstate heatsinks show a variation of about 0.16 m^{-1} in the same range of pump power intensity. This variation is already sufficient to prevent fundamental mode operation over the whole pump power range for a pump spot diameter of 4 mm (Figure 2.4). Therefore, additional adjustments in the cavity would be required when the pump power is increased, using for example adaptable mirrors [29] or adapting of the cavity lengths to shift the center of the stability zone [30].

2.1.3 Gain materials: thermo-mechanical and spectroscopic properties

Gain materials for high-power TDLs have to meet a number of important requirements in terms of thermo-mechanical and spectroscopic properties to be suitable for high-power operation in the thin-disk geometry:

- Symmetry: Isotropic materials are better suited for power scaling. In particular, a strong anisotropy in the thermal expansion coefficients leads to asymmetric beam degradation at high power levels that cannot be compensated with standard resonator design.
- Thermal conductivity (κ): The importance of a material with a high thermal conductivity is clearly illustrated in Figure 2.5, where we simulated the temperature profiles of two disks with nearly double the thermal conductivity under the same pumping conditions.

- Thermo-optic coefficient (dn/dT): This parameter represents an important contribution to thermal lensing of the thin disk under high pump power levels. Materials with low dn/dT are preferred.
- Growth temperature: Low growth temperatures allows us to grow materials using well-established growth techniques such as the Czochralski method [31]. Most well-established gain materials used for TDLs, such as Yb:YAG, are grown using this method.
- Maximum achievable doping: high doping concentrations enable us to use thinner disks with better heat management, and therefore reach higher efficiency and better beam quality. However, it should be noted that in many gain materials, the thermal conductivity degrades with increasing doping concentration.
- Quantum defect: a small quantum defect results in a reduced thermal load on the disk.
- Absorption cross-section and bandwidth: High absorption cross-sections allow for thinner disks and therefore more efficient heat removal. A large absorption bandwidth relaxes the requirements on the pump linewidth. However, nowadays, the development of VBG stabilized diodes with output powers up to 800 W allows to efficiently pump materials with narrow absorption linewidth, such as Yb:LuO and Yb:LuScO. Several results based on such materials will be presented in this manuscript.
- Emission cross-section and bandwidth: For modelocking experiments, a wide emission bandwidth supporting ultrashort pulses is crucial. However, materials with broad emission bandwidths usually exhibit a disordered lattice structure that in turn limits their thermal conductivity - a crucial property for high-power operation. More details on the specific challenges of broadband materials for TDLs will be presented in Chapter 4, where the different trade-offs to obtain short pulses at high power levels will be discussed. High emission cross-sections are preferred since they decrease the pulse energy threshold for overcoming Q-switching

instabilities [32]. This point will be discussed in more detail in Paragraph 2.2.2 of this Chapter.

Other mechanical properties such as hardness, thermal expansion coefficients and fracture limits that are not mentioned here are also important parameters in particular for the fabrication and coating of thin and large disks. It is interesting to note that not only the host for the Yb ion needs to fulfill these requirements but also that doping should not strongly degrade these properties, which is one important challenge.

Most of the average power and energy scaling of modelocked TDLs has been achieved with Yb:YAG. This material has excellent properties for high-power TDLs and benefits from many years of industrial development. Nowadays, very thin disks ($<100\ \mu\text{m}$) with large diameters (up to several centimeters) and excellent quality are commercially available. However, other materials with the potential to outperform Yb:YAG in the thin-disk geometry have recently attracted significant attention. One promising candidate is the family of cubic sesquioxide materials. Using Yb:LuO, 140 W of average power with 738 fs pulses were obtained. This represented for several years the highest average power from a passively modelocked oscillator, showing the large potential of this material. Using the broadband mixed sesquioxide material Yb:LuScO, we demonstrated 96 fs pulses, which are the shortest pulses ever obtained from a modelocked TDL, reaching for the first time the sub-100 fs milestone. More details on these experimental results and on these materials will be given in Chapter 4.

2.2 Soliton modelocking of solid-state lasers using SESAMs

One crucial challenge for high-power modelocked TDLs is to achieve stable pulse formation at high intracavity peak powers. Typically, these lasers operate in the soliton modelocking regime, where the interplay between negative group delay dispersion (GDD) and self-phase modulation (SPM) within one round-trip of the laser resonator results in soliton pulses. In this special case, the saturable absorber is responsible for starting and stabilizing the modelocking mechanism. A detailed description of soliton modelocking can be found in [33-35]. Here, we will only give a short

overview of the important points with a special focus on the specific challenges in the case of high-power TDLs.

Semiconductor saturable absorbers mirrors (SESAMs) [4, 18, 19] are ideally suited for modelocking at high power levels, since they benefit from comparable heat removal capabilities as the thin-disk gain medium. In fact, the SESAM is also a thin structure in comparison to typical beam spot sizes, and the one-dimensional heat-flow approximation is mostly valid in this case too (Figure 2.7). In addition, this device is power scalable by increasing both the area of the beam and the pulse energy by the same factor, therefore keeping the same degree of absorber saturation. Furthermore, the macroscopic nonlinear optical parameters for modelocking can be optimized over a wide range by the design of the structure, the choice of the semiconductor absorber and the growth conditions.

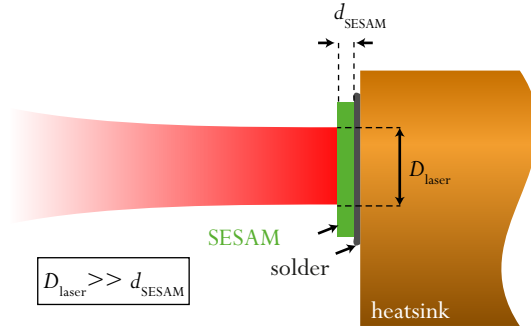


Figure 2.7: Schematic of a typical SESAM used in TDLs. In most cases, the SESAM is contacted on a copper heatsink using indium solder. The heatsink can be water-cooled or actively cooled using a Peltier element.

2.2.1 Soliton modelocking with slow saturable absorbers

In order to achieve the shortest possible pulses in a passively modelocked laser, the nonlinear phase undergone by the pulse in one roundtrip of the laser cavity and dispersion need to be in balance.

In the case of soliton modelocking of lasers based on Yb-doped solid-state gain media, phase shifts are mostly due to SPM and can be compensated by negative GDD. The saturation fluence of Yb-doped gain

materials typically used for modelocked TDLs is much larger than the pulse energy circulating in the laser cavity and resulting fluence on the disk. For example, the saturation fluence of Yb:YAG is $\approx 9 \text{ J/cm}^2$, resulting in a saturation energy of 280 mJ at a typical pump spot diameter of 2 mm. Typical pulse energies in modelocked TDLs are in the order of some tens to hundreds of μJ . Within one round trip, the gain remains undisturbed by the laser pulses and has no extra contribution to the total nonlinear phase shift of the pulses. Therefore, the total nonlinear phase shift in one round-trip is dominated by the different sources of SPM in the laser cavity. Introducing the correct amount of negative GDD results in soliton pulses circulating in the cavity. When this condition is fulfilled, the pulse duration of the soliton verifies

$$\tau_p \approx 1.76 \frac{2|D|}{\gamma E_p} \quad (2.1)$$

where τ_p is full-width half maximum (FWHM) pulse duration of the soliton, D is the total negative dispersion per roundtrip in s^2/m , E_p is the intracavity pulse energy and γ the SPM coefficient in rad/W .

Formula (2.1) indicates that the pulse formation is independent of the absorber parameters. However, the SESAM plays an essential role in starting and stabilizing the pulses. Soliton modelocking supports the formation of pulse durations significantly shorter than the absorber recovery time. Compared to the pulse, the absorber is then “slow”. In this case, a net gain window after the pulse remains where a continuum could eventually grow, and eventually destabilize the pulses. However, this continuum exhibits a narrow spectrum, and low peak power. This means negative GDD still affects this continuum but self-phase modulation is very weak. Therefore, the continuum will be stretched in time and eventually absorbed by the SESAM. This effect is illustrated in Figure 2.8.

From Formula (2.1), one could naively think that at a given pulse energy and in order to obtain shorter pulses, it is sufficient to reduce the amount of dispersion, and increase the amount of SPM via the γ parameter. This is obviously incorrect and there are both limits in terms of minimum amount of dispersion and maximum amount of tolerable nonlinearity to sustain the modelocking mechanism.

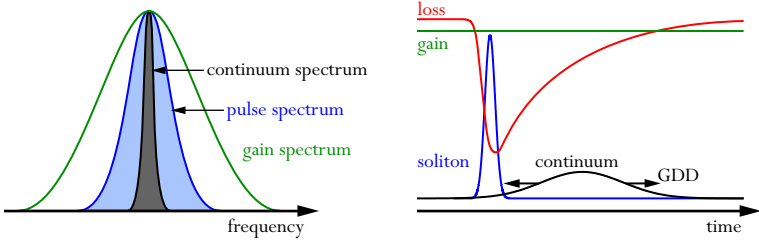


Figure 2.8: Absorber stabilization mechanism in the case of passive modelocking with slow saturable absorbers.

The minimum amount of dispersion for sufficient broadening of the continuum and therefore efficient stabilization of the soliton pulses leads to an empirical formula for the minimum achievable pulse duration in a soliton-modelocked laser [36]:

$$\tau_{p,\min} \approx \left(\frac{1}{\Delta f_g} \right)^{3/4} \left(\frac{\tau_a}{\Delta R} \right)^{1/4} \frac{g^{3/8}}{\phi^{1/8}} \quad (2.2)$$

where Δf_g is the FWHM gain bandwidth, τ_a is the absorber recovery time, ΔR is the modulation depth of the absorber, g the power gain per roundtrip, and ϕ the phase shift of the soliton.

Formula (2.2) does not take into account some important parameters, such as for example the saturation level of the absorber. In particular, it does not give information on the maximum tolerated soliton phase shift. Nevertheless, most experimental results presented in this thesis are in good agreement with this formula.

The most important parameter to achieve short pulses is the gain bandwidth of the material. Although the influence of the absorber parameters on the minimum achievable pulse duration is weak, they are crucial to push the limits in terms of pulse duration, in particular in cases where the gain bandwidth is limited. The particular requirements of SESAMs to obtain short pulses from modelocked TDLs will be treated in more detail in Chapter 3.

2.2.2 Q-switched modelocking vs. cw modelocking

During pulse build-up, competing saturation effects of the absorber and the gain medium can lead to Q-switching instabilities [32]. A simple picture to understand the reason for these instabilities is to consider a rise in the pulse energy inside the laser cavity that originates, for example, from the noise of the laser. The absorber will be more strongly saturated at a higher energy level and therefore the pulses will experience a lower loss. This leads to an exponential rise of the pulse energy. Subsequent saturation of the gain medium will have the opposite tendency and reduce the pulse energy. Depending on the saturation parameters of the absorber and the gain, these oscillations can be damped or undamped. In the case of undamped oscillations, the modelocked pulses will have a slow temporal modulation in the kHz range. This regime is referred to as Q-switched modelocking (QML) (Figure 2.9). During this regime, peak powers can be significantly higher than that of the cw-modelocked pulses, which can cause damage of different cavity components.

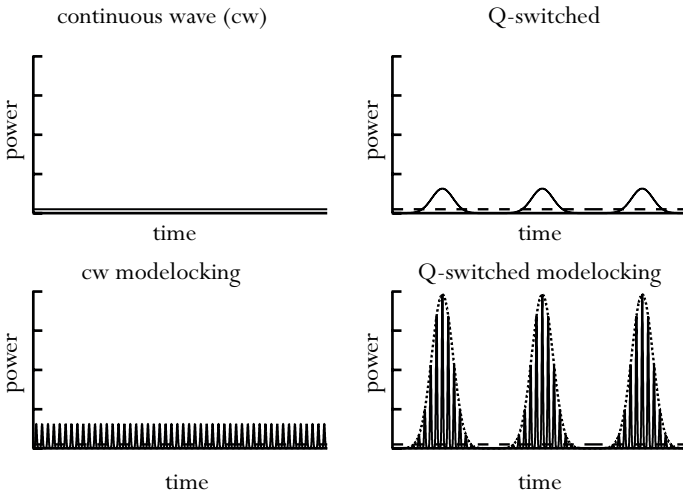


Figure 2.9: Different regimes of pulsed laser operation.

A detailed description of this regime and the intracavity pulse energy thresholds to overcome it are given in [32]. Formula (2.3) is useful to evaluate the influence of the different macroscopic parameters of SESAM and gain on this intracavity pulse energy threshold E_p :

$$E_p^2 > E_{\text{sat,g}} E_{\text{sat,a}} \Delta R \quad (2.3)$$

In this formula $E_{\text{sat,g}}$ is the saturation energy of the gain, $E_{\text{sat,a}}$ is the saturation energy of the absorber and ΔR its the modulation depth. In the case of soliton modelocking, the additional stabilizing mechanism of the soliton pulse formation makes this threshold significantly higher than observed in practice. However, this formula indicates that, in some cases, these undamped oscillations in the kHz range can be favored. Concerning the gain medium, high saturation fluences favor this QML regime. This corresponds to gain materials with low emission cross-sections, high upper-state lifetimes, and laser geometries with large spot sizes on the gain medium. On the absorber side, large saturation fluences and large spot sizes favor these undamped oscillations. In addition, a higher modulation depth will also favor QML, since for a given small rise in the pulse energy, the gain factor due to the extra saturation of the absorber is larger.

2.2.3 Semiconductor saturable absorber mirrors

- SESAM parameters

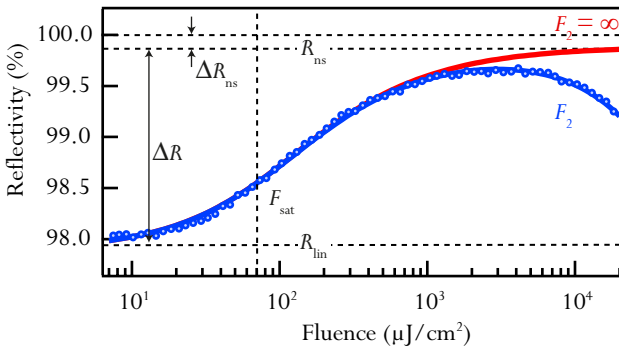


Figure 2.10: Typical SESAM response and different parameters retrieved from a least-squares fit of the experimental data. The details of the measurement and fitting procedure will be presented in detail in Chapter 3. In this example, the SESAM has a saturation

fluence $F_{\text{sat}} = 70 \mu\text{J}/\text{cm}^2$, a modulation depth $\Delta R = 1.95\%$, nonsaturable losses $\Delta R_{\text{ns}} = 0.1\%$, and an inverse saturable absorption coefficient $F_2 = 3.2 \text{ J}/\text{cm}^2$.

As we mentioned in 2.2.1, the SESAM plays an important role in the starting and stabilization of the soliton pulses. The nonlinear reflectivity of a typical SESAM is presented in Figure 2.10, together with the relevant macroscopic parameters.

The important macroscopic saturation parameters of a SESAM are:

- The modulation depth ΔR , which represents the maximum achievable change in reflectivity. Usually, this modulation cannot be reached because additional effects, such as two-photon absorption or free-carrier absorption, lead to a rollover in reflectivity at high pulse fluences that reduces the effective modulation depth.
- The nonsaturable losses ΔR_{ns} represent the unsaturable fraction of the reflectivity. These nonsaturable losses originate from defect absorption, scattering, free-carrier absorption, carrier heating, etc...
- The saturation fluence F_{sat} indicates, in the case of moderate modulation depths (up to approximately 10%), the fluence at which 1/e of the modulation depth has been saturated.
- The induced absorption (IA) coefficient F_2 characterizes the strength of the reflectivity rollover that occurs at high fluences. In the case of femtosecond pulses, two-photon absorption (TPA) is the main cause of IA [37, 38].
- The 1/e recovery time $\tau_{1/e}$ of the absorber. More details on the measurement procedure to characterize the dynamics of the absorber will be presented in Chapter 3.
 - SESAMs in thin-disk lasers

Although the appropriate absorber parameters depend on the specific laser design considered, a typical parameter range in the case of modelocked TDLs is given in Table 2.1.

- Modulation depth: Most modelocked TDLs use the disk as a single folding mirror in the cavity, resulting in 4 passes through the disk per cavity roundtrip. Due to the small thickness of the disk, the resulting gain is low and optimal output coupling rates are typically $< 10\%$. In such a configuration, a small loss modulation is sufficient to start and stabilize the pulses (typically $\Delta R < 1\%$). However, special geometries such as the one described in [21] where an increase of the overall gain per roundtrip is achieved by multiplying the number of passes through the disk, a somewhat higher modulation depth can be required. A larger modulation depth usually leads to larger nonsaturable losses, which can lead to thermal effects at high intracavity powers. Furthermore, a higher modulation depth results in a higher tendency for Q-switched modelocking. This results in trade-offs in the achievable performance.
- Saturation fluence: the requirement obviously depends on the specific resonator parameters (laser spot size on the SESAM, outcoupling rate, intracavity pulse energy). Ideal saturation parameters of SESAM modelocked ultrafast lasers are in the order of $S = 3-10$ [36], but modelocked TDLs usually operate at much higher saturation parameters (>20). In most cases, it is beneficial to operate with high saturation fluences and smaller spot sizes, because this relaxes cavity sensitivities to alignment and possible thermal lensing [26].
- Nonsaturable losses: Nonsaturable losses limit the maximum achievable reflectivity of the sample; therefore they represent an extra source of losses in the cavity. Furthermore, they contribute to heating and possible thermal lensing of the SESAM. Therefore, a lower value is desirable.
- Rollover: In order to achieve samples with high damage threshold and to shift the rollover to higher fluences, the IA coefficient F_2 should be as large as possible. This allows operating SESAMs at higher saturation level free of multiple pulsing instabilities. This point will be treated in detail in Chapter 3.

- Recovery time: Shorter recovery times allow reaching shorter pulses (Formula (2.2)). However, this is usually achieved by growing the absorber section at low temperatures [39], which results in increased nonsaturable losses. Therefore a compromise needs to be found.

All these requirements lead to challenging compromises. Up-to-date, there were no specific studies of SESAMs in the particular case of high-power lasers. During the timeframe of this thesis a specific investigation was carried out and guidelines were developed to design SESAMs with high damage thresholds. The results of this study will be presented in detail in Chapter 3.

	Typical range	Highest average power [14]	Highest pulse energy* [21]	Shortest pulse duration [40]
F_{sat}	30-200 $\mu\text{J}/\text{cm}^2$	140 $\mu\text{J}/\text{cm}^2$	61 $\mu\text{J}/\text{cm}^2$	90 $\mu\text{J}/\text{cm}^2$
ΔR	0.5-3%	0.95%	3.5%	1.2%
ΔR_{ns}	0-1%	0.1%	NC	0.4%
$\tau_{1/e}$	1-300 ps	67 ps	NC	2 ps
F_2	$>3 \text{ J}/\text{cm}^2$	$\approx 30 \text{ J}/\text{cm}^2$	NC	$\approx 6.5 \text{ J}/\text{cm}^2$
τ_p	-	583 fs	1.1 ps	96 fs
P_{av}	-	275 W	145 W	5 W
T_{oc}	-	11%	70%	2.6%

*Multiple gain passes configuration - NC: not characterized

Table 2.1: Typical SESAM parameters in SESAM modelocked TDLs.

2.3 Challenges of high-power modelocking

2.3.1 Q-switching instabilities

As we mentioned already in 2.2.1, typical Yb-doped gain materials used in TDLs have high saturation fluences. Furthermore, large spot sizes on the disk (of several mm) are commonly used to achieve high power levels. On the absorber side, we saw in the previous Paragraph that large saturation fluences are beneficial to achieve these high power levels in comfortable cavity conditions. All these parameters contribute to a high QML threshold. In most cases, TDLs reach large enough pulse energies for this not to be a serious issue. However, there are specific situations where special attention needs to be paid in order to avoid damage of different components in the cavity during this regime. For example, when the goal is to generate short pulses from modelocked TDLs, the gain emission cross-sections tend to be low and a high-modulation depth is beneficial. In this case QML can be one of the main limiting factors.

2.3.2 Excessive nonlinearities

One of the most crucial limitation for high-power modelocking is an excessive nonlinear phase shift that can destabilize modelocked operation in the soliton modelocking regime [34, 36]. In a typical cavity for a soliton modelocked TDL (Figure 2.11), the circulating pulse experiences SPM by propagating through nonlinear materials like the gain medium, a Brewster plate and the air atmosphere. A Brewster plate is most commonly used to obtain a linearly polarized output and for fine adjustment of the SPM by placing it at a position in the cavity where there is a focus. Negative dispersion is introduced with dispersive mirrors throughout the cavity.

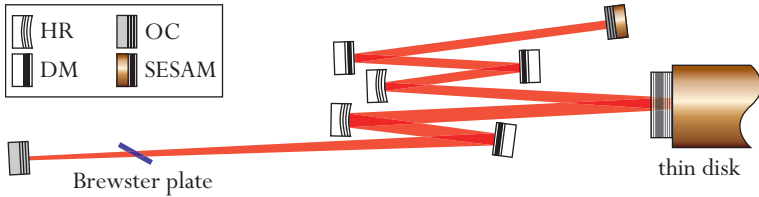


Figure 2.11: Typical layout of a modelocked TDL cavity.

The total nonlinear phase shift ϕ_{nl} undergone by the pulse during one round trip of the cavity can be calculated with

$$\phi_{\text{nl}} = 2 \cdot \frac{2\pi}{\lambda} \int_{\text{cav}} n_2(z) I(z) dz \quad (2.4)$$

Most commonly, the γ -factor (in mrad/MW) is used, which is independent of the pulse parameters but takes into account the different spot sizes of the beam throughout the cavity.

$$\phi_{\text{nl}} = 4 \cdot \frac{2\pi}{\lambda} P_{\text{pk}} \int_{\text{cav}} \frac{n_2(z)}{A(z)} dz = P_{\text{pk}} \cdot \gamma_{\text{cav}} \quad (2.5)$$

Therefore, the γ -factor can be written as:

$$\gamma_{\text{cav}} = 4 \cdot \frac{2\pi}{\lambda} \int_{\text{cav}} \frac{n_2(z)}{A(z)} dz \quad (2.6)$$

Different elements in the cavity contribute to the total γ -factor:

$$\gamma_{\text{cav}} = 4 \cdot \frac{2\pi}{\lambda} \left[\int_{\text{disk}} \frac{n_{2,\text{disk}}(z)}{A(z)} dz + \int_{\text{cav}} \frac{n_{2,\text{air}}(z)}{A(z)} dz + \int_{\text{BP}} \frac{n_{2,\text{BP}}(z)}{A(z)} dz + \dots \right] \quad (2.7)$$

- Gain material:

$$\gamma_{\text{disk}} = 4 \cdot \frac{2\pi}{\lambda} d_{\text{disk}} \frac{n_{2,\text{disk}}}{A_{\text{disk}}} \quad (2.8)$$

The SPM from the disk can typically be neglected as the mode size A_{disk} is large and the pulse passes only through very little material $d_{\text{disk}} \ll A_{\text{disk}}$.

- Brewster plate:

$$\gamma_{\text{BP}} = 4 \cdot \frac{2\pi}{\lambda} d_{\text{BP}} \frac{n_{2,\text{BP}}}{A_{\text{BP}}} \quad (2.9)$$

Most commonly, the Brewster plate is thin enough to consider the size of the beam constant. If this is not the case, a simple integration on the z-direction is straightforward. The influence of the Brewster plate can be controlled by the choice of the thickness, the material and the mode size at the location in the cavity where it is placed. Usually, the Brewster plate is desirable as it offers some control over the total amount of SPM and ensures linear polarization of the laser output. In cavities where a fine control of the SPM can be achieved otherwise (for example with the air pressure in laser oscillators operated in vacuum, see Chapter 6), a thin-film

polarizer can be used to select the polarization, and the Brewster plate can be completely eliminated.

- Air atmosphere:

$$\gamma_{\text{atm}} = 4 \cdot \frac{2\pi}{\lambda} \int_{\text{cav}} \frac{n_{2,\text{atm}}(z)}{A(z)} dz \quad (2.10)$$

The contribution of the air atmosphere was initially ignored, since the nonlinear refractive index $n_{2,\text{atm}}$ is orders of magnitude smaller than the refractive index of, for example, a fused-silica Brewster plate. However, typical TDLs have cavity lengths in the order of several meters to several tens of meters. Furthermore, in most modelocked TDLs, the intracavity peak power is substantially higher than the output peak power and can exceed 100 MW [14, 41]. Thus, the intracavity SPM introduced by the ambient air in the cavity can become the main contribution to the total soliton phase shift [42]. In order to compensate for this phase shift and obtain stable soliton modelocking, large amounts of negative GDD are required. In addition, if these phase shifts become too large, the pulse formation mechanism is destabilized limiting power and energy scaling.

Different approaches have been suggested in the past years to overcome this limitation:

- Flooding the resonator with helium
- Decreasing the ratio between intracavity peak power and output peak power by increasing the output coupling rate and the overall roundtrip gain. This can be achieved by increasing the number of gain passes on the disk or by using several disks in one oscillator.
- Operation of the oscillator in a vacuum environment

These different approaches will be discussed in more detail in Chapter 6, where the last point is demonstrated for the first time.

- Cavity optics:

The nonlinearity introduced by the coatings of different cavity optics was, up-to-date, always considered negligible. However, we will see in Chapter 6 that they can become an important contribution to the total soliton phase shift at extreme intracavity peak powers.

2.3.3 Thermal effects and damage

Ultimately, thermal effects and damage that occur in different cavity components limit average power scaling of modelocked TDLs. This is particularly the case in simple oscillator geometries where a low number of gain passes is used and the circulating intracavity power can reach several kW of average power.

- **Gain medium:** In most bulk lasers, thermal aberrations that occur in the gain medium limit the achievable output power. As we have discussed in the first Paragraph of this Chapter, TDLs are very well suited to partially overcome this limitation. Significant efforts have been dedicated in the past years to optimize the heat management and thermal aberrations from the thin gain medium. In the case of standard gain materials like Yb:YAG, disks with insignificant thermal lensing are commercially available, such as the one used in the experiment presented in Chapter 6. For novel gain materials such as Yb:LuO or Yb:LuScO, a small residual thermal lensing can be compensated for by adapting the resonator design. This was the case in the demonstration of 140 W from a modelocked Yb:LuO TDL, where the resonator arms needed to be adjusted at different pump power levels to compensate for the thermal lens of the disk and achieve fundamental transverse mode operation [30].
- **SESAM:** For a long time, the SESAM was thought to be the bottleneck for power-scaling of modelocked TDLs. Contradictory information about the damage threshold of such devices was reported, and no thorough investigation was carried out prior to this thesis. In Chapter 3, we will present a study of SESAMs for high-power oscillators where we derive simple guidelines to obtain high-damage threshold and optimized absorber parameters. These guidelines were used to design the SESAM used in the experiment presented in Chapter 6, where we could demonstrate the highest average power from any ultrafast oscillator with 275 W [14]. Currently, the SESAM does not represent the limiting factor towards higher average powers.

- Dispersive mirrors: A more important yet often-ignored problem is thermal management and nonlinearities that can occur in the dispersive mirrors required for soliton modelocking. Most commonly, Gires Tournois Interferometer (GTI)-type mirrors are used because they can provide large amounts of negative dispersion [43, 44]. However, these mirrors rely on field resonances that can cause thermal and nonlinear effects. Currently, scaling of TDLs to more than 275 W of average power is limited by thermal effects observed in such dispersive mirrors [14].

2.4 Outlook

For further average power scaling to the kilowatt level, pump spot diameters on disk has to be increased. This sets severe demands on the applicable thin disk crystal properties and mounting techniques. Currently, Yb:YAG thin-disks mounted with glue on diamond appear to be the best candidates for this future step. Nevertheless, novel materials such as Yb:LuO have a large potential to outperform Yb:YAG in terms of efficiency and pulse duration, when growth and contacting techniques are perfected.

Several points presented in the previous Paragraph seem to suggest that reducing the intracavity power by increasing the overall gain of the system (using several disk in the oscillator or with multiple gain passes on the same disk) and choosing a higher output coupler transmission is the best alternative for further power scaling. However, in both these cases, it is not straightforward to achieve fundamental mode operation. In the first case, resonator design is complex since each disk can show a different thermal lensing behavior. The second approach of an active multi-pass cell in a mode-locked TDL has been introduced by Neuhaus et al. [45, 46] and has demonstrated impressive performance. However, increasing the number of passes on the gain significantly increases the demands on the disk quality. Figure 2.12 shows how the thermal lensing stability zones decrease with an increasing number of passes over the disk. The comparison between a single pass (i.e. two passes in one roundtrip, black line) and five passes over the disk (blue line) reveals a shrinking of the overall stability

zone by a factor of about five, showing that only negligible thermal lensing could be tolerated in such a multi-pass arrangement.

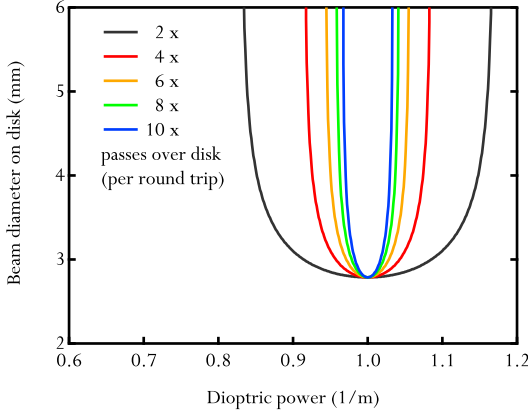


Figure 2.12: Simulations of the stability zones of an active multi-pass resonator for different numbers of passes over the disk. This graph compares the stability zones from a single pass (i.e. two passes in one round trip, black line) up to 5 passes (blue line).

Therefore, it seems more likely that the next step towards several hundred watts of average power with pulse energies in the order of $100 \mu\text{J}$ will be achieved with a single- or only a few-pass resonator in a vacuum atmosphere similar to the latest demonstrated power scaling results (Chapter 6) [14].

In terms of dispersion management, new thermally improved designs for GTI-type mirrors will be one of the crucial steps in further power scaling steps. Furthermore, the novel high-damage threshold SESAM designs will be presented as an outlook of Chapter 3, and represent a key element for these future oscillators.

Chapter 3 - SESAMs for high-power femtosecond oscillators

As we mentioned in the previous Chapter, the excellent power scalability of the TDL technology should soon allow for kilowatt fundamental transverse mode oscillators suitable for SESAM modelocking. Possible SESAM limitations were, so far, not thoroughly studied and contradictory information on damage thresholds and losses was reported. Previous investigations on optimized SESAM designs mostly focused on the realization of low saturation fluences [47, 48], which is important for modelocked high repetition rate lasers and stable modelocking of semiconductor lasers [49]. This study resulted in fundamentally modelocked laser oscillators with record-high repetition rates up to 160 GHz in the 1- μm spectral region [50] and 100 GHz in the 1.5- μm telecom spectral region [51], and the development of new ultrafast integrated semiconductor lasers (MIXSELS) [52].

SESAMs for high-power ultrafast TDLs operate in a completely different regime than the above-mentioned modelocked lasers. Pulse energies and average power levels in ultrafast TDLs are several orders of magnitude higher. In Table 3.I, we present typical SESAM operation parameters in recently demonstrated high-power thin-disk oscillators. We notice that in such oscillators SESAMs operate at kilowatt intracavity power levels, peak intensities of tens of gigawatts per square centimeter, and fluences above the millijoule per square centimeter level. A useful parameters to describe the operation point of a SESAM in a certain oscillator is the saturation parameter $S = F/F_{\text{sat}}$. Typical SESAM modelocked lasers operate at $S = 3\text{--}10$ [36], but stable operation was demonstrated in high-energy oscillators at saturation parameters $S > 20$ (see Table 3.I).

	Yb:YAG [14]	Yb:YAG [21]	Yb:LuO [30]
Average output power	275 W	145 W	141 W
Repetition rate	16.3 MHz	3.5 MHz	60.0 MHz
Pulse duration	580 fs	1100 fs	740 fs
Output pulse energy	17 μ J	41 μ J	2 μ J
Output peak power	26 MW	33 MW	2.8 MW
Intracavity average power	2.5 kW	0.2 kW	1.5 kW
Intracavity pulse energy	154 μ J	57 μ J	25 μ J
Intracavity peak power	236 MW	46 MW	30 MW
Spot radius on SESAM ($1/e^2$)	1.2 mm	0.55 mm	0.63 mm
Fluence on SESAM	3.4 mJ/cm ²	6 mJ/cm ²	2 mJ/cm ²
Average intensity on SESAM	55 kW/cm ²	21 kW/cm ²	12 kW/cm ²
Peak intensity on SESAM	5.2 GW/cm ²	4.8 GW/cm ²	5 GW/cm ²
Saturation fluence of SESAM	140 μ J/cm ²	61 μ J/cm ²	60 μ J/cm ²
Saturation parameter ($S=F/F_{\text{sat}}$)	24	100	33

Table 3.I: Typical levels of operation of SESAMs in state-of-the-art high-power SESAM modelocked TDLs.

Therefore, SESAMs for high-power oscillators require

- large saturation fluences,
- high damage thresholds,
- low nonsaturable losses to avoid thermal effects, and
- low induced absorption (IA), which is responsible for the reflectivity rollover at high fluences and can lead to multi-pulsing instabilities [37, 53, 54].

During the time frame of this thesis, we extended previous studies to the specific case of SESAMs for high-power oscillators. We present the first detailed study on damage thresholds and lifetime of different representative samples. We focus on how to tailor and combine these parameters, and present additional guidelines in the specific case where recovery time and modulation depth of the absorber are of interest. This is the case, for example, in high-power oscillators where the aim is to achieve short pulse durations (sub-200 fs).

This Chapter will be divided in three parts. In Part I, we investigate damage of samples with different absorber sections and topcoatings, but in all cases, negligible nonsaturable losses. For this case, we designed SESAMs with multiple quantum wells (QWs) in a standard antiresonant configuration with suitable dielectric topcoatings and obtained samples with increased saturation fluence, damage threshold as well as reduced nonsaturable losses and IA. We conclude by indicating guidelines for SESAMs for high-power oscillators with high-damage thresholds.

In Part II, we extend these studies to the specific case of SESAMs with short recovery times, designed to achieve short pulses from modelocked TDLs. In this case, the influence of the growth temperature and resulting nonsaturable losses on the damage threshold of the samples is investigated. Extra guidelines are presented on how to design SESAMs achieving the required compromises.

In Part III, we summarize the findings of our damage investigation and give an outlook for improved SESAM designs for future kilowatt-level oscillators.

Part I - Damage thresholds, lifetime and design guidelines

3.1 Experimental setup and SESAM characterization

3.1.1 Experimental Setup

In order to reach the high fluences necessary to carry out this study, we used a high-energy SESAM modelocked Yb:YAG thin-disk oscillator seeding a high-precision nonlinear reflectivity measurement setup [55] to characterize nonlinear reflectivity, IA, and damage of our SESAMs. This allowed us to test our SESAMs up to an unprecedentedly high fluence level of 0.21 J/cm^2 , corresponding to a peak intensity of 185 GW/cm^2 .

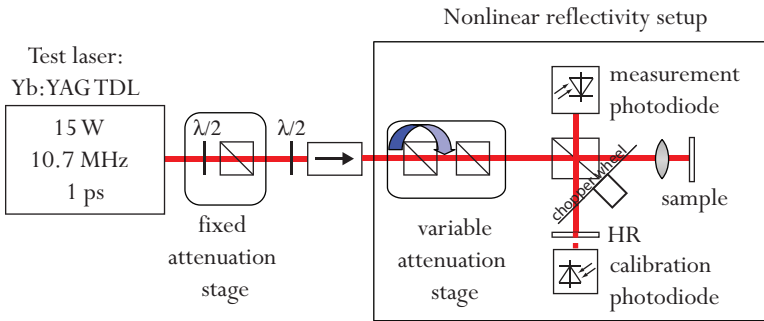


Figure 3.1: Experimental setup used for the nonlinear reflectivity characterization and damage measurements.

The experimental setup is presented in Figure 3.1. The SESAM modelocked Yb:YAG TDL delivers 15 W of average power at a repetition rate of 10.7 MHz, corresponding to a pulse energy of 1.4 μJ in 1-ps pulses. We used a lens with a focal length $f = 20 \text{ mm}$ resulting in a spot size diameter of $17.9 \mu\text{m}$ on the sample. At the maximum available power, this resulted in a maximum fluence of 0.21 J/cm^2 , which is 30 times higher than previous measurements of high-power SESAMs [55]. The fixed

attenuation stage was used to set the maximum fluence level for a given measurement. In this way, one can benefit from the full range of the variable attenuation stage even for samples with moderate saturation fluences and damage thresholds.

The variable attenuation stage enables us to access a pulse fluence range of more than four orders of magnitude. We use a highly reflective (HR) mirror with a specified reflectivity of 99.98% at 1030 nm (Layertec GmbH) for reflectivity calibration. A typical measurement obtained with this setup is presented in Chapter 2, Figure 2.10.

3.1.2 Characterization of the nonlinear reflectivity parameters

Formula (3.1) describes the fluence-dependent SESAM reflectivity $R(F)$ for a flat-top-shaped beam profile [56]:

$$R(F) = R_{\text{ns}} \frac{\ln \left(1 + \frac{R_{\text{lin}}}{R_{\text{ns}}} \left(e^{\frac{F}{F_{\text{sat}}}} - 1 \right) \right)}{\frac{F}{F_{\text{sat}}}} e^{-\frac{F}{F_2}} \quad (3.1)$$

The fitting procedure used for our measurements is based on this formula but is numerically corrected for a Gaussian-shaped transverse beam. A least-squares fit procedure yields the saturation parameters of the SESAM (saturation fluence F_{sat} , modulation depth $\Delta R = R_{\text{ns}} - R_{\text{lin}}$, nonsaturable losses $\Delta R_{\text{ns}} = 1 - R_{\text{ns}}$, IA coefficient F_2). These parameters are illustrated in Chapter 2, Figure 2.10.

3.1.3 Importance of the induced absorption (IA) coefficient F_2

Operation at high incident pulse fluences on the SESAM compared to its saturation fluence (i.e., high S -parameter, see Table 3.I) makes multi-pulsing instabilities a more critical issue in TDLs. It is, therefore, of particular importance for high-power oscillators to correctly characterize the IA coefficient F_2 that describes the additional absorption observed at high fluences. We usually refer to this effect as a “rollover” in reflectivity. Although this rollover is beneficial to suppress Q-switching instabilities, operating the SESAM close to this rollover can lead to multi-pulsing

instabilities [37, 53, 54]. The reason for this is that pulse breakup results in several pulses circulating in the cavity, which are less energetic than one single pulse at a given average power. Operating in a SESAM range where the reflectivity increases with pulse fluence results in single pulses experiencing fewer losses therefore being favored. If the SESAM is over-saturated due to IA, multiple pulses with lower pulse energy can have a gain advantage compared to single pulses and be favored.

The F_2 parameter, typically expressed in mJ/cm^2 , describes the strength of the rollover and is taken into account as an additional parameter in the reflectivity function for the fitting procedure (Formula (3.1)).

Another relevant parameter that can be extracted using the nonlinear reflectivity curve is the fluence F_0 , where the maximum reflectivity is reached. This parameter is related to the IA coefficient F_2 (for weak IA coefficients ($F_0 > 5F_{\text{sat}}$) and small modulation depths) [37] by:

$$F_0 = \sqrt{F_2 F_{\text{sat}} \Delta R} \quad (3.2)$$

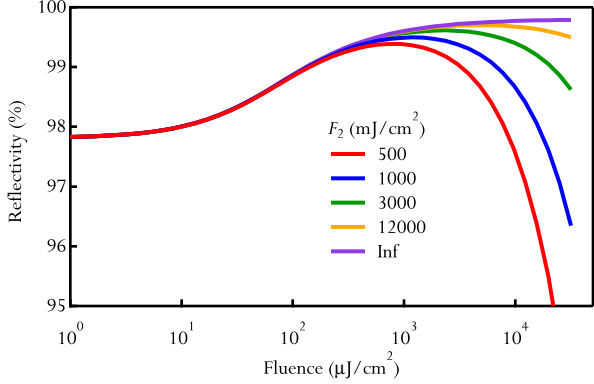
Due to the relatively long pulse duration of the laser source used in this study (1 ps) and the resulting weak rollover, these approximations are fulfilled in all cases considered here. Although F_0 may appear as a more intuitive parameter, F_2 is independent of the SESAM parameters, whereas F_0 depends on the product $F_{\text{sat}} \cdot \Delta R$. This makes F_2 a well-suited parameter to compare IA of different SESAMs. F_2 can be calculated in the case of two-photon absorption (TPA) and for sech^2 pulses using

$$F_2 = \frac{\tau_p}{0.585 \int_{\text{struct}} \beta_{\text{TPA}}(z) n^2(z) |E(z)|^4 dz} \quad (3.3)$$

with z the vertical position within the wafer structure, $\beta_{\text{TPA}}(z)$ the TPA coefficient expressed in cm/GW , $E(z)$ the normalized electric field in the structure, and $n(z)$ is the refractive index. This formula gives a good approximation of the measured rollover for femtosecond pulses. For longer pulses, the observed F_2 is larger than calculated if only TPA is taken into account. The exact reason for this stronger IA for longer pulses has not yet been clearly elucidated [37].

Figure 2.10 illustrates the influence of the IA coefficient F_2 when F_{sat} , ΔR , and ΔR_{ns} are kept constant. As we can see, the effective modulation depth of the sample is reduced.

Figure 3.2: Effect of the F_2 parameter on the nonlinear reflectivity at given saturation parameters (in this case $F_{sat} = 50 \mu\text{J}/\text{cm}^2$, $\Delta R = 2\%$, $\Delta R_{ns} = 0.2\%$) and different F_2 parameters.



3.2 Design of the SESAMs under test

A straightforward approach to increase the saturation fluence of a SESAM is to grow a top mirror on the structure to increase its finesse. In this way, the electric field in the absorber layers is reduced, and therefore, the fluence required to saturate the sample is increased. As we increase the saturation fluence, we reduce the modulation depth of the sample by the same factor, since

$$\Delta R \cdot F_{sat} = F_t \quad (3.4)$$

where F_t is the transparency fluence of the absorber. The transparency fluence F_t , is related to the transparency density N_t by:

$$F_t = dh\nu N_t \quad (3.5)$$

where N_t is the 2-D transparency density of the QW absorber, $h\nu$ is the incident photon energy and d is the thickness of the QW. The transparency density N_t only depends on material composition, wavelength and confinement, which are all intrinsic properties of the absorber. The detailed calculation of this transparency density as a function of the intrinsic semiconductor parameters is described in [38, 57]. However, in this case,

we are mostly interested in the link between the transparency fluence and the macroscopic parameters of the SESAM, namely F_{sat} and ΔR .

The energy per area absorbed by the sample F_{abs} at any given incident fluence F is:

$$F_{\text{abs}}(F) = F(1 - R(F)) \quad (3.6)$$

The condition for transparency in the case on negligible nonsaturable losses and no IA is given by

$$F_t = \lim_{F \rightarrow \infty} F(1 - R(F)) \quad (3.7)$$

Using Formula (3.1), we obtain

$$F_t = F_{\text{sat}} \ln \left(\frac{1}{R_{\text{lin}}} \right) \approx F_{\text{sat}} \ln(1 + \Delta R) \approx F_{\text{sat}} \cdot \Delta R \quad (3.8)$$

The product $F_{\text{sat}} \cdot \Delta R$ remains constant for a given absorber section since the transparency density is an intrinsic material property. An additional top-mirror on a given SESAM will, therefore, increase its saturation fluence and decrease its modulation depth. This means that the samples to topcoat need to have a large enough modulation depth in addition to the basic requirements (i.e. low nonsaturable losses and an initially large saturation fluence). With multiple QWs, we can adjust the modulation depth without changing the saturation fluence of the samples.

3.2.1 SESAM structures grown for damage investigations

In Figure 3.3, we present the design of the non-topcoated SESAM (NTC) used for this study. It consists of a 30-pair GaAs/AlAs distributed Bragg reflector (DBR) and three 10-nm InGaAs QWs as absorber layers in an antiresonant configuration. This SESAM was grown by molecular beam epitaxy (MBE) in the FIRST cleanroom facility at ETH Zurich. The QWs of this sample were grown at $T \approx 400^\circ\text{C}$, resulting in a recovery time at $1/e$ of $\tau_{1/e} \approx 200$ ps and low nonsaturable losses $< 0.1\%$. Lower MBE growth temperatures would support shorter recovery times, but an increased number of defects and higher nonsaturable losses [39]. In this first Part, we target an investigation of the damage mechanism in SESAMs. Therefore, it is crucial to isolate the possible causes of damage. Using samples with negligible nonstaurable losses allows us to assume that

damage cannot occur by heat deposition in the absorber. In the next Part of this Chapter, a separate study on the exact effect of the recovery time of the absorber on the damage parameters will be presented in the context of modelocked TDLs with short pulses (sub-200 fs).

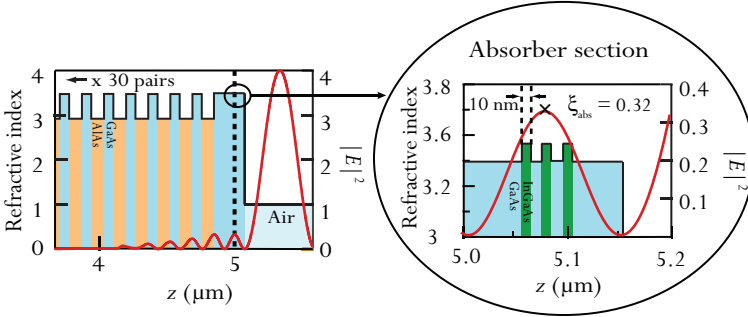


Figure 3.3: SESAM structure without topcoating used for the damage study. Different topcoatings will be applied on this structure.

3.2.2 Topcoating section

Three different topcoatings were grown on this structure (Figure 3.4). In the first case, a semiconductor topcoating was chosen with four pairs of quarter-wave GaAs/AlAs layers grown by MBE (semiconductor topcoating (SCTC), see Figure 3.4b). In this design, the field enhancement in the absorber is reduced by a factor of ≈ 4 compared to the uncoated sample (see Figure 3.4d). Therefore the same increase of the saturation fluence is expected. For the other cases, a dielectric $\text{SiO}_2/\text{Si}_3\text{N}_4$ topcoating grown by plasma-enhanced chemical vapor deposition (PECVD) was chosen. Two sets of samples were coated with two and three pairs of quarter-wave layers (DTC2 and DTC3, see Figure 3.4c). In this case we expect an increase of the saturation fluence of a factor of 3 and 5, respectively (Figure 3.4d). These dielectric topcoatings are particularly attractive because the deposition process is much simpler and considerably more cost efficient than an MBE topcoating. Furthermore, the dielectric topcoating can be applied after MBE growth. This allows for additional flexibility in terms of finesse increase of the structure. From a material point of view, SiO_2 and

Si_3N_4 are dielectric materials, and therefore exhibit negligible TPA compared to GaAs and AlAs [58], which results in reduced IA.

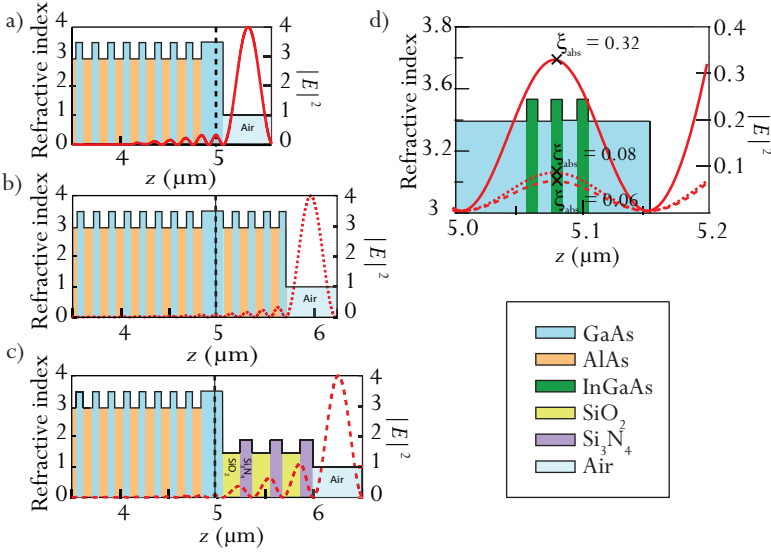


Figure 3.4: Different SESAM structures used for the damage study. a) SESAM design (also presented in Figure 3.3) with 3 QWs and no topcoating (NTC), b) same SESAM but with a 4-quarter-wave-pair GaAs/AlAs semiconductor topcoating (SCTC), c) same SESAM but with a 3-quarter-wave-pair $\text{SiO}_2/\text{Si}_3\text{N}_4$ dielectric topcoating (DTC3), d) field enhancement in the absorbers.

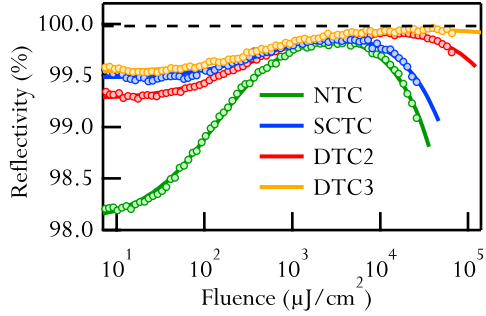
3.3 Nonlinear reflectivity, damage thresholds and lifetimes

3.3.1 Nonlinear reflectivity

	F_{sat} ($\mu\text{J}/\text{cm}^2$)	ΔR (%)	ΔR_{ns} (%)	F_2 (mJ/cm^2)
NTC	72	2.05	<0.1	3200
SCTC	279	0.52	<0.1	5500
DTC2	168	0.71	<0.1	31700
DTC3	247	0.43	<0.1	346000

Table 3.II: Saturation parameters of the different samples, extracted from the measurements presented in Figure 3.5 with the fit function described in Formula (3.1).

Figure 3.5: Nonlinear reflectivity measurement of the different samples used in this study, illustrating the effect of the different applied topcoatings.



The nonlinear reflectivity measurements and corresponding extracted parameters are presented in Figure 3.5 and Table 3.II. We can clearly see the effect of the different topcoatings on the saturation parameters of the samples: as the saturation fluence increases, the modulation depth decreases by a similar factor. The saturation fluences of all the topcoated samples are $> 150 \mu\text{J}/\text{cm}^2$ and their modulation depths are between 0.4% and 0.8%. SESAMs used in high-power TDLs typically have modulation depths in this range (Table 3.I). This makes all our fabricated SESAMs excellent candidates for such systems. The 3-QW non-topcoated sample with 2% modulation depth is ideally suited for topcoatings designed for a saturation fluence increase of 3–5. All SESAMs have negligible nonsaturable losses $< 0.1\%$ and therefore minimal thermal load.

All topcoated SESAMs have increased IA coefficients F_2 compared to that of the non-topcoated sample. However, the semiconductor topcoated SESAM (SCTC) shows only a small increase compared to the dielectric topcoated samples (DTC2 and DTC3). Although the field in the DBR structure and the absorber section is reduced in all samples, the GaAs/AlAs topsection experiences a strong electric field, and GaAs has a strong TPA coefficient. In the case of the dielectric topsection, both materials have a negligible TPA coefficient compared to GaAs. Therefore, SESAMs with similar saturation parameters (similar electric field distributions in the DBR and the absorber region) but different topcoatings have different IA responses.

Using Formula (3.3), the expected F_2 parameter only taking into account TPA was calculated for all our fabricated structures and assuming a pulse duration of $\tau_p = 1\text{ps}$ (pulse duration of the TDL used for the measurements). For this calculation, the TPA coefficients of AlAs, SiO_2 , and Si_3N_4 are considered negligible compared to that of GaAs, and we used $\beta_{\text{TPA,GaAs}} = 20\text{ cm/GW}$ [58]. The results are summarized in Table 3.III.

	$F_{2,\text{meas}}$ (mJ/cm^2)	$F_{2,\text{TPA}}$ (mJ/cm^2)	$F_{2,\text{TPA}}/F_{2,\text{meas}}$
NTC	3200	8200	2.56
SCTC	5500	15000	2.71
DTC2	31700	70200	2.21
DTC3	346000	206000	0.6

Table 3.III: Comparison of the measured IA coefficient $F_{2,\text{meas}}$ and the calculated $F_{2,\text{TPA}}$ (only considering TPA).

For the SESAM with the 3-pair dielectric topcoating (DTC3), the available power limits the measurement accuracy of F_2 . As we can see in Figure 3.5, the maximum fluence does not allow measuring deep enough into the rollover; therefore, F_2 could not be measured with enough accuracy for this SESAM. For all other SESAMs, there is a factor of ≈ 2.5 between the calculated and measured F_2 (Table 3.III), indicating that the observed rollover is stronger than predicted only by TPA for this pulse duration. This is due to the relatively long pulses we used in the study. Indeed, it was shown in [37] that the rollover observed in the picosecond regime was stronger than that predicted by TPA only in similar structures. The observed factor of around 2-3 seems to be in good agreement with the previous above mentioned study carried out with 3-ps long pulses.

3.3.2 Damage fluence and time-to-damage measurement procedure

We define damage of a SESAM under test as an irreversible change in the structure resulting in a dramatic drop in the measured reflectivity. The damage fluence threshold F_d is then defined as the minimum fluence where this irreversible reflectivity drop occurs in $<1\text{ s}$. In order to measure the

damage fluence and the time-to-damage of a sample we use the same setup described in the first section for nonlinear reflectivity measurements. We set the fluence to a constant value and track reflectivity of the sample versus time. A typical measurement trace is shown in Figure 3.6 (left).

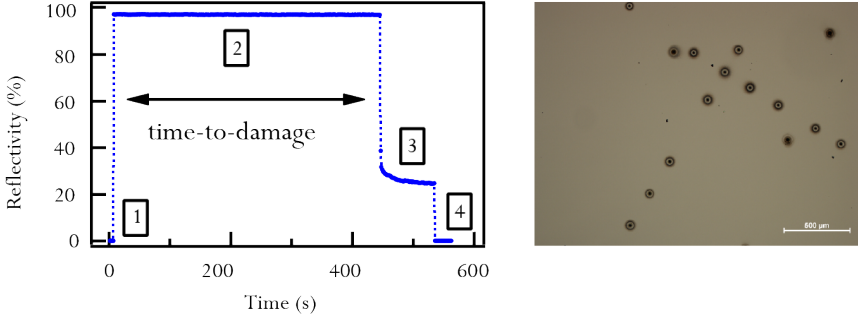


Figure 3.6: Left: Typical time-to-damage measurement. In this example, we measured a time-to-damage of 445 s at a fluence of $27 \text{ mJ}/\text{cm}^2$, corresponding to a fluence 65% lower than the damage threshold. Right: Image of a tested SESAM where we can see multiple damage spots resulting from the performed characterization.

First, the fluence is set to the desired value while the sample arm is blocked (1). The measurement of reflectivity versus time is then started, and the laser is focused onto the sample. The time before the irreversible reflectivity drop (2) is what we define as “time-to-damage”. One reflectivity measurement point lasts typically around 1 s, and the precision of the measurement is, therefore, limited to this duration. The observed drop in reflectivity is stronger when damage occurs at higher fluences, but typically the drop amounts to $\approx 50\text{--}90\%$ of the initial reflectivity of the non-damaged sample.

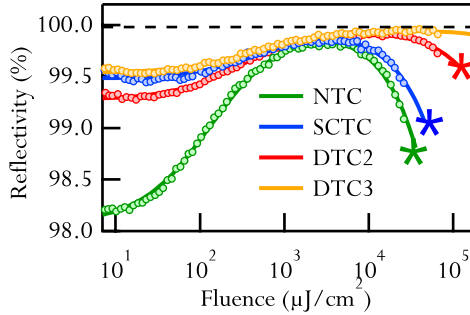
In order to find the damage threshold, we first scan the fluence in steps of approximately $5 \text{ mJ}/\text{cm}^2$ starting at around $100 \cdot F_{\text{sat}}$ based on typical damage values. When a fluence is found where instantaneous damage is observed, we perform a fine scan both in fluence (steps of $\approx 1 \text{ mJ}/\text{cm}^2$) and in the z -position of the sample in order to find the exact focus position for minimum damage fluence. The obtained minimum value is what we define as damage threshold fluence of a sample. After a spot was

damaged, we move the SESAM under test in the x - or y -direction in order to perform the next measurement on an undamaged spot. It is interesting to note that the higher the damage threshold, the bigger the impact trace on the SESAM when damaged; therefore, a larger translation to a new spot is required to perform the next measurement.

3.3.3 Damage threshold measurements

As a first step, we performed damage tests on the different 3-QW SESAMs described in Section 3.2 to compare the effect of the different topcoatings on the damage behavior. The damage fluences of these samples are presented in Figure 3.7 and Table 3.IV, together with the different parameters of the tested SESAMs.

Figure 3.7: Damage threshold of the different tested SESAMs together with their nonlinear reflectivity measurement.



	F_{sat} ($\mu\text{J}/\text{cm}^2$)	ΔR (%)	ΔR_{ns} (%)	F_2 (mJ/cm^2)	F_d (mJ/cm^2)	$S_d = F_d / F_{\text{sat}}$
NTC	72	2.05	<0.1	3200	32.6	450
SCTC	279	0.52	<0.1	5500	44.1	158
DTC2	168	0.71	<0.1	31700	122	726
DTC3	247	0.43	<0.1	346000	>210	>850

Table 3.IV: Damage thresholds of the different representative SESAMs together with their saturation parameters. The samples with a 3-pair dielectric topcoating did not show damage up to the maximum available fluence in our setup of $0.21 \text{ J}/\text{cm}^2$.

The topcoated SESAMs show, in all cases, higher damage fluences than without a topcoating. The damage fluences for the dielectric topcoated SESAMs (DTC2 and DTC3) are much higher than for the semiconductor topcoated SESAM (SCTC) with similar saturation parameters. It is interesting to note that regardless of the sample, instantaneous damage occurs at fluences deep in the rollover regime, where SESAM modelocked lasers would not operate in a stable regime (e.g., saturation parameters $S > 150$). However, the higher damage threshold is very beneficial to overcome the QML regime, where peak powers can be significantly larger. For our sample with three quarter-wave pairs dielectric topcoating (DTC3), we did not observe damage even at the maximum available fluence in our setup of 0.21 J/cm^2 . This corresponds to a peak intensity of 185 GW/cm^2 on the sample. This particular sample was tested at this maximum fluence level for several hours and no damage was observed.

3.3.4 Lifetime measurements

We measured lifetime curves of the samples for which the damage fluence could be measured with the available maximum fluence. The results are presented in Figure 3.8. For all samples, the lifetime curves seem to follow an exponential behavior.

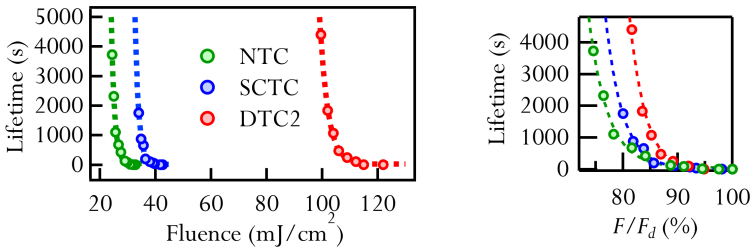


Figure 3.8: Lifetime curves of different representative SESAMs. Left: Lifetime curve with fluence axis in mJ/cm^2 , where one can see the large shift of the sample with a dielectric topcoating to higher fluences. Right: Same lifetime curves, but with the fluence axis normalized to the damage threshold of the sample.

	t_0 (s)	F_4 (mJ/cm ²)	F_3 (mJ/cm ²)	F_d (mJ/cm ²)	$S_d = F_d / F_{\text{sat}}$
NTC	48	1.15	14	32.6	450
SCTC	14	1.31	24	44.1	158
DTC2	24	2.97	74	122	726

Table 3.V: Fit parameters for the lifetime curves presented in Figure 3.8 using the fit function described in Formula (3.9).

The fit for the lifetime curves was performed using a single exponential function:

$$t(F) = t_0 + e^{\frac{(F-F_3)}{F_4}} \quad (3.9)$$

The fit parameters are presented in Table 3.V. The difference in the parameter F_3 is approximately the difference between the damage thresholds that was already described in the previous Paragraph. Parameter F_4 indicates the “slope” of the exponential function. The fit parameter t_0 is a small offset of the exponential in the y -axis necessary to correctly fit the measurements.

For every SESAM, the measurements were done for fluence levels ranging from the instantaneous damage fluence to around 80% of this value, leading to maximum time-to-damage values of 1–2 h. In Figure 3.8 (left), we can see that the lifetime of the sample with a dielectric topcoating is shifted to higher fluences (increase of F_3), confirming the advantage of this type of topcoating for increasing the damage threshold of SESAMs. In addition, the slope of the exponential (parameter F_4) is steeper for the topcoated samples, and in particular the dielectric topcoated one (see Figure 3.8 (right)), suggesting an even larger advantage (i.e., a larger difference between lifetimes) at lower fluences.

3.3.5 Extension of lifetime curves to lower fluences

We can use these measurements to estimate the lifetime of SESAMs at a given lower fluence. As we mentioned in the introduction Paragraph, SESAMs in high-power oscillators operate with saturation parameters $S \approx 20$ -100. It is therefore interesting to evaluate their lifetime at this level. The longest time-to-damage measurement was performed using a sample

with the same antiresonant structure as the one presented in Figure 3.3 (NTC) but with one QW instead of 3 QWs as an absorber. The lifetime of this sample is presented in a logarithmic scale as a function of the saturation parameter in Figure 3.9 and extended to very low saturation parameters.

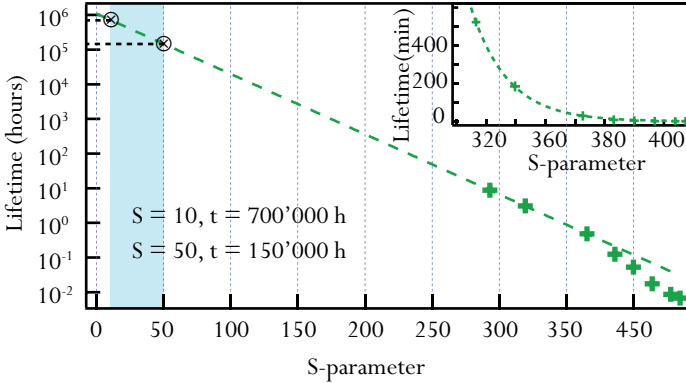


Figure 3.9: Lifetime of SESAMs extended to saturation parameters where typical high-power TDLs operate.

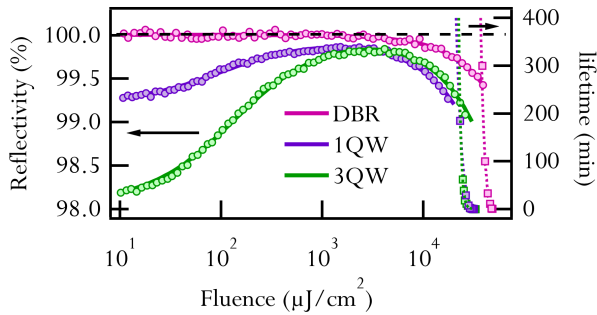
We can see that at saturation parameters of $10 < S < 50$, the suggested lifetimes are in the order of 700 000 – 150 000 h. Testing a sample with a dielectric topcoating such as the ones presented in the previous Paragraph (DTC2, for example) should result in even higher lifetimes at such low fluences. The value obtained is approximately an order of magnitude larger than observed in some high-power commercial systems using SESAM technology [59]. Nevertheless, considering that the longest time-to-damage point was taken at a fluence over an order of magnitude larger than the evaluated points, our measurements seem to give a good approximation of the lifetime of SESAMs at more standard fluences. However, we can see here that it is crucial to take points at long lifetimes ($> 10 \text{ h}$) for a correct extension of the lifetime curves. This was not performed because the TDL used for these experiments is not adequate for such long term testing, in particular in terms of long-term stability. Furthermore, it is likely that other mechanisms need to be taken into account for much lower fluences.

3.4 Damage mechanism

3.4.1 Influence of the absorber section on the lifetime

In order to identify the damage mechanism, we compared the damage behavior of a SESAM with a single QW absorber, one with 3-QWs (same one described in Section 3.2), and a DBR mirror (without absorber section) in order to evaluate if the damage thresholds are dependent on the absorber geometry. All the samples have no topcoating and in an antiresonant configuration. The results are presented in Figure 3.10 and Table 3.VI.

Figure 3.10: Nonlinear reflectivity and lifetime measurements for a DBR, a SESAM with 1QW as an absorber and a similar SESAM with 3 QW absorbers.



	F_{sat} ($\mu\text{J}/\text{cm}^2$)	F_2 (mJ/cm^2)	F_d (mJ/cm^2)	$S_d = F_d / F_{\text{sat}}$
DBR	-	7400	48	-
1QW	57	2600	32.1	560
3QW	72	3200	32.6	453

Table 3.VI: Nonlinear reflectivity fit parameters and damage thresholds of the samples with different absorber sections presented in Figure 3.10.

We can see that the damage behavior of a DBR is similar to that of the characterized SESAMs. Damage occurs deep in the rollover regime, and this rollover occurs at comparable fluence levels as for the SESAMs. This seems to indicate that this mechanism is related to the IA process, which is

mainly caused by the GaAs layers in the structure. We can also notice that the absorbers seem to have a tendency to slightly reduce the lifetime. One possible reason is that the SESAMs have additional GaAs spacers in the absorber section where the electric field is strong, and therefore represent an important contribution to the IA. This would also explain the 50% higher damage fluence for the DBR (Table 3.VI).

3.4.2 Approximate expression of the energy absorbed by IA

For all SESAMs under test, we observed that damage occurs at fluences deep in the rollover regime, suggesting a damage mechanism related to the absorbed energy due to IA. It is interesting to note that in the case of the sample with 3 QWs and a two-pair dielectric topcoating (DTC2) where F_2 is greatly increased; the damage curve is also shifted to higher values.

The energy absorbed by the sample due to the IA can be evaluated taking into account a number of approximations. For any given fluence, one can calculate the fraction of this fluence absorbed by the sample (Formula (3.6)). We approximate $R(F)$ using the expression for a flat-top beam (Formula (3.1)), this time including the extra rollover factor. This expression can be numerically corrected for a Gaussian beam. However, using the approximate expression for a flat-top beam leads to a negligible error in our calculation [57] and allows us to obtain an approximate analytical expression. We simplify Formula (3.1) by assuming a strongly saturated absorber ($F \gg F_{\text{sat}}$) and operation at a fluence close to the rollover point in reflectivity, which for weak TPA implies $F \ll F_2$. With these approximations, we obtain:

$$R(F) \approx R_{\text{ns}} \left(1 - \frac{F}{F_2} \right). \quad (3.10)$$

The absorbed energy F_{abs} per area can then be estimated by

$$F_{\text{abs}} \approx F \left(1 - R_{\text{ns}} \left(1 - \frac{F}{F_2} \right) \right). \quad (3.11)$$

For samples with small nonsaturable losses ($R_{\text{ns}} \approx 1$) such as the ones used for this damage study, we have

$$F_{\text{abs}} \approx \frac{F^2}{F_2}. \quad (3.12)$$

In order to verify that damage occurs at a constant level of deposited energy, we therefore need to verify

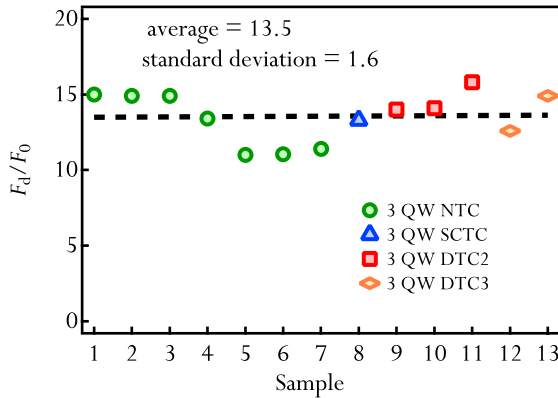
$$\frac{F_d^2}{F_2} = k \quad (3.13)$$

where k is a constant factor. Therefore, the damage fluence F_d for all SESAMs should scale proportionally to $\sqrt{F_2}$. In the case of SESAMs with the same absorber section, where the product $F_{\text{sat}} \cdot \Delta R$ is constant, the damage fluence F_d should scale proportionally with F_0 (Formula (3.2))

3.4.3 Experimental verification

In order to illustrate this dependence, we plotted the ratio F_d/F_0 for different SESAMs based on the 3-QW absorber described in the previous section (Figure 3.11) but with different topsections (and as a consequence a constant $F_{\text{sat}} \cdot \Delta R$ product).

Figure 3.11: Ratio F_d/F_0 for different samples for which we measured the damage threshold. All samples have the same absorber section (3 QWs) but different topcoating and/or different IA response.



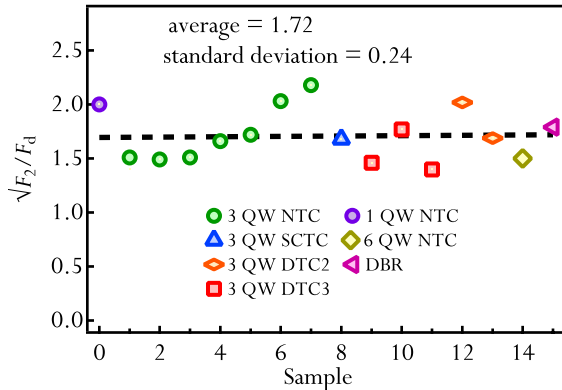
Even for the same topcoating design, we observe differences in the IA response of the samples due to the inhomogeneity of the MBE growth with respect to the center position of the wafer. This results in a difference in the damage threshold of the samples with the same structure. It is worth

noting that in the previous Paragraph where samples with different absorber sections are compared, we always used samples at the same position in the wafer to minimize this error. In total, we measured 13 samples with different IA.

These results clearly indicate that the ratio F_d/F_0 remains approximately constant for all the evaluated samples. This has an important consequence for the design of SESAMs with high damage threshold: by shifting the rollover to higher fluences, for example with a dielectric topcoating, it is possible to tailor the damage threshold of the structure.

If we want to extend this evaluation to samples with different absorbers, and even to a DBR mirror (since the absorber does not seem to be the cause for the damage mechanism), it is relevant to compare the damage threshold not to F_0 but to verify $F_d \propto \sqrt{F_2}$. In Figure 3.12, we plotted the ratio $\sqrt{F_2}/F_d$ for 16 different samples for which we were able to measure the damage fluence.

Figure 3.12: Ratio $\sqrt{F_2}/F_d$ for different samples for which we measured the damage threshold, including samples with different absorber sections and a DBR mirror.



The data seems to confirm that the damage process is dominated by the energy absorbed by the sample due to the IA mechanism, and that the main contribution to IA comes from the field in the DBR and spacer layers and not by the absorber section itself. This gives a clear indication of the damage behavior of such SESAMs, suggesting that catastrophic damage occurs due to heating of the lattice by energy absorbed by the IA process. It

also indicates a guideline on how to shift the damage fluence to higher values by simply increasing F_2 .

3.5 Guidelines for SESAMs with high damage thresholds

We identified two important parameters concerning catastrophic damage of SESAMs at high fluences: on the one hand, the damage mechanism originates in the amount of energy deposited by IA on the sample. The damage threshold scales, therefore, proportionally to $\sqrt{F_2}$ (Formula (3.13)). In our study, we used 1-ps pulses; therefore, the mechanism involved is mostly, but not only, due to TPA. Furthermore, we demonstrated that the absorber itself is not responsible for the damage mechanism, since a DBR showed a comparable damage threshold and lifetime behavior to those of the different SESAMs. Therefore, we can give guidelines to develop SESAMs for operation in high-power oscillators:

- Multiple QWs allow us to tune the modulation depth of the samples without changing their saturation fluence. This is required to have an initially large ΔR without topcoating, since the top mirror will reduce this modulation depth. When of a relatively low number of QWs is used, the absorbers can be placed simultaneously in one antinode of the electric field. In this case, the absorbers have only a small influence on the damage threshold, mostly because of the additional GaAs spacer layers commonly used as barrier material. When a larger number of QW is used, the amount of material to add becomes significant. In this case, one could also consider using another material with lower β_{TPA} (for instance AlAs) for such QW barrier layers. Without GaAs barrier layers, we expect uncoated SESAM samples to have an almost identical damage behavior to that of a DBR mirror. This point will be discussed in Part III of this Chapter.
- Dielectric topcoatings are preferred over semiconductor topcoatings to increase the saturation fluence. The topsection of a SESAM is critical because it experiences a very strong electric field and therefore contributes strongly to the IA and to the damage. With a

dielectric material, we achieve larger values for F_2 and, consequently, higher damage fluences.

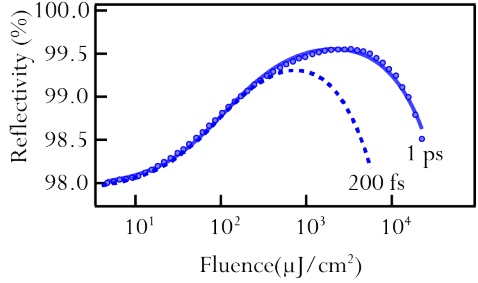
- The absorber section of the samples used for this study was grown at $T \approx 400^\circ\text{C}$ leading to recovery times in the order of ≈ 200 ps. In TDLs, SESAM recovery times are typically in the order of $\tau_{1/e} \approx 10$ -300 ps. Lower growth temperatures would not only result in shorter recovery times but also in a larger growth defect density. The exact influence of growth temperature on the damage behavior will be treated in the next Part.

Part II – Influence of absorber growth temperature on damage

In this section, we will focus on the specific challenges of designing SESAMs for high-power TDLs that target short pulse durations (typically sub-200fs). In the previous section, we saw that modelocked TDLs typically operate at large intracavity pulse energies, resulting in fluences on the SESAM in the order of several mJ/cm^2 (Table 3.I). These demanding conditions require robust SESAMs. In addition, specific SESAM parameters are required to generate short pulses from TDLs based on gain media with moderate gain bandwidths. The main challenges are in this case:

- As we discussed in Chapter 2 (Paragraph 2.3.1), the QML threshold can become more difficult to overcome in this type of lasers. Therefore, special attention needs to be paid in achieving SESAMs with high-damage thresholds.
- At short pulse durations (< 200 fs), IA can already occur at moderate pulse fluences. This is illustrated in Figure 3.13, where we present the nonlinear reflectivity measurement of an uncoated SESAM at 1 ps pulse duration (bullets), and estimated its response of at 200 fs (dashed line) by adapting the F_2 parameter using Formula (3.3). As we discussed in the first part of this Chapter, an early rollover can lead to multi-pulsing instabilities at moderate saturation parameters and can be one of the main limiting factors to reaching high power levels.
- SESAMs with short recovery times are important for the generation of short pulses using gain media with moderate gain bandwidths. A common way of tailoring the recovery time is to grow the QW absorbers at low-temperature (LT). LT-growth introduces additional defects in the lattice that result in fast nonradiative decay times [60-64]. However, this results in extra nonsaturable losses, which can lead to thermal effects [39, 63].

Figure 3.13: Nonlinear reflectivity measurement of an uncoated SESAM at 1 ps pulse duration (bullets), and estimated response of at 200 fs (dashed line) by adapting the F_2 parameter using Formula (3.3) (dashed line).



Therefore, special care needs to be taken to design SESAMs that combine large modulation depths, large saturation fluences, fast recovery times, reduced IA and high damage thresholds. In Part I of this Chapter, we showed that it is possible to tailor the IA and damage threshold by using appropriate dielectric topcoatings on antiresonant structures with multiple QWs as absorbers, and that the absorber section does not have a strong influence on the damage mechanism. However, in this study, we used a set of samples with intermediate recovery times and small modulation depths leading to negligible nonsaturable losses. Here, we extend this study and investigate the influence of lower growth temperatures (which result in faster recombination times), on the damage threshold of SESAMs with high modulation depths, designed for power scaling of TDLs with sub-200 fs.

3.1 Experimental setup and SESAM structures

3.1.1 Experimental setup

In order to carry out this study, we measured the nonlinear reflectivity, damage threshold and recovery parameters of a set of representative samples. For the nonlinear reflectivity and the damage threshold measurements, we used the same setup and experimental procedure described in Part I of this Chapter. To measure the recovery time of the samples, we used a standard pump-probe setup (Figure 3.14) seeded by a bulk Yb:YAG laser delivering 1-ps long pulses at a repetition rate of 38 MHz and 150 mW of average power. The laser operates at a central wavelength of 1030 nm.

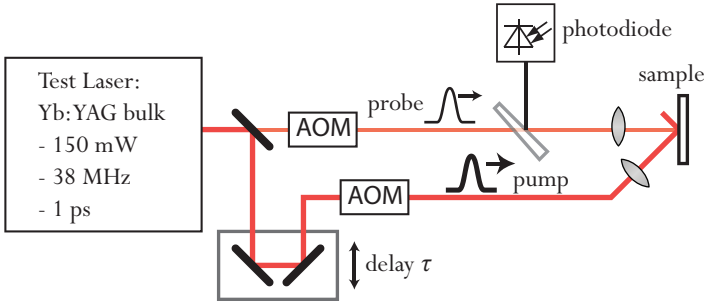


Figure 3.14: Pump-probe setup used for measuring the recovery dynamics of the different SESAMs. AOM: Acousto-optic modulator.

The temporal decay of the reflectivity $R(t)$ of the SESAM from a certain saturation level back to the unsaturated reflectivity can be described by a bi-temporal exponential function of the delay between the probe and the pump pulse:

$$R(\tau) = Ae^{-\frac{\tau}{\tau_{\text{fast}}}} + (1-A)e^{-\frac{\tau}{\tau_{\text{slow}}}} \quad (3.14)$$

where A is the amplitude of the fast component with a characteristic decay time at $1/e$ of τ_{fast} and $(1-A)$ is the amplitude of the slow component with a $1/e$ decay time τ_{slow} . This bi-temporal response is due to different recombination processes. The fast response is usually on a timescale of some hundred femtoseconds and is due to the fast intraband thermalization of carriers to the lowest energy state in the conductive energy band. The second slower time response (in the order of picoseconds to nanoseconds) corresponds to carrier recombination with holes from the valence band [63]. It is worth noting that in our setup the 1-ps long probe pulses usually do not properly resolve the fast recombination exponential component. In order to precisely evaluate it, another laser system with shorter pulses is required. Nevertheless, we can compare the behavior of the response time of different SESAMs knowing this uncertainty.

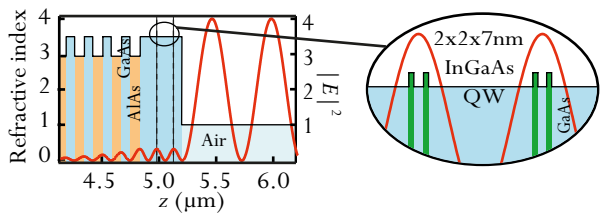
Different growth temperatures influence both characteristic decay times as well as their respective amplitude. However, it is difficult to tailor these parameters independently with LT-grown QWs. This is due to the nature of the low growth temperature process, which consists of

introducing defects in the lattice structure to reduce the carrier recombination time. A strict comparison of the recovery of different samples requires comparing all three parameters τ_{slow} , τ_{fast} and A . A commonly used simplification consists of comparing the recovery time at a given level of recovery, for example, the time that it takes for the absorber to recover to $1/e$ of its saturated value. Another point to take into account is that the recovery dynamics depend on the level of saturation of the absorber. In this study, we compare all samples at similar saturation level of $S \approx 3$, limited by the output power of our test laser.

3.1.2 Structure used for this study

For this study, we used a structure with a large numbers of QWs, to reach an initially large modulation depth. The structure of the uncoated sample is presented in Figure 3.15. It consists of a standard DBR and four InGaAs QW absorbers embedded in GaAs. The absorbers were placed two-by-two in two consecutive antinodes of the electric field pattern to optimize their absorption. This resulted in samples with $>3\%$ modulation depth, which can be further coated to decrease their modulation depth. The QW absorbers of the four samples used for this study were grown at different temperatures (245°C , 270°C , 300°C , 385°C). The samples were designed for an operation wavelength of 1030 nm .

Figure 3.15: Structure of the uncoated SESAMs used for this study. The QWs were grown at different temperatures and the samples were evaluated for damage threshold.



3.2 Experimental results

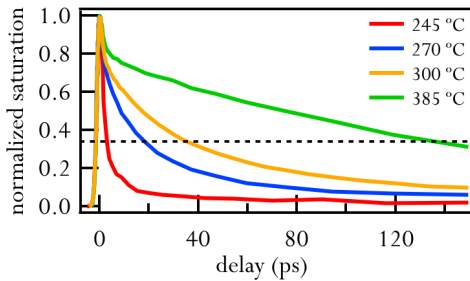
3.2.1 Influence of growth temperature on recovery parameters and damage threshold

All investigated SESAMs had the same structure, and yielded similar saturation parameters (Table 3.VII). The differences observed are most likely due to small errors during the MBE growth, that result in slight differences in the enhancement in the structure.

$T_{\text{growth}} (^{\circ}\text{C})$	245	270	300	385
τ_{fast} (ps)	2	8	7	2
τ_{slow} (ps)	66	88	107	167
A	0.77	0.67	0.46	0.2
$\tau_{1/c}$ (ps)	3	17	33	128
F_{sat} ($\mu\text{J}/\text{cm}^2$)	32	31	22	34
ΔR (%)	3.9	3.6	4.4	3.6
ΔR_{ns} (%)	1.2	0.4	0.2	0.1
F_2 (mJ/cm^2)	1460	1430	1230	1602
F_d (mJ/cm^2)	15.6	18.4	22.6	25.1

Table 3.VII: Recovery parameters of SESAMs with the same structure (Figure 3.15), but with the absorbers grown at different temperatures. The recovery parameters were extracted from the measurements presented in Figure 3.16.

Figure 3.16: Pump-probe measurements of samples with the same structure, but the absorbers grown at different temperatures.



In Figure 3.16, we plotted the pump-probe traces of these samples. The corresponding fit parameters are presented in Table 3.VII. These measurements indicate that samples grown at lower temperatures have faster recovery times, as expected from previous studies [39].

In Figure 3.17 (left), we plotted the different characteristic decay times as a function of the growth temperature. The amplitude of the fast component A decreases with the growth temperature, whereas the slow time decay constant τ_{slow} increases with growth temperature. Both quantities behave linearly with the growth temperature. The fast decay time τ_{fast} is difficult to evaluate correctly with the long pulse duration of our seed laser.

In Figure 3.17 (right), we plot the decay time to 1/e ($\tau_{1/e}$) as a function of QW growth temperature. The observed exponential behavior confirms previous studies carried out with LT-grown GaAs [39]. Although the parameter $\tau_{1/e}$ is not sufficient to fully characterize the dynamics of the absorber, it is appropriate to compare the recovery of the absorber in a passively modelocked laser. In fact, in most soliton formulas the recovery parameter of the absorber corresponds to the time where the gain net window after the pulse closes. In this picture, a constant degree of recovery is related to the level of losses in one round trip of the laser cavity.

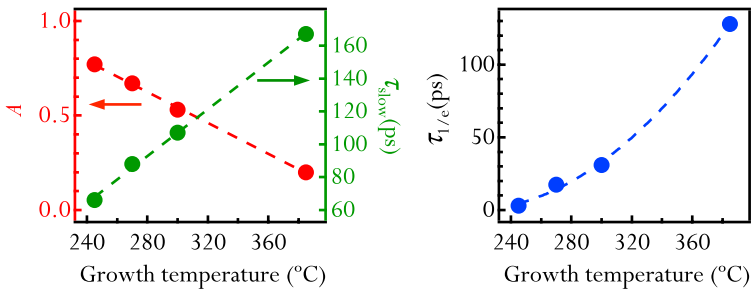


Figure 3.17: Different recovery parameters of the studied samples versus absorber growth temperature. Left: decay time of the slow component and amplitude versus absorber growth temperature. Right: decay time at 1/e versus growth temperature.

In Figure 3.18 (left), we plot nonsaturable losses and damage threshold of these samples as a function of the growth temperature. The total nonsaturable losses of the samples decrease exponentially with the growth temperature, which also confirms the observations made in reference [39]. It is interesting to point out that even for our fastest sample with a recovery time of ≈ 2 ps the nonsaturable losses stay reasonable in comparison to the modulation depth of the sample (1.2% nonsaturable losses for 3.9% modulation depth). For use in most common TDLs, lower modulation depth is required. Therefore a dielectric topcoating that will reduce the field in the absorber will be applied, further reducing the nonsaturable losses.

In Figure 3.18 (right), we can see that the damage threshold decreases exponentially with the nonsaturable losses of the samples. However, the change in damage threshold is relatively small compared to the increase in the recovery time of the absorber (we observe a decrease of 40% in damage threshold, for a 12-fold decrease of the nonsaturable losses). Heating of the absorbers due to the additional defects most likely causes this small decrease in the damage threshold of the samples.

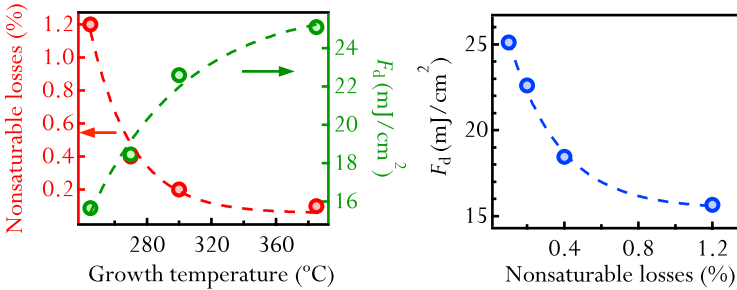


Figure 3.18: Left: Dependence of damage threshold and nonsaturable losses on absorber growth temperature. Right: Dependence of damage threshold on nonsaturable losses.

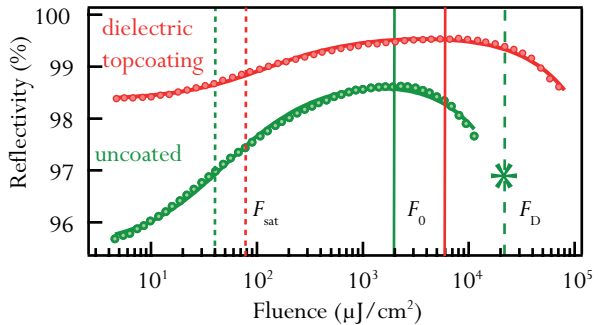
In the study presented in the previous section, we only considered samples with negligible nonsaturable losses. In that case, the absorbers had nearly no influence on the damage mechanism, which mainly originated from IA. The results presented here indicate that the nonsaturable losses introduced by the additional defects in the absorbers also contribute to the

damage mechanism (Figure 3.18b). However, this influence is small relative to the change in the recovery time of the samples. Furthermore, even for our fastest samples, damage occurs at fluence levels where modelocked lasers do not operate in a stable configuration.

3.2.2 Topcoated sample for use in high-power thin-disk laser

For further use of the different SESAMs presented in this part in a high-power TDL based on Yb:LuScO (Chapter 4, Paragraph 4.3.2), we applied a two-pair $\text{SiO}_2/\text{Si}_3\text{N}_4$ dielectric topcoating using PECVD in order to reduce the field in the absorbers. As discussed in the first section of this chapter, this results in an increase of the saturation fluence and reduction of the modulation depth. Furthermore, this increases their damage threshold, and IA coefficient. Since this SESAM was designed in the goal of obtaining short pulse durations (<200 fs), we used the sample with the shortest recovery time, which was grown at 245°C . The recovery time of the topcoated sample is the same as the sample without topcoating. The deposition of this topcoating by PECVD was done at 300°C , which is low enough not to generate any post-growth annealing effects on the absorber of the SESAM. The effect of the topcoating on the nonlinear reflectivity of the initial sample is presented in Figure 3.19.

Figure 3.19: Nonlinear reflectivity measurement of uncoated sample grown at 245°C (green) and after dielectric topcoating (red).



The saturation fluence F_{sat} , IA coefficient F_2 and damage threshold F_d are increased, which is important for high-power operation, the initially large modulation depth ΔR is decreased to a moderate value and the recovery time remains the same (Table 3.VIII). The damage threshold of

the topcoated sample was not measured in order to avoid introducing damage spots to the sample, but the measurement range indicates that the damage fluence is significantly increased. The obtained parameters are ideally suited for the targeted parameters.

	Before Topcoating	Dielectric Topcoating
Structure	4 QWs	4 QWs + 2-pair SiO ₂ /Si ₃ N ₄
F_{sat} ($\mu\text{J}/\text{cm}^2$)	32	70
ΔR (%)	3.9	1.3
ΔR_{ns} (%)	1.2	0.4
F_2 (mJ/cm^2)	1460	7300
$\tau_{1/e}$ (ps)	3	3
F_d (mJ/cm^2)	16	> 80

Table 3.VIII: SESAM parameters and damage threshold of sample with the lowest recovery time before and after applying dielectric topcoating.

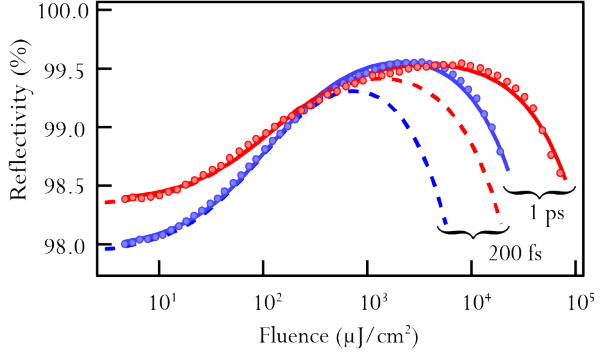
3.2.3 Comparison with previous uncoated SESAM with similar parameters

In Figure 3.20, we compare the nonlinear reflectivity of the newly designed SESAM (red) with an uncoated SESAM with similar saturation parameters (blue). In both cases, we added in dashed lines the expected response of the SESAM at shorter pulse duration (200 fs) by modifying F_2 according to Formula (3.3). The extracted fit parameters of the nonlinear reflectivity, recovery parameters and damage threshold of both samples are presented in Table 3.IX.

Using the SESAM shown in blue, pulses as short as 195 fs were demonstrated at a moderate average power of 9.5 W using Yb:LuScO as the gain medium. In this experiment, the SESAM operated at a fluence of $1 \text{ mJ}/\text{cm}^2$. The early rollover in the reflectivity of this SESAM was one of the limitations to higher average power. Furthermore, the low damage threshold of this sample resulted in repeated damage of the sample during the QML regime. The new sample has similar saturation and recovery parameters but a higher damage threshold. In addition, its rollover is shifted to higher fluences. This allowed us to reach 23 W and 235 fs [65]. In this case, the fluence on the SESAM was $1.4 \text{ mJ}/\text{cm}^2$. In this

experiment, no damage was observed and further scaling was prevented by damage of the disk. This laser experiment will be described in more detail in Chapter 4.

Figure 3.20: Nonlinear reflectivity of two samples with similar saturation parameters, one uncoated and based on a single QW as an absorber (blue) and one designed with 4 QWs and a dielectric topcoating, following our guidelines (red).



	Old sample	New sample
Structure	1 QW	4 QW + 2-pair SiO ₂ /Si ₃ N ₄
F_{sat} ($\mu\text{J}/\text{cm}^2$)	64	70
ΔR (%)	1.9	1.3
ΔR_{ns} (%)	0.3	0.4
F_2 (mJ/cm^2)	1950	7300
$\tau_{1/e}$ (ps)	5.1	3
F_d (mJ/cm^2)	26	> 80

Table 3.IX: Nonlinear reflectivity, recovery time and damage threshold of two samples with similar saturation parameters. One sample is uncoated and based on a single-QW absorber and the second was fabricated following our guidelines, based on 4-QW absorbers and a dielectric topcoating.

This result indicates that the guidelines developed in Part I can be extended to samples with fast recovery times and larger modulation depths, suitable for modelocking of high-power TDLs with short pulse durations.

3.3 Additional guidelines: SESAMs with fast recovery times

The additional measurements presented here clearly show that growing the absorber section at lower temperatures results in samples with faster recovery times but also higher nonsaturable losses, confirming previous

studies [39]. Our damage measurements indicate that the additional nonsaturable losses represent an extra contribution to the damage threshold. However, this contribution is small compared to the mechanism described in the first section. In fact, we observe a decrease of nearly two orders of magnitude in the recovery time at $1/e$ of our samples with growth temperature, while the damage threshold is only decreased by 40%. Even for the fastest samples, damage occurs at fluences where modelocked lasers would not operate in a stable regime. Adding a dielectric topcoating increases the damage threshold while maintaining the fast recovery time.

An additional point can be added to the guidelines presented in the first Part of this Chapter to obtain high damage threshold samples. For laser systems aiming for short pulse durations, where short recovery times and large modulation depths are beneficial, a compromise needs to be found in terms of nonsaturable losses, damage threshold and recovery time of the samples. If a sufficiently large number of QWs is initially used and a suitable dielectric topcoating is applied, the resulting samples combine high damage thresholds and fast recovery times (identical to that of the uncoated samples). Furthermore, the topcoating reduces the nonsaturable losses of the sample, which is important to avoid heating and thermal lensing.

Part III - Summary and outlook

3.1 Summary and guidelines for SESAMs with high damage thresholds

To the best of our knowledge, this is the first detailed study on damage of SESAMs designed for high intracavity energy oscillators. We identified the relevant nonlinear parameters to compare SESAM damage independently of their specific design structure. We clearly observe a dependence of the damage threshold on the IA parameter F_2 , by demonstrating that the damage fluence F_d of all the tested SESAMs scales proportionally to $\sqrt[3]{F_2}$. At the targeted pulse durations for modelocked TDLs (typically < 1 ps), the mechanism responsible for this rollover in reflectivity is mainly TPA. Therefore, the main contribution to the damage process comes from the GaAs layers in the SESAM structure, which have the largest TPA coefficient, and not from the absorber layers. In the case of SESAMs with the same absorber (i.e., constant $F_{\text{sat}} \cdot \Delta R$), the damage fluence F_d scales proportionally to the rollover fluence F_0 (Formula (3.2)). In summary, damage occurs due to heating of the lattice by energy absorbed because of IA and not by heat generated in the absorber. Additional damage measurements on a simple semiconductor DBR mirror further confirm this conclusion. We give clear design guidelines for SESAMs with reduced IA and therefore increased damage thresholds. Among the SESAMs used for this study, we demonstrated samples with high saturation fluences of $> 200 \mu\text{J}/\text{cm}^2$, low nonsaturable losses of $< 0.1\%$, reduced IA, and increased damage threshold. This was achieved by using a dielectric topcoating on a multiple-QW SESAM. For our best sample with a saturation fluence of $247 \mu\text{J}/\text{cm}^2$, nonsaturable losses of $\Delta R_{\text{ns}} < 0.1\%$, and a modulation depth of $\Delta R = 0.43\%$, we could not observe damage even at fluences as high as $0.21 \text{ J}/\text{cm}^2$ which was the maximum available fluence in our setup. This corresponds to a peak intensity of $185 \text{ GW}/\text{cm}^2$. For all SESAMs tested, the damage threshold occurs at fluences where it is not possible to operate a modelocked laser in stable operation.

Time-to-damage measurements were performed and lifetime curves of > 8 h were measured for some SESAMs, confirming a clear exponential behavior and suggesting lifetimes of several years at standard operation fluences. However, at much lower fluences than the instantaneous damage fluence, other damage effects might have to be considered. Nevertheless, these extrapolated lifetimes are only one order of magnitude higher than those observed in some high-power commercial systems using SESAM technology.

In the case where short recovery times are of importance, we demonstrate that the extra nonsaturable losses introduced by LT-growth of the absorbers have only very small influence on the damage threshold of the samples. Therefore, the guidelines to obtain high damage threshold SESAMs with reduced IA also apply for samples with very fast recovery times.

Future damage investigations will explore different laser operation regimes such as pulse duration, pulse repetition rate and spot size on the SESAM. Another interesting investigation would consist of performing a similar study to determine the damage mechanisms involved in quantum-dots, carbon nanotube-based and graphene-based saturable absorbers [48, 66, 67]. These novel absorbers have gained significant attention during the past years as modelocking devices. Therefore, identifying and comparing their damage behavior to the well-established SESAM technology is of interest.

It is particularly important to reproduce a similar study at shorter pulse duration such as 100 fs, to confirm our measurements in a regime where TPA is clearly dominant. However, with the current guidelines, it is already possible to estimate the damage threshold at shorter pulse durations, even though these values still need to be experimentally confirmed.

3.2 Outlook: future SESAM designs

3.2.1 More QWs, more topcoating layers

The simple guidelines derived in this Chapter indicate that multiplying the number of QWs and the number of dielectric layers results in high-damage

threshold samples with reduced IA and high saturation fluences - all crucial parameters for high-power oscillators. However, the limits of this approach were not investigated, for example, in terms of maximum amount of QWs and/or dielectric top layers.

- Dielectric topcoating:

Concerning the dielectric topsection, we chose the pair $\text{SiO}_2/\text{Si}_3\text{N}_4$ simply because the coatings could be applied in-house in just a few hours using PECVD. Most of the depositions were performed at 300°C in order to achieve high optical quality layers. However, this deposition method has limits in terms of the number of layers that can be applied.

- Stress: Given the high growth temperature, a large number of layers can result in significant stress of the coating at room temperature, which can lead to fracture of the coating. The limit in terms of number of layers can be increased up to some extent by reducing the deposition temperature, for example to 120°C , at the expense of a slight degradation of the optical quality of the deposited coating. However, for a large number of layers, the use of other stress-less deposition techniques such as sputtering or evaporation should be considered.
- Materials: Different dielectric material pairs with a higher refractive index contrast is beneficial to reduce the necessary number of layers to achieve a given field enhancement in the absorbers. Some examples are $\text{SiO}_2/\text{Ta}_2\text{O}_5$ (which is already commonly used as a topsection for SESAMs) $\text{SiO}_2/\text{HfO}_2$ or $\text{SiO}_2/\text{TiO}_2$.

- Number of QWs:

Concerning the number of QWs that can be applied, a certain number of points need to be taken into account:

- Ideally using the maximum possible number of QWs in one antinode of the electric field is preferred to limit the amount of material used in the structure. However, the QWs need to be separated by a large enough distance that they do not interact between each other. This sets a limit to the number of QWs in one antinode for achieving

efficient absorption. We limit this number to three QWs per antinode.

- The fabrication of SESAMs with large amount of QWs is challenging due to stress resulting from the difference in lattice constants of the absorbers and the spacer layers. Although the exact consequences of this stress on SESAM properties has not been studied in detail, strain-compensation methods might be necessary to maintain the losses in the sample low.

3.2.2 QW absorbers embedded in AlAs

The layers in which the QWs are embedded experience a strong electric field and therefore have an important contribution to the TPA response of the sample. Therefore, the use of a material with a low TPA-coefficient for these layers is beneficial to achieve samples with higher damage threshold and reduced TPA response. An improvement to the structures presented in this Chapter consists of embedding the QW absorbers in AlAs and not in GaAs. AlAs has an indirect bandgap that has a higher energy difference than GaAs (2.16 eV for AlAs versus 1.42 eV for GaAs [68]) and therefore exhibits a significantly lower TPA coefficient [58]. These samples are expected to have similar TPA response than a DBR. For a low number of QWs, the improvement in terms of TPA is negligible. However, this is expected to be an essential step for future samples with a larger number of QWs.

In addition to the lower TPA response of the samples, embedding LT-grown InGaAs QWs in AlAs results in samples with exceptionally fast recovery times, and similar nonsaturable losses as comparable structures embedded in GaAs. The exact reasons for this are currently being investigated. However, these fast samples have been crucial in modelocking of several lasers with record-short pulse durations [14, 40, 69], including the results presented in Chapter 4.

Special care needs to be taken with these samples because AlAs is strongly oxidized when exposed to air. Although the top layer material of SESAM samples is always GaAs, degradation can occur from the sides, for

examples on cleaved samples. The dielectric topsection suggested in this Chapter is an efficient way to protect samples.

3.2.3 Novel mirror structures

The next step to improve the TPA response and damage of samples is modifying the standard AIAs/GaAs DBR. As we saw in the first part of this Chapter, the field in this part of the structure is mostly responsible for the TPA response of the sample.

- One possibility is to replace GaAs by $\text{Al}_x\text{Ga}_{1-x}\text{As}$ (with for example $x = 0.2$) and increase the number of pairs accordingly to the loss in refractive index contrast.
- Another possibility is to design structures with low amount of GaAs (or even low amount of AlGaAs) that deviate from an ideal Bragg reflector in that the layers are no longer quarter-wave pairs. In this case, sufficiently high reflectivity can be achieved, usually at the expense of bandwidth.

3.2.4 Upside-down growth of large-scale SESAMs for improved thermal management

Up-to-date, thermal effects in SESAMs were not the main limitation for power scaling of modelocked TDLs. Deposited heat in such structures is very low and is mainly due to the nonsaturable losses of the samples. However, in future kW level oscillators, this small fraction of absorbed power can easily become significant.

The modelocked TDL power-scaling concept relies on increasing the spot sizes both on the disk and on the SESAM. Although for SESAMs we have the additional design freedom of increasing the saturation fluence to keep the saturation level constant, spot sizes will most likely also become larger as we move towards kW output powers. One important consequence is that possible thermal lensing of the SESAM will then become a critical issue. Therefore, the design of large (several cm) SESAMs with improved thermal capabilities is a key point in this direction.

One possible improvement for better thermal management of SESAMs is substrate removal. In standard SESAMs, the DBR and the absorber section are grown in this order on a GaAs substrate. In this case,

the GaAs substrate plays no optical role, and is just limiting heat transport due to its low thermal conductivity compared for example to diamond ($\kappa_{\text{GaAs}} \approx 44 \text{ Wm}^{-1}\text{K}^{-1}$ and $\kappa_{\text{diamond}} \approx 2200 \text{ Wm}^{-1}\text{K}^{-1}$). A common approach to improve the heat removal of the sample is to grow the structure upside down, contact the sample to a heatsink and then remove the substrate. This technique is commonly referred to as “flip-chip” bonding, and is most commonly used for power scaling of VECSELs [70], where the very high pump absorption make this a more critical issue. In this way, heatsinks with better heat removal properties such as copper or diamond can be chosen. The resulting structure is very thin (typically some μm thick) and can be very efficiently cooled. This technique is illustrated in Figure 3.21.

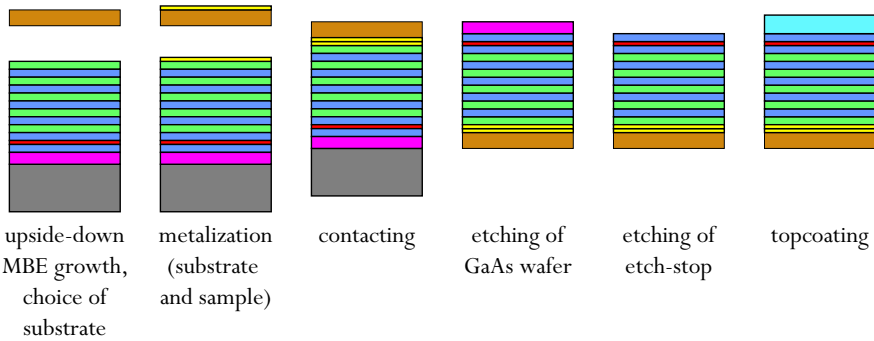


Figure 3.21: Schematic for the fabrication steps of future generation upside-down SESAMs.

During the timeframe of this thesis, the first test samples were designed using a copper heatsink. Several points still appear challenging and are currently being investigated:

- obtaining uniform etching of the etch-stop layer in large samples, to obtain a surface with sufficient quality
- bonding of the samples without pre-stress

Using large-scale upside down SESAMs will then be key to limit thermal distortions of the SESAM and achieve stable modelocking in future kW-level modelocked TDLs.

Chapter 4 - New pulse duration limits of modelocked thin-disk lasers

High peak power MHz sources with short pulse durations (< 200 fs) currently rely on external pulse compression schemes such as passive spectral broadening using self-phase modulation (SPM) without any additional gain [71], active spectral broadening in fiber amplifiers [72, 73], compression in gas-filled hollow core fibers and capillaries [74, 75], and parametric amplification techniques [76]. Although these systems reach impressive performance, they usually suffer from a reduced temporal quality of the pulses and a rather high complexity. In contrast, SESAM modelocked TDLs operate in the soliton modelocked regime [34, 36], and therefore deliver transform-limited sech^2 -shaped pulses directly from a laser system with a footprint similar to that of a low-power oscillator. Therefore, achieving shorter pulses directly from these high-power sources is currently a topic of important research efforts.

One of the most challenging points is finding broadband materials suitable for high-power operation in the thin-disk geometry and short pulse generation. Usually, Yb-doped broadband materials exhibit a disordered lattice structure that in turn limits its thermal properties. Nevertheless, the thin-disk geometry with its excellent heat removal capabilities is potentially suitable to overcome these limitations, and extend high-power operation to the sub-100-fs regime.

The specific difficulties in terms of SESAM design are another major point. In Chapter 3, Part II we presented recent work on specific SESAM designs suitable for such laser sources.

In this Chapter, we explore the pulse duration limits of modelocked TDLs based on different promising gain materials. In all cases, optimized SESAM designs were key to achieve these results. This Chapter is organized as follows. In the first Paragraph, we will briefly summarize the state-of-the-art of novel gain materials for TDLs. In the following Paragraphs, we will focus on experimental results obtained with three different sesquioxide

materials: Yb:LuO, Yb:LuScO, and Yb:ScYLO (Yb:(Sc,Y,Lu)₂O₃). In all cases, we were able to modelock an important fraction of the available emission bandwidth, reaching record-short pulse durations. In particular, a modelocked TDL with sub-100-fs pulse duration based on the mixed sesquioxide material Yb:LuScO was demonstrated. These are the shortest pulses ever demonstrated from a TDL to date, reaching for the first time the sub-100 fs milestone. This proof-of-principle experiment shows that such oscillators are suitable to access this regime. Furthermore, we will present preliminary power scaling experiments that indicate that much higher powers should be within reach. We will conclude with an outlook towards these higher power levels with sub-100 fs pulse durations.

4.1 Broadband materials for high-power thin-disk lasers

4.1.1 State-of-the art

Many Yb-doped gain materials were modelocked in the thin-disk geometry in the past years. In the goal of achieving the shortest possible pulse duration out of such systems, an important challenge is to find gain materials that combine the required thermo-mechanical properties with a broad emission bandwidth to support ultrashort pulse durations. As we highlighted in Chapter 2, most Yb-doped broadband materials exhibit a disordered lattice structure that in turn limits their thermal properties. In particular, it is challenging to maintain a high thermal conductivity at the required doping levels for efficient thin-disk operation. This is clearly illustrated in Figure 4.1 (left), where we plot thermal conductivity of materials that have been modelocked in the thin-disk geometry versus their emission bandwidth. The thermal conductivity of these materials was plotted at an equivalent typical doping concentration $N \approx 0.85 \cdot 10^{21} \text{ cm}^{-3}$ (as a reference, this corresponds to a typical doping concentration of 3 at.% for Yb:LuO). In Figure 4.1 (right), we plotted the average power of modelocked TDLs demonstrated to date as a function of their pulse duration. The “empty area” in this Figure clearly illustrates the challenge of obtaining short pulses and high average powers.

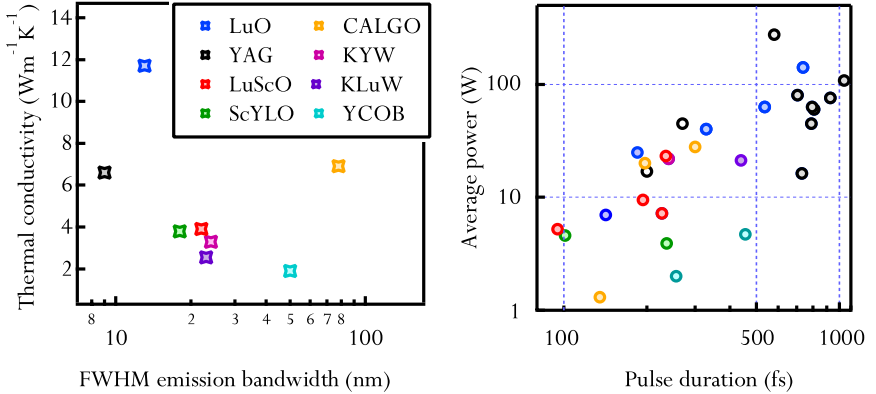


Figure 4.1: Left: Thermal conductivity versus emission bandwidth of most commonly used gain materials in modelocked TDLs. An overview with more details on the material parameters is given in [77]. Right: Average power of modelocked TDLs versus their pulse duration, illustrating the difficulty of combining high average power and short pulses. The laser parameters of the different results illustrated in this Figure are presented in Table 4.I.

Table 4.I summarizes laser results achieved to date from SESAM modelocked TDLs. A more general overview of different thin-disk materials also in terms of their continuous-wave (cw) performance but with a particular focus on the minimum achievable pulse duration is given in reference [78].

The most widely-used gain material for TDLs is Yb:YAG [79]. It is grown with excellent quality and in large sizes. Furthermore, it shows a good thermal conductivity (typically around 7 W/(m·K) for an Yb³⁺ doping concentration of 10 at.%), which is another key ingredient for laser operation at high power levels. Little surprising, the first modelocked TDL was based on Yb:YAG. It was presented in the year 2000 and delivered an average power of 16.2 W with a pulse duration of 730 fs [20]. Four years later the average power could be increased by almost a factor of five to 80 W with a very similar pulse duration of 705 fs [80]. To date, the typical pulse duration of high-power SESAM modelocked Yb:YAG TDLs is limited to > 500 fs, even though low power SESAM modelocked laser oscillators demonstrate much shorter pulses [81, 82].

New pulse duration limits of modelocked thin-disk lasers

Material	P_{av}	E_p	τ_p	f_{rep}	P_{pk}	Ref.
Yb:YAG	275 W	17 μ J	580 fs	16.3MHz	26 MW	[14]
	145 W	41.3 μJ	1.1 ps	3.5 MHz	35 MW	[21]
	80 W	1.5 μ J	705 fs	57 MHz	1.7 MW	[80]
	76 W	26 μ J	960 fs	2.9 MHz	25 MW	[45]
	45 W	11 μ J	791 fs	4 MHz	12.5 MW	[45]
	63 W	5.1 μ J	796 fs	12 MHz	5.7 MW	[42]
	60 W	1.7 μ J	810 fs	34 MHz	1.9 MW	[53]
	16 W	0.5 μ J	730 fs	34 MHz	0.6 MW	[20]
Yb:YAG (KLM)	17 W	0.4 μ J	200 fs	40 MHz	1.9 MW	[83]
	45 W	1.1 μ J	270 fs	40 MHz	3.7 MW	[83]
Yb:LuO	141 W	2.3 μ J	738 fs	60 MHz	2.8 MW	[30]
	63 W	0.8 μ J	535 fs	81 MHz	1.3 MW	[84]
	40 W	0.5 μ J	329 fs	81 MHz	1.3 MW	[84]
	7 W	0.1 μ J	142 fs	64 MHz	0.7 MW	[85]
	25 W	0.4 μ J	185 fs	66 MHz	1.8 MW	[86]
Yb:KLuW	21 W	0.6 μ J	440 fs	35 MHz	1.2 MW	[87]
Yb:KYW	22 W	0.9 μ J	240 fs	25 MHz	3.3 MW	[88]
Yb:ScYLO	3.9 W	0.1 μ J	236 fs	36 MHz	0.4 MW	[89]
	5 W	0.1 μ J	101 fs	70 MHz	0.6 MW	x
Yb:CALGO	28 W	1.3 μ J	300 fs	21 MHz	3.8 MW	[90]
	20 W	0.9 μ J	197 fs	21 MHz	4 MW	[90]
	1.3 W	0.03 μ J	135 fs	45 MHz	0.2 MW	[90]
Yb:YCOB	2 W	0.1 μ J	270 fs	20 MHz	0.3 MW	[91]
	4.7 W	0.2 μ J	455 fs	24 MHz	0.4 MW	[91]
Yb:LuScO	7 W	0.1 μ J	227 fs	66 MHz	0.4 MW	[92]
	23 W	0.3 μ J	235 fs	70 MHz	1.2 MW	[65]
	9.5 W	0.1 μ J	195 fs	70 MHz	0.6 MW	[65]
	5 W	0.1 μ J	96 fs	77 MHz	0.6 MW	[40]

x: indicates results that have not been published to-date

Table 4.I: Parameter overview of modelocked TDLs demonstrated to date. The extreme values are shown in red (highest average power, pulse energy, shortest pulse duration).

Very recently, the first Kerr-lens modelocked (KLM) Yb:YAG TDL was demonstrated with an average power of 17 W and a pulse duration of 200 fs [93], indicating that much shorter pulses can be achieved at higher power levels using SESAM modelocking.

One broadband material that held the record for the shortest pulses for many years is Yb:KYW [94, 95]. In 2002, a modelocked TDL based on this material was presented with an average power of 22 W and a pulse duration of 240 fs [88]. The varying quality of the available material and the anisotropic nature of this crystal, however, limited further power scaling.

Besides the tungstate materials, some borate materials show wide gain spectra for the generation of short pulses [96, 97]. Some initial modelocking experiments with Yb:YCOB revealed a pulse duration of 270 fs at a moderate average output power of 2 W. Similar to Yb:KYW anisotropic thermal aberrations complicated fundamental mode operation at higher power levels [91].

Very recently, the first modelocking experiments using the promising material Yb:CALGO were reported [90]. This material combines a very broad and smooth emission bandwidth with a thermal conductivity comparable to Yb:YAG. In the first modelocking results up to 28 W of average power were demonstrated with 300 fs pulses. Shorter pulses (135 fs) could only be achieved at a moderate average power of 1.3 W. The available doping concentrations and thickness of the crystal limits the average power in this first experiment. Nevertheless, this material is one of the most interesting candidates for power scaling of modelocked TDLs with short pulses, in particular give the very promising results obtained with bulk modelocked lasers based on this material [98, 99].

Finally, another very successful group of thin-disk gain materials are Yb-doped cubic sesquioxides. All experimental results presented in this Chapter are based on this family of materials. In the next Paragraph, we will cover the properties of these materials in more detail.

4.1.2 Sesquioxide materials for efficient high-power operation

- Material properties

Yb-doped cubic sesquioxides have been recognized as a potentially more efficient gain material than Yb:YAG [100-108]. A high mechanical strength in combination with excellent thermal properties and high absorption cross sections make them ideally suited for the TDL geometry (see Table 4.II). Although these cubic sesquioxide materials are known since 1957 [106], the rather high melting temperature of about 2400°C prevented the growth of high quality crystals of the size required for TDL operation. This resulted for many years in a poor crystal quality and moderate optical-to-optical efficiencies [109, 110].

	Yb:LuScO	Yb:ScO	Yb:LuO	Yb:YAG
Thermal conductivity @8.10 ²⁰ cm ⁻³ (W/m·K)	3.5	7	12	7
Cation density (10 ²⁰ cm ⁻³)	3.1	3.36	2.85	1.38
Pump wavelength (nm)	975.7	975.1	976	940
Absorption cross-section (10 ⁻²⁰ cm ²)	3.3	4.4	3.1	0.8
Absorption bandwidth (nm)	2.4	2.1	2.9	12.5
Emission wavelength (nm)	1038	1041	1034	1030
Emission cross-section (10 ⁻²⁰ cm ²)	0.89	1.44	1.26	1.89
Emission bandwidth (nm)	22	11	12	9
Melting temperature (°C)	2370	2430	2450	1940

Table 4.II: Relevant properties of sesquioxide materials for modelocked TDLs. More details and other properties of these materials can be found in [23].

During the last years, these difficulties were overcome with the heat exchanger method (HEM) for the growth of high quality, large scale sesquioxide crystals [105]. The first cw and modelocked experiments in the thin-disk geometry were based on Yb:LuO [101, 111], followed by

successful cw-laser operation of $\text{Yb:Sc}_2\text{O}_3$ (Yb:ScO) crystals [112]. More recently, the disordered LuScO was successfully introduced as a host material for the Yb-ion [113]. The broad spectra resulting from the disordered lattice resulted in the first modelocking experiment to reach 227 fs, which was, at the time, the shortest pulses from a modelocked thin-disk oscillator [92].

- Cw results with high efficiency

	Yb:LuScO	Yb: ScO	Yb:LuO
Laser wavelength (nm)	1041	1042	1034
Outcoupling transmission (%)	1.2	1.2	2.7
Disk thickness (μm)	200	200	250
Doping concentration (%)	3	2.4	2
Pump spot diameter (mm)	4	4	2.6
Pump power (W)	365	380	413
Output power (W)	250	264	301
Optical-to-optical efficiency (%)	69	70	73
Slope efficiency (%)	81	80	85
Pump power density (kW/cm^2)	2.9	3	7.8

Table 4.III: Cw multimode experiments performed with different sesquioxide materials, showing their potential for high-power operation in the thin-disk geometry.

Cw multimode experiments performed during the timeframe of this thesis showed that these improved Yb-doped sesquioxides achieve higher efficiencies than any other gain material in the TDL geometry. For all materials tested (Yb:LuO , Yb:ScO and LuScO) slope efficiencies $> 80\%$ could be demonstrated using a VBG-stabilized diode to pump these materials into the zero-phonon line (ZPL). These results are summarized in

Table 4.III, and details about the performed experiments can be found in [114].

In this Chapter we focus on the potential of this material family for short pulse generation. We will show that nearly bandwidth limited pulses can be obtained with several materials from this family (Yb:LuO, Yb:LuScO and Yb:ScYLO). The spectroscopic detail of each one of these materials will be presented with the obtained experimental results.

4.2 Short pulses from Yb:LuO

4.2.1 Yb:LuO : a promising candidate for outperforming Yb:YAG

The most promising sesquioxide material in terms of average power scaling is Yb:LuO. This material exhibits a higher thermal conductivity than Yb:YAG ($\kappa(10 \text{ at. } \%) = 6.6 \text{ Wm}^{-1}\text{K}^{-1}$ for Yb:YAG and $\kappa(5 \text{ at. } \%) = 11.7 \text{ Wm}^{-1}\text{K}^{-1}$ for Yb:LuO for an equivalent doping concentration of $1.4 \cdot 10^{21} \text{ cm}^{-3}$). Furthermore, it has an about three to four times higher absorption cross-section at the zero-phonon line (ZPL) (976 nm) than Yb:YAG at its typical pump wavelength of 940 nm (Figure 4.2, left). This does not only allow the fabrication of thinner disks but also reduces the thermal load in the crystal as the quantum defect is about 38% lower. Pumping Yb:YAG at its ZPL (969 nm) is also possible [115]. However, in Yb:YAG, the peak emission cross section at the ZPL is very similar to that of the broad peak at 940 nm (Figure 4.2, left). Therefore, the benefit of pumping at the ZPL is, in this case, limited to the lower quantum defect of $\approx 31\%$. Given the small advantage in terms of efficiency and the higher constraints imposed on the pump linewidth that require using VBG stabilized diodes currently limited to $\approx 800 \text{ W}$ of output power, it seems more likely that future Yb:YAG modelocked TDLs will still be pumped at its broader line at 940 nm. In addition, the availability of high quality very thin disks that can be cooled very efficiently further weakens the need to pump Yb:YAG at the ZPL.

Yb:LuO exhibits nearly double the emission bandwidth of Yb:YAG (Figure 4.2, right), making it an excellent candidate for the generation of short pulses at high power levels. The first modelocked TDL based on this material was presented in 2007 and delivered an average power of 25 W

with a pulse duration of 523 fs [116]. During the time frame of this thesis, subsequent power scaling by increasing the pump spot size on the disk led to a maximum average output power of 141 W in 738 fs long pulses. This was, for many years, the highest output power reported from a modelocked oscillator [30]. The optical-to-optical efficiency of over 40% was higher than typically reported for modelocked Yb:YAG TDLs.

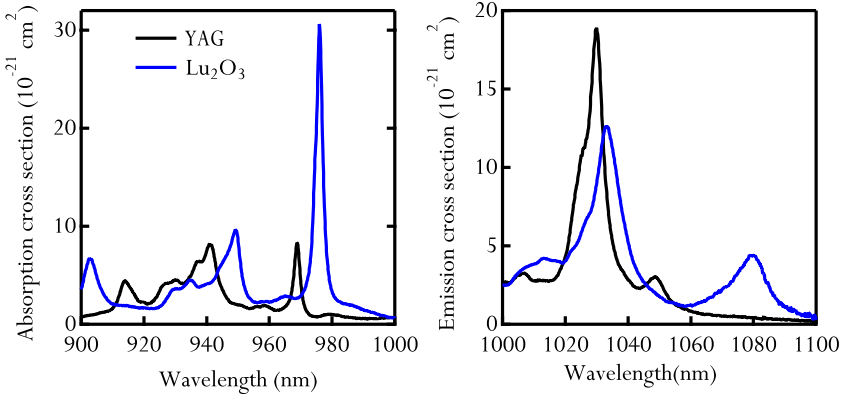


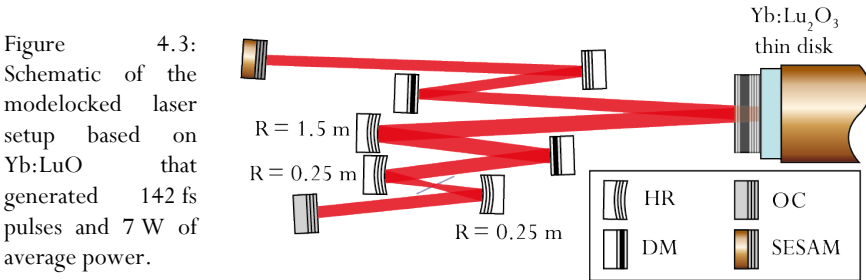
Figure 4.2: Left: Absorption cross section of Yb:LuO compared to that of Yb:YAG. Right: Emission cross section of Yb:LuO compared to that of Yb:YAG.

The potential of this material for short pulse generation in the thin-disk geometry was not fully exploited until the work presented in this thesis. In a very promising first experiment, 40 W of average power and 329 fs pulses were demonstrated [84]. In the experiments discussed in this thesis, we could nearly exploit the full emission bandwidth of this material achieving 142 fs at an average power of 7 W. The record-short pulses of this oscillator enabled the first detection of the CEO frequency of a modelocked TDL directly from the oscillator. These results will be presented in Chapter 5. In a second experiment, we show the first step in power scaling while keeping the short pulse duration, and demonstrate 25 W and 185 fs.

4.2.2 Yb:LuO modelocked thin-disk laser with 7 W, 142 fs [85]

- Experimental setup

The laser setup used for this experiment is shown in Figure 4.3. The thin disk, used as a folding mirror in the single-mode cavity, consisted of a 150- μm thick, 3%-doped Yb:LuO disk mounted on a 1.4-mm thick diamond heatsink, soldered on a back-cooled copper mount. The disk was glued on the diamond heatsink using the method described in [117] and had a wedge of 0.1° in order to avoid residual reflections which can be coupled to the resonator and destabilize modelocked operation. In order to efficiently pump Yb:LuO at its narrow ZPL, we used a volume Bragg grating (VBG) stabilized pump diode [28] that emits at a central wavelength of 976 nm in a narrow linewidth $\Delta\lambda < 0.5$ nm. The thin-disk module was arranged for 24 pump passes through the disk enabling an absorption $>95\%$ of the pump radiation. Throughout this experiment, we used a pump spot diameter of 1.9 mm.



In order to achieve soliton modelocking [34, 36], we used two GTI-type mirrors that accounted for -2200 fs^2 of GDD. A 1.5-mm thick uncoated YAG plate, introduced at a focus of $\approx 200 \mu\text{m}$ radius accounted for the necessary self-phase modulation (SPM) to balance the negative dispersion in the cavity. Furthermore, it ensures a linearly polarized output. The outcoupling coefficient was 4%.

• Evaluation of SESAM parameters

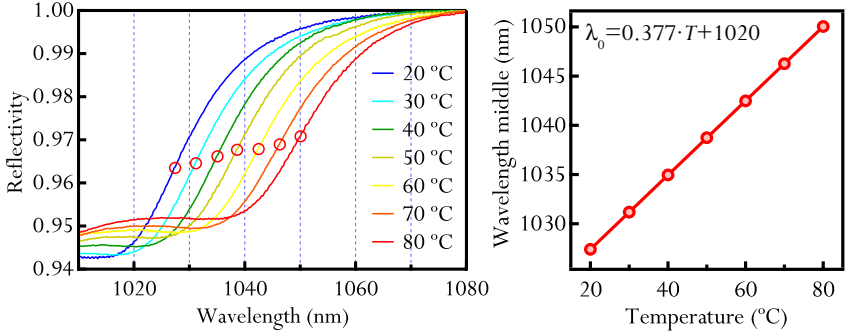


Figure 4.4: Left: Measurement of the linear reflectivity of the SESAM versus wavelength for different temperatures. Right: Evaluation of the rate of this shift with temperature.

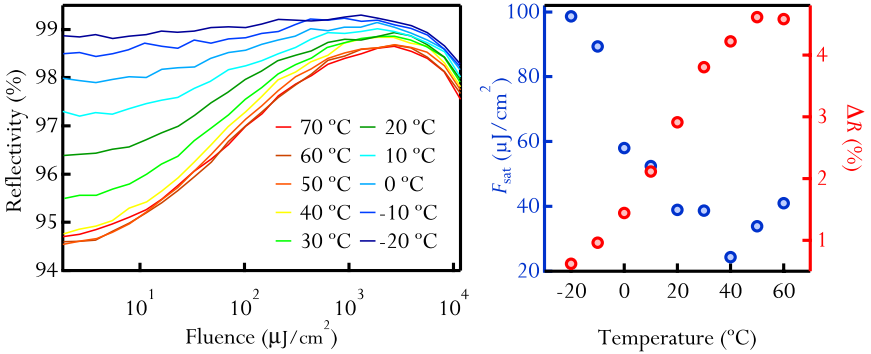


Figure 4.5: Left: Nonlinear reflectivity measurements at different temperatures. The performed temperature variation allows us to approximate the behavior of this SESAM at room temperature for a wavelength range of ≈ 1011 nm up to ≈ 1045 nm. Right: Variation of the fit parameters (ΔR and F_{sat}) of these nonlinear reflectivity measurements with temperature.

The SESAM used in this experiment is similar to the one described in Chapter 3, Part II. It consists of a standard DBR and four 7-nm thick InGaAs QWs, placed two-by-two in consecutive antinodes of the standing wave pattern of the electric field. The absorbers were embedded in AlAs layers and were grown at a low temperature of 270°C. For this first experiment, where short pulse durations were targeted, we did not apply a

dielectric topcoating, in order to fully benefit from the modulation depth of the sample.

We characterized this sample at 1030 nm using the setup described in Chapter 3 (Paragraph 3.1.1) and measured a saturation fluence $F_{\text{sat}} = 36 \mu\text{J}/\text{cm}^2$, a modulation depth $\Delta R = 3.3\%$, nonsaturable losses $\Delta R_{\text{ns}} = 0.7\%$ and a fast recovery time of $\tau_{1/e} = 1.9 \text{ ps}$. The laser wavelength of our laser was longer than the wavelength used for the SESAM characterization. In order to evaluate the parameters of this SESAM at the correct wavelength, we performed temperature dependent linear (Figure 4.4) and nonlinear reflectivity measurements (Figure 4.5). In Figure 4.4 (left), we present the linear reflectivity of the sample versus wavelength for different temperatures of the sample. These curves were measured using a spectrophotometer (Varian Cary 5E). In Figure 4.4 (right), we evaluate the obtained shift by measuring the wavelength where the curvature of the reflectivity curve changes sign for different temperatures. For anti-resonant structures, this allows us to measure the rate at which the emission peak of the QWs shifts with temperature. In this way, it is possible to approximate the behavior of a SESAM at another wavelength than the one used to characterize it.

In our laser setup, the SESAM was water-cooled to stabilize its temperature (to $\approx 18^\circ\text{C}$), and the laser operated at a wavelength of 1035 nm. Given the slope of 0.377 nm/K measured for this sample, and the measurement wavelength of 1030 nm, a good approximation of the parameters of our SESAM in our laser setup is given by the measurement performed at $T = 0^\circ\text{C}$ (Figure 4.5 left and right). At this temperature, we obtained $F_{\text{sat}} = 58 \mu\text{J}/\text{cm}^2$, a modulation depth $\Delta R = 1.5\%$, nonsaturable losses $\Delta R_{\text{ns}} = 0.6\%$ and a recovery time of $\tau_{1/e} = 1.9 \text{ ps}$. The laser spot size on the SESAM was $\approx 350 \mu\text{m}$.

- Modelocking result

We achieved stable modelocking up to an average power of 7 W. At this average power, pulses as short as 142 fs were obtained with an optical-to-optical efficiency of 15%. This corresponds to a pump power of 47 W. The laser operated at a repetition rate of 64 MHz, leading to a pulse energy of

0.1 μJ and a peak power of 0.7 MW. The pulses were close to the transform-limit of the spectrum with a time-bandwidth product of 0.34 (ideal sech^2 0.315) (Figure 4.6). The achieved modelocked optical spectrum (8.5 nm FWHM) is $>70\%$ of the available FWHM emission bandwidth of Yb:LuO, confirming the large potential of this material in terms of short pulse generation in the thin-disk geometry.

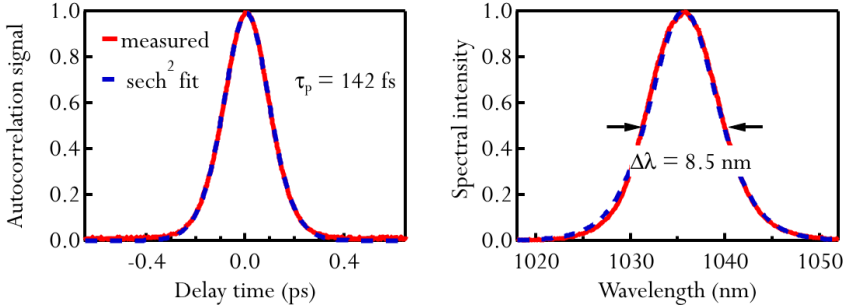


Figure 4.6: Left: Measured autocorrelation trace at 7 W average power and corresponding fit assuming a sech^2 pulse shape. Right: Measured optical spectrum of the pulses, and corresponding sech^2 fit showing a 8.5 nm wide spectrum (FWHM).

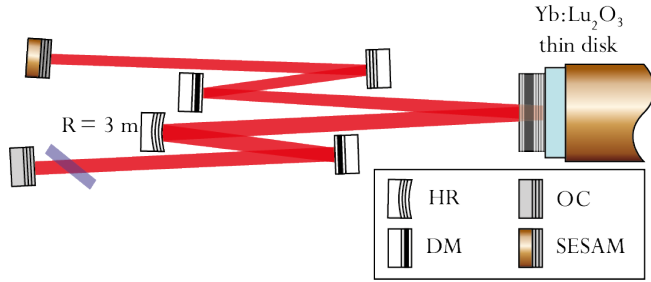
In this first proof-of-principle experiment, we focused on obtaining short pulses. Therefore, we used small spot sizes on the disk and the SESAM in order to operate in a relaxed cavity configuration with low misalignment and thermal sensitivities [26, 118] and to minimize Q-switching instabilities [32]. Furthermore, we achieved the crucial SESAM parameters in samples with moderate saturation fluences. In the next Paragraph, we present a first straightforward power-scaling step, where we demonstrated an average power of 25 W while keeping the pulses short with 185 fs.

4.2.3 Power scaling to 25 W, 185 fs

In order to achieve higher average power, we enlarged the pump spot on the disk from 1.9 mm to 2.6 mm and on the SESAM from $\approx 350 \mu\text{m}$ to $\approx 600 \mu\text{m}$. We used the same pump source and pump layout as described in the previous Paragraph.

The schematic cavity layout is presented in Figure 4.7. We used two GTI-type mirrors that accounted for -2200 fs^2 of GDD per roundtrip. A 7-mm thick uncoated YAG plate introduced the necessary SPM for soliton modelocking. Furthermore, it ensured a linearly polarized output.

Figure 4.7:
Schematic of the modelocked laser setup based on Yb:LuO that generated 185 fs pulses and 25 W of average power.



In addition to the larger spot sizes used, we used a higher outcoupling rate of 6%, to relax intracavity levels. Furthermore, we used the SESAM described in the previous Paragraph, but with a one-pair $\text{SiO}_2/\text{Si}_3\text{N}_4$ quarter-wave dielectric topcoating. This topcoating increases the saturation fluence of the sample and its damage threshold [38], but reduces its modulation depth. The parameters of this sample was measured at 1030 nm and evaluated at 1035 nm following the same procedure we described in the previous Paragraph. The evaluated parameters are a saturation fluence $F_{\text{sat}} = 110 \mu\text{J}/\text{cm}^2$, a modulation depth $\Delta R = 0.9\%$, nonsaturable losses $\Delta R_{\text{ns}} = 0.4\%$ and a recovery time of $\tau_{1/e} = 1.9 \text{ ps}$.

We obtained stable modelocking up to an average power of 25 W. At this average power, we achieved pulses as short as 185 fs with an optical-to-optical efficiency of 18.5%. The laser operated at a repetition rate of 66.5 MHz, resulting in a pulse energy of $0.4 \mu\text{J}$ and a peak power of 1.8 MW. The pulses were close to the transform-limit of the spectrum with a time-bandwidth product of 0.349 (ideal sech^2 0.315) (Figure 4.8).

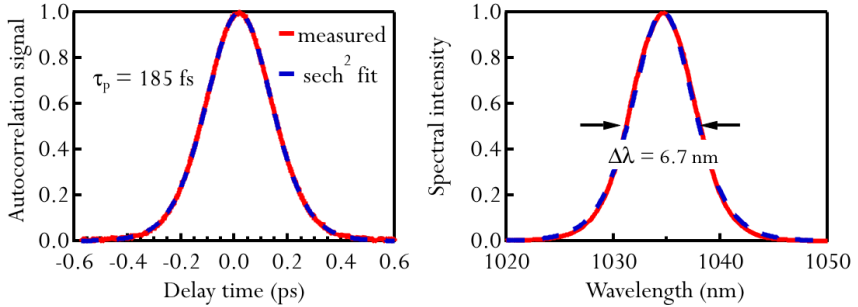


Figure 4.8: Left: Measured autocorrelation trace at 25 W average power and corresponding fit assuming a sech^2 pulse shape. Right: Measured optical spectrum of the pulses, and corresponding sech^2 fit showing a 6.7 nm wide spectrum (FWHM).

In this experiment, we were interested in keeping the pulse duration short (sub-200 fs) and obtaining high average powers. Several factors contributed, in this case, to the slightly longer pulses obtained. On the one hand, the high-damage threshold SESAM used for this experiment had a smaller modulation depth than the uncoated sample. Furthermore, we used a higher output-coupling rate, which results in a higher gain per cavity roundtrip, also increasing the minimum achievable pulse duration.

A possibility that is currently being investigated is the use of a similar SESAM with high damage threshold, temperature-controlled to obtain a somewhat higher modulation depth. However, this would result in a lower saturation fluence, which needs to be compensated with a larger spot size. This should represent no problem in terms of Q-switching, given the higher damage threshold of the samples. Another possible improvement is, as indicated in the outlook of Chapter 3, to design a SESAM with larger number of QWs and more dielectric pairs, which will combine a higher damage threshold and a higher saturation fluence. As we mentioned in the outlook of Chapter 2 these novel structures are currently being investigated.

4.3 Short pulses from Yb:LuScO

4.3.1 Mixed cubic sesquioxide Yb:LuScO

For the generation of even shorter pulses, the ILP group (University of Hamburg) developed the stoichiometric mixture of Yb:LuO and Yb:ScO₃ resulting in Yb:LuScO [113]. This material succeeded in combining the two emission spectra of Yb:LuO and Yb:ScO that lie roughly 7 nm apart, in a 22-nm-broad emission bandwidth centered around 1038 nm (Figure 4.9). The same advantages in terms of absorption cross section that were discussed for Yb:LuO are true for Yb:LuScO, with an even higher absorption cross section at the ZPL.

The first crystal tested in modelocked operation was of limited quality, which explains the moderate average power of 7.2 W. Nevertheless, this result took over the record in terms of short pulse duration from Yb:KYW (240 fs) with a pulse duration of 227 fs in 2009 [92]. In contrast to many other broadband materials that exhibit anisotropic thermal and optical properties (such as Yb:KYW or Yb:YCOB) this material has an isotropic crystal structure. This indicates that power scaling to the 100 W level should be feasible from this material.

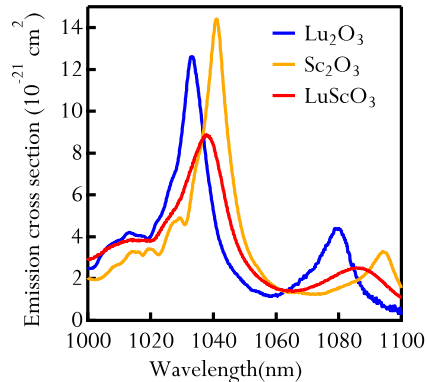


Figure 4.9: Emission cross section of Yb:LuScO as a result of the stoichiometric mixture of ScO and LuO.

Since the above-mentioned first demonstration of an Yb:LuScO modelocked TDL [92], the crystal quality was significantly improved. In a first experiment, we demonstrate the first step in average power scaling of

this promising gain material to 23 W with pulse duration of 235 fs [119]. In a second experiment aiming for pushing the pulse duration of this material, we demonstrate a SESAM modelocked TDL based on this material with a pulse duration of 96 fs at an average power of 5.1 W. These are the shortest pulses ever obtained from a modelocked TDL, reaching for the first time the sub-100 fs milestone [120].

4.3.2 High-power modelocked Yb:LuScO thin-disk laser

- Experimental setup

In this experiment, we used a 150 μm -thick Yb(3%):LuScO crystal from the second growth run of this material. The disk was glued on a 1.4-mm-thick diamond heatsink. This was the first experiment using a sesquioxide thin disk mounted on a diamond heatsink. This crystal was pumped with the same VBG- stabilized fiber-coupled diode described in the experiments performed with Yb:LuO. We used a pump spot diameter of 2.6 mm. The unpumped disk was characterized with a polarized Michelson interferometer and the mean radius of curvature of this disk was measured to be $R_m = 1.95$ m, with no significant astigmatism.

- Cw high-power operation

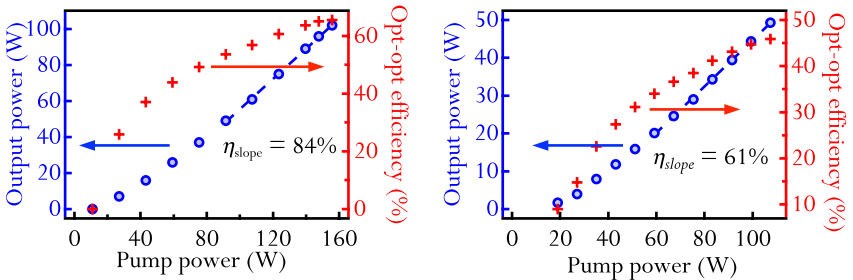


Figure 4.10: Left: cw output power slope in a simple linear multimode laser cavity, indicating a slope efficiency $> 80\%$ Right: cw output power slope in fundamental mode operation.

In a linear cw multimode cavity that consisted of a 1.2% transmission curved mirror with a radius of curvature of 100 mm and the HR-backside

of the disk, we measured output powers of more than 100 W with an optical-to-optical efficiency of 63% and a slope efficiency of 84% (Figure 4.10, left).

In a cw fundamental transverse mode folded cavity with an output coupler transmission of 2.6% we achieved 50 W of output power with an optical-to-optical efficiency of 45% and a slope efficiency of 61%. At this output power, we measured an $M^2 < 1.3$, suitable for modelocking experiments (Figure 4.10, right). Although this cavity design allows us to compensate for small changes of the thermal lens [30], significant changes were not required to achieve single-mode operation up to the demonstrated 50 W.

At the maximum output power levels presented, we did not observe a decrease in the optical-to-optical efficiency. Therefore we could have, in principle, pushed for higher power levels in both cases. However, we did not further increase the pump power to avoid damage of the crystal before the modelocking experiments.

As we discussed in Chapter 1, this mounting technique should enable better heat removal, but most importantly more robust fundamental mode operation. We believe this contributed to achieve the cw performance presented here. However, during the modelocking experiments, we observed damage of the crystal at low pump intensity below 2 kW/cm^2 . Note that a thicker, $200\text{-}\mu\text{m}$ disk from the first growth run of this material, soldered with indium-tin on a copper heatsink delivered a comparable multimode performance (140 W) under the same conditions and could withstand intensities up to 3.8 kW/cm^2 with high efficiencies. This seems to suggest an imperfect mounting on the diamond heatsink.

- High-power femtosecond operation

For the modelocking experiment, we used the same fundamental mode cavity that yielded 50 W of cw power, but a higher outcoupling rate of $T = 5\%$. The higher outcoupling rate was chosen to reduce the intracavity power and therefore relax the fluence level on the SESAM in order to reach higher average powers, at the expense of a small reduction of the optical-to-optical efficiency. We introduced a fused silica Brewster plate

with a thickness of 3 mm for polarization and SPM control (Figure 4.11) and two GTI-type mirrors in the cavity that accounted for a total GDD per roundtrip of -2200 fs^2 . The dielectric topcoated high damage threshold SESAM, which was especially designed for this experiment, was described in detail in Chapter 3 (Paragraph 3.2.2). Its saturation parameters are (at 1030 nm) $F_{\text{sat}} = 70 \mu\text{J}/\text{cm}^2$, $\Delta R = 1.3 \%$, $\Delta R_{\text{ns}} = 0.4\%$ and a recovery time of $\tau_{1/e} = 2 \text{ ps}$. At the time of the experiment, the temperature dependent measurement setup was not available. Therefore, these absorber parameters still need to be corrected for the correct laser wavelength ($\approx 1039 \text{ nm}$). The laser mode radius on the SESAM in this cavity was $\approx 390 \mu\text{m}$.

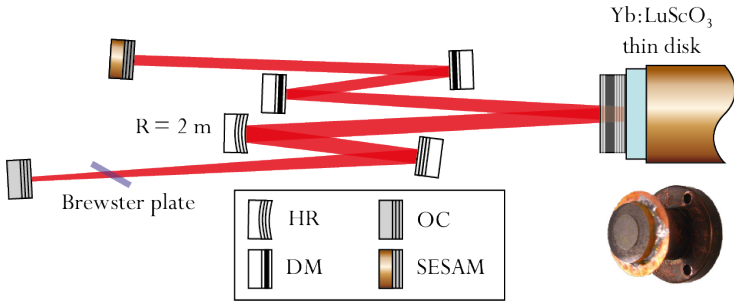


Figure 4.11: Schematic of the cavity used for the modelocking experiment and picture of the disk on a diamond heatsink.

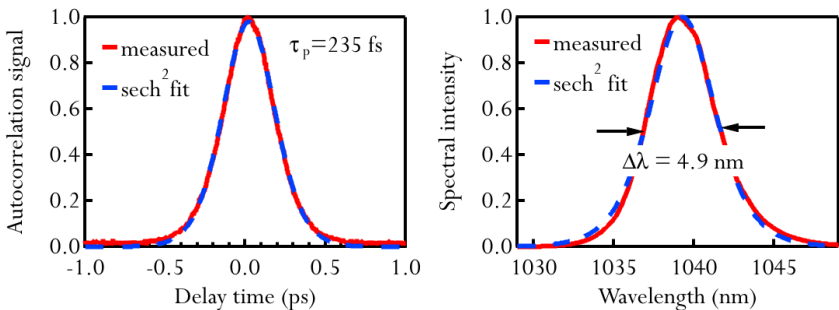


Figure 4.12: Left: Measured autocorrelation trace at 23 W average power and corresponding fit assuming a sech^2 pulse shape. Right: Measured optical spectrum of the pulses, and corresponding sech^2 fit showing a 4.9 nm wide spectrum (FWHM).

We obtained stable modelocking starting at 17.5 W up to 23 W of average power. At the highest modelocked average power level, the pulses were 235 fs long and were nearly transform-limited with a time bandwidth product of 0.32 (ideal sech^2 0.315) (Figure 4.12).

The optical-to-optical efficiency was 21%, corresponding to a pump power of 109 W. The repetition rate of the pulses was 70 MHz. Notice that compared to previous results using Yb:KYW in which similar performance was obtained, no dispersive intracavity elements were necessary to flatten the emission spectrum, showing the potential of Yb:LuScO for short pulse generation at even higher powers.

Further attempts to increase the average power of the laser resulted in damage of the disk. This was probably due to a defect in the gluing onto the diamond heatsink. However, we believe that sub-200-fs pulses could have been achieved at higher average powers.

4.3.3 Sub-100 fs Yb:LuScO thin disk laser [40]

In a second experiment aiming to explore the limits in terms of pulse duration of modelocked TDLs, we used another Yb:LuScO disk with a thickness of 200 μm . In this case, the disk was mounted on a 1.4-mm thick diamond, which was directly water-cooled through the back surface for more efficient heat removal. We used the same VBG stabilized pump diode described in the previous experiments and the same pump arrangement. For this first proof-of-principle experiment, we used a moderate pump spot diameter of 1.9 mm.

For stable soliton modelocking, we introduced five GTI-type mirrors that accounted for 2800 fs^2 of negative GDD per roundtrip. Two uncoated YAG plates inserted at Brewster's angle with thicknesses of 5 and 7 mm ensured linear polarization and introduced SPM to balance the negative GDD for stable soliton modelocking (Figure 4.13). We used an output coupler with 2.6% transmission, chosen to achieve the best compromise between average power and pulse duration.

The use of undoped YAG is justified by its high nonlinear refractive index n_2 , resulting in γ factors 2-3 times higher than that of fused silica ($n_2 = 3 \times 10^{-16} \text{ cm}^2/\text{W}$ for fused silica and $n_2 = 8 \times 10^{-16} \text{ cm}^2/\text{W}$ for undoped YAG [121]) This allows us to introduce large amounts of nonlinearity for

the generation of very short pulses. It is worth noticing that using undoped YAG for SPM also introduces significant amounts of positive dispersion (in this case $\approx 1600 \text{ fs}^2$ of positive GDD). This was taken into account in the design of the laser. The large amount of negative dispersion was partly compensating for the positive dispersion of the YAG plates. Using only one plate would minimize small losses introduced at Brewster's angle. However, at the time of the experiment, the maximum thickness available was 7 mm, therefore two plates were introduced at the expense of a small loss in output power. Another approach would be to introduce a focus in the cavity design and place a thinner plate at this position. However, precise control of the amount of SPM is more difficult with a tight focus. An interesting alternative is the use of materials with much higher n_2 such as ZnSe ($\gamma = 3 \times 10^{-14} \text{ cm}^2/\text{W}$) [122]. However, obtaining such crystals with the optical quality required for intracavity use is challenging.

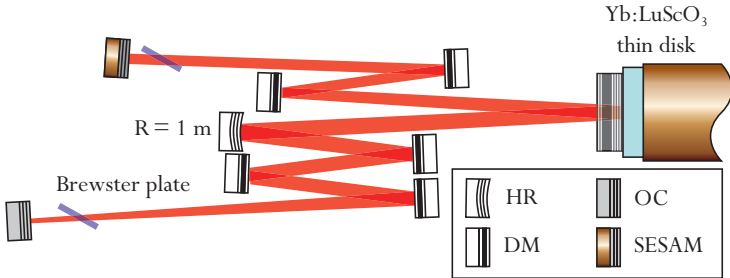


Figure 4.13: Schematic of the cavity used for the sub-100 fs modelocking experiment.

The SESAM used in this experiment is the same uncoated sample described in the previous Paragraph for modelocking of Yb:LuO. The same procedure described in 4.2.2 was used to evaluate the parameters of this SESAM at the correct laser wavelength. The SESAM parameters measured at -10°C at 1030 nm best approximate our laser wavelength of 1039 nm. We obtained $F_{\text{sat}} = 90 \mu\text{J}/\text{cm}^2$, a modulation depth $\Delta R = 1.2\%$, nonsaturable losses $\Delta R_{\text{ns}} = 0.4\%$ and a recovery time of $\tau_{1/e} = 1.9 \text{ ps}$.

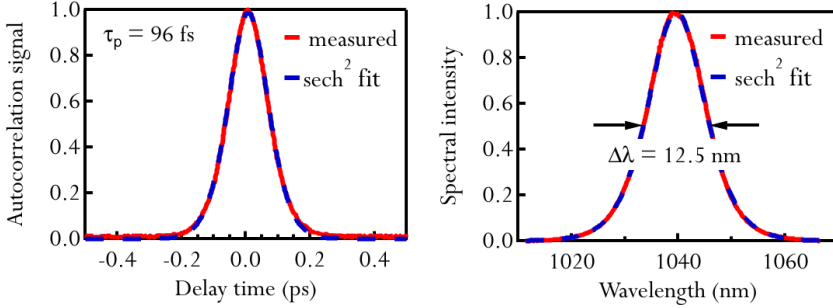


Figure 4.14: Left: Measured autocorrelation trace at 5 W average power and corresponding fit assuming a sech^2 pulse shape. Right: Measured optical spectrum of the pulses, and corresponding sech^2 fit showing a 12.5 nm wide spectrum (FWHM).

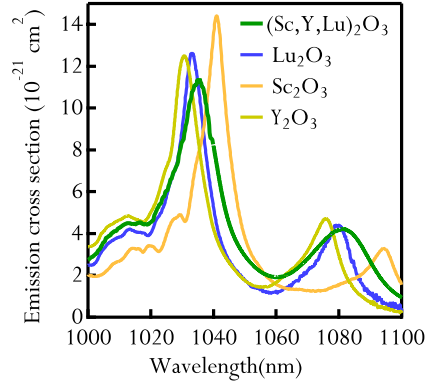
Stable modelocking was obtained with up to 5.1 W of average power with an optical-to-optical efficiency of 11%. The pulse duration at the maximum power level was 96 fs. The laser operated at a repetition rate of 77.5 MHz and the pulses were close to the transform-limit of the measured spectrum with a time-bandwidth product of 0.33 (ideal sech^2 0.315)(Figure 4.14). These are, to our knowledge, the shortest pulses ever obtained from a modelocked TDL, reaching for the first time the sub-100 fs regime.

Both shorter pulse durations and higher average powers should be feasible from this laser material. As we discussed for Yb:LuO, further SESAM optimization will allow us higher powers by enlarging the spot sizes on the disk and on the SESAM. In the case of Yb:LuScO, the larger emission bandwidth relaxes the requirements on the SESAM parameters, and should enable straightforward power scaling such as described in the previous Paragraph for Yb:LuO.

4.4 Short pulses from Yb:ScYLO

The approach of mixing different sesquioxide materials to obtain broader bandwidths continued to Yb:ScYLO resulting from the combination of Yb:ScO, Yb:Y₂O₃ (Yb:YO) and Yb:LuO (Figure 4.15). However, the first growth run of this material revealed no significant spectroscopic advantages over Yb:LuScO.

Figure 4.15: Emission cross section of sesquioxide material Yb:ScYLO, as a result of the mixture of LuO, YO, and ScO.



Nevertheless, it is an interesting isotropic material that exhibits an emission bandwidth of 18.5 nm FWHM, making it a good candidate for short pulse generation. Two thin disks from the first growth run of this material were tested in modelocked operation. In the first experiment, 236 fs were demonstrated at an average power of 3.9 W [89]. The low average power was due to the very poor quality of the crystal, which showed a strongly asymmetric radius of curvature and several grain boundaries, which limited the obtainable power in fundamental mode operation to only few watts. It is worth noticing that a similar problem was observed in the first results of Yb:LuScO [92] for which the second growth run demonstrated disks with significantly higher quality.

Given the quality of the available disks from the first growth run, we focused on exploring the limits in terms of pulse duration of this material. We used the same SESAM as in the sub-100 fs Yb:LuScO experiment described in the previous Paragraph. We obtained 5 W of average power and a remarkable short pulse duration of 101 fs. This was obtained at a repetition rate of 70 MHz, resulting in a pulse energy of 0.1 μ J.

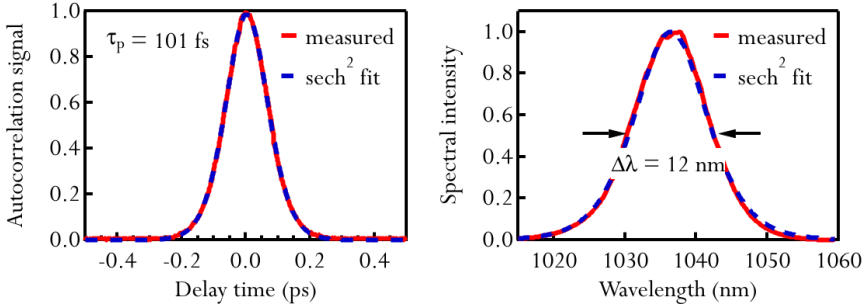


Figure 4.16: Left: measured autocorrelation trace at 5 W average power and corresponding fit assuming a sech^2 pulse shape. b) measured optical spectrum of the pulses, and corresponding sech^2 fit showing a 12 nm wide spectrum (FWHM).

This result, which shows very similar performance to what is demonstrated with Yb:LuScO, further confirms the suitability of sesquioxide materials for short pulse generation.

4.5 Summary and discussion

The different results presented in this Chapter are summarized in Table 4.IV.

Material	P_{av}	E_p	τ_p	f_{rep}	P_{pk}	Ref.
Yb:LuO	7 W	0.1 μJ	142 fs	64 MHz	0.7 MW	[85]
	25 W	0.4 μJ	185 fs	66 MHz	1.8 MW	[86]
Yb:ScYLO	3.9 W	0.1 μJ	236 fs	36 MHz	0.4 MW	[89]
	5 W	0.1 μJ	101 fs	70 MHz	0.6 MW	x
Yb:LuScO	23 W	0.3 μJ	235 fs	70 MHz	1.2 MW	[65]
	5 W	0.1 μJ	96 fs	77 MHz	0.6 MW	[40]

Table 4.IV: Summary of laser results presented in this Chapter. x indicates a result that has not been reported in a publication or conference proceedings up-to-date.

The most remarkable common point of all these results is the large fraction of the available emission bandwidth that could be exploited in modelocked operation. This seems to indicate that much shorter pulses can be obtained with materials with significantly larger emission bandwidths,

such as for example, Yb:CALGO. In Figure 4.17, we plotted the emission bandwidth simultaneously with the demonstrated modelocked spectra for each material presented in this Chapter. The observed redshift of the modelocked spectrum compared to the peak emission wavelength is partly due to the low inversion level β used in all the demonstrated results. A low inversion level (corresponding to a low gain per roundtrip) is beneficial to push the pulse duration to the limits according to Formula (2.2). Furthermore, at a given output power, the resulting higher intracavity power also contributes to an increased nonlinear phase shift, which is also beneficial to obtain shorter pulses.

Strictly speaking, one should compare the modelocked spectrum not to the emission cross section, but to the exact gain cross section at the inversion level β at which the laser operates. This inversion level represents the fraction of active ions that are in the excited upper-state energy level. In the case where there are no other spectrally dependent loss elements in the laser cavity, the gain spectrum is modified for different inversion levels β according to

$$g(\lambda) = \beta\sigma_{\text{em}}(\lambda) - (1 - \beta)\sigma_{\text{abs}}(\lambda) \quad (4.1)$$

where $g(\lambda)$ is the gain cross section, and σ_{em} (resp. σ_{abs}) the emission (resp. absorption) cross sections. This is illustrated in Figure 4.18, for Yb:LuScO and Yb:LuO. In reality, there are always sources of spectrally dependent loss (such as the reflectivity of the different dielectric mirrors in the cavity, or the SESAM) and the precise determination of all these elements and their influence on the gain cross section is a complicated task. Therefore, a comparison to the emission spectrum is more adequate. Nevertheless, we estimate that in our experiments we operated in all cases at $\beta < 0.15$.

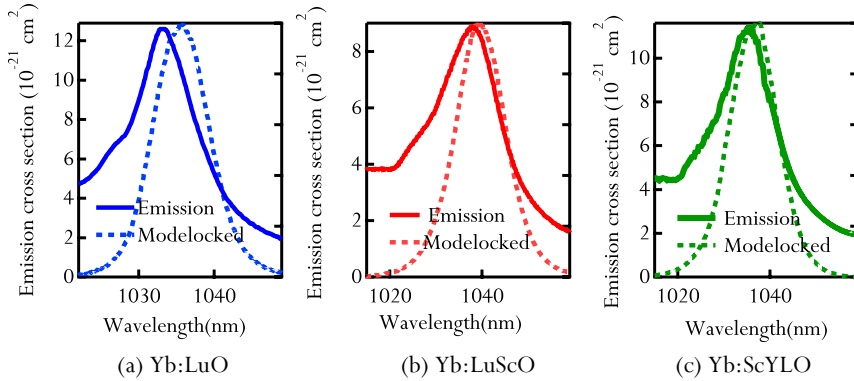


Figure 4.17: Emission cross-sections and modelocked bandwidth for the shortest pulses from different sesquioxide materials (a) Yb:LuO emission and modelocked spectra for the 142-fs pulses obtained at 7 W (b) Yb:LuScO emission and modelocked spectra for the 96-fs pulses obtained at 5 W (c) Yb:ScYLO emission and modelocked spectra for the 101-fs pulses obtained at 5 W.

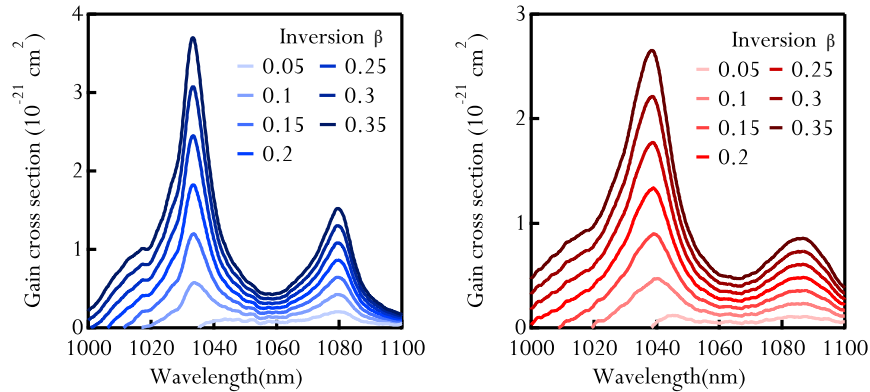


Figure 4.18. Left: Gain cross section of Yb:LuO for different inversion levels of the gain medium. Right: Gain cross section of Yb:LuScO for different inversion levels of the gain medium.

We believe that operating these lasers at low inversion level was an important point to obtain the record-short pulses demonstrated in this Chapter. As we can see in Figure 4.18, the shape of the gain spectrum changes significantly, and tends to become smoother at low inversion levels

both for Yb:LuO and Yb:LuScO. An important consequence of this is that further power scaling using these materials will require maintaining a low output-coupling rate (typically $<5\%$). The use of thinner disks ($< 100 \mu\text{m}$) from improved growth runs should support efficient fundamental-mode operation at these low inversion levels and at high output powers.

Another consequence of this point is that operation in vacuum (such as the oscillator presented in Chapter 6) will be crucial to reach the targeted 100-W level, given the high intracavity peak powers involved in the targeted oscillators. Furthermore, future improved dispersive mirrors and SESAM designs with low IA and high-damage thresholds such as the ones suggested in Chapter 3, Part III will be key to support these future steps. Finally, the use of novel materials with broader emission bandwidths relaxes these requirements, and will therefore be an ongoing topic of investigation.

Although the output power levels obtained at the record-short pulse durations are still moderate, the intracavity levels of these oscillators are in the order of several hundred watts, which already opens the door to driving nonlinear optics experiments inside the oscillator. This promising alternative will be discussed in more detail in the next Chapter.

Chapter 5 - Carrier-envelope offset detection of a modelocked thin-disk laser

A growing number of applications in metrology, spectroscopy and attosecond science could potentially benefit from the high average and peak powers available from table-top TDLs. In particular, the extremely high intracavity intensity of modelocked TDLs offers a new avenue to boost the average photon flux in high harmonic generation (HHG) [7, 8] and therefore generate a table-top source of vacuum ultraviolet (VUV) and extreme ultraviolet (XUV) radiation for such applications. The achievement of sub-100 fs pulses from such sources, presented in Chapter 4, represents a first step in the right direction.

However, another crucial aspect that had not been investigated prior to the work presented in this thesis is the potential of TDLs as stabilized high-power frequency combs. During this thesis, we achieved another important step and measured the first carrier envelope offset (CEO) frequency [123, 124] of a TDL.

This Chapter will be organized as follows. In the first Paragraph, we will present one of the most promising applications of the sources developed during this thesis, which consists of making use of the high intracavity levels inside TDLs to drive HHG. In a second Paragraph, we will give a short introduction to frequency combs and carrier envelope offset (CEO) detection. This will be followed by the experimental results achieved with our Yb:LuO TDL. Finally, we will conclude with some remarks on the next steps towards full stabilization of a TDL.

5.1 Towards high-harmonic generation inside a thin-disk laser

Making use of the high intracavity intensity levels inside a TDL to drive extreme nonlinear optics experiments is a promising approach that has not yet been demonstrated. Passive enhancement cavities [125-128] for femtosecond laser pulses have already shown that they are an ideal configuration for exploiting nonlinear processes between light pulses and matter. Currently, they are a topic of extensive research, mainly targeting the widespread area of HHG at MHz repetition rates. Up-to-date, passive enhancement cavities proved very successful: an impressive intracavity power of 18 kW at 78 MHz with 200 fs pulses was achieved [129] and power levels $> 200 \mu\text{W}$ in the UV were demonstrated [130], opening the door to exciting applications such as VUV/XUV precision spectroscopy on He^+ [131] or even exploring nuclear transitions [132]. Very recently, the first demonstration of direct XUV frequency comb spectroscopy of Argon was reported [133] at MHz repetition rate using a UV frequency comb driven by an ultrafast high-power fiber based system coupled to a passive enhancement cavity. However, these passive enhancement cavities require careful coherent coupling of femtosecond pulses from the driving laser into the resonator. The circulating pulse has to match the driving pulses, which becomes challenging in the presence of nonlinearities, phase distortions and dispersion inside the resonator. Furthermore, efficiently extracting the UV radiation from these very high finesse cavities is challenging [134, 135].

Driving HHG inside TDLs would be substantially simpler. In this case, both pulse formation and laser amplification are achieved inside the cavity, where the nonlinear process takes place. In addition, there is no need for coherent coupling and the circulating pulse can simply adapt to the present nonlinearity. Another potential advantage is that different transverse mode profiles can be achieved, for example TEM_{01} , for efficient output coupling of the high harmonics via a hole in a cavity mirror [136]. So far, the required short pulse durations (sub-100 fs) for efficient HHG had not been demonstrated for TDLs. Another key point, in particular for spectroscopy experiments, is the frequency stability of TDLs, which has not been studied before. The multimode pumping scheme of TDLs could potentially

increase the noise level such that a stable frequency comb cannot be realized [137].

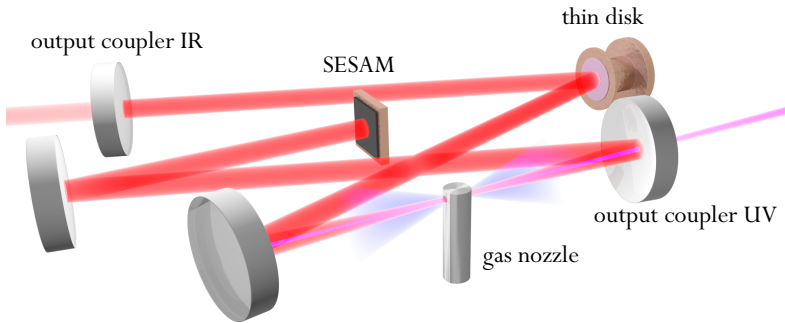


Figure 5.1: Suggested schematic setup for intralaser high-harmonic generation inside a TDL.

In Chapter 4, we showed that TDLs can access unprecedented short pulse durations, reaching sub-100 fs for the first time. Here, we present another milestone towards intralaser HHG using TDLs: we measured for the first time the CEO frequency of such a laser source, which will enable full stabilization of unamplified high-power oscillators.

5.2 Frequency combs and carrier-envelope offset frequency detection

5.2.1 Frequency combs

The term “frequency comb” simply refers to the frequency representation of a stable train of ultrashort pulses in the temporal domain (Figure 5.2). Strictly speaking, the spectrum of any modelocked laser can be a frequency comb provided that the pulses are stable enough in a given time window. In literature, the term “frequency comb” usually refers to a “stabilized frequency comb” most likely because this stabilization is crucial for most widespread applications of such combs. In fact, an unstable comb exhibits breathing and shifting of its teeth in fast time scales related to the noise level of the laser source, which limits their usability as “frequency rulers”.

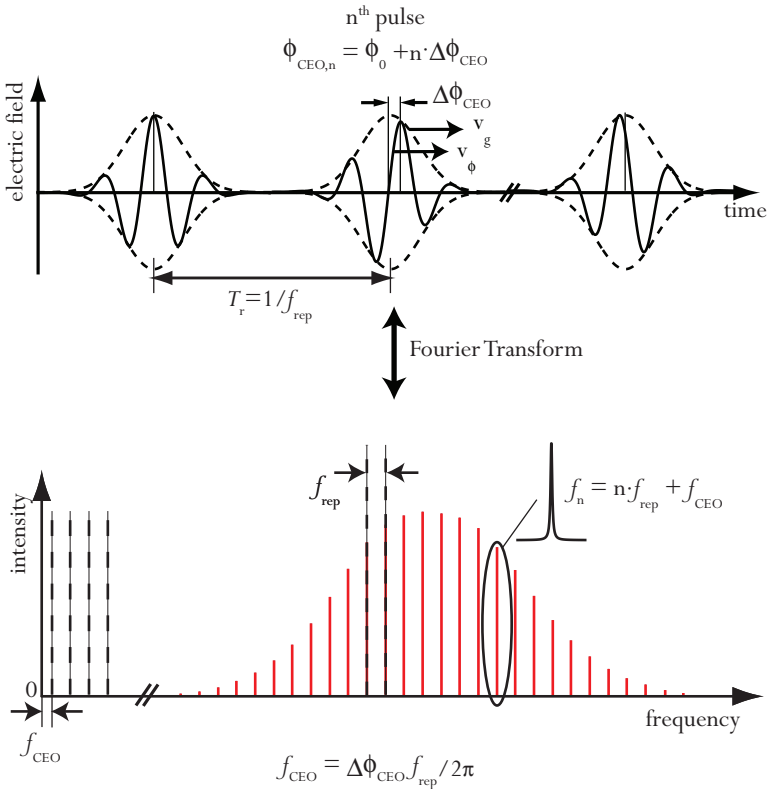


Figure 5.2: A frequency comb is the frequency representation of a stable train of ultrashort pulses.

In order to fully stabilize a frequency comb, two comb parameters need to be detected and locked:

- the repetition rate of the laser f_{rep} , which represents the spacing between the comb teeth in the frequency domain and the inverse of the period of the pulse train in the temporal domain.
- the CEO frequency of the laser f_{CEO} , which represents the offset of the first line of the comb to the zero-frequency. In the temporal domain, this represents the phase slip of the

maximum of the pulse envelope to the electric field from one pulse to the next one.

The repetition rate of the laser is straightforward to detect. Typical modelocked solid-state lasers have repetition rates in the range of some MHz up to a hundred GHz [51], which can be directly detected with standard fast photodiodes and studied with microwave analyzers.

The CEO frequency lies in a portion of the optical frequency spectrum where there is no spectral energy (Figure 5.2, bottom). Therefore, direct detection is not possible and more sophisticated detection schemes are required. The most commonly used method for CEO frequency detection is the so-called f -to- $2f$ interferometer [123]. This is the method used for the experiments described in this Chapter. However, it is worth mentioning that other promising alternatives are currently being investigated, but are mostly in the proof-of-principle state [138, 139].

Once these two parameters are monitored with a large enough SNR, electronic stabilization to an external reference is straightforward. The stabilized frequency comb can then be used as a very precise ruler in the frequency domain.

5.2.2 Carrier-envelope offset frequency detection schemes: f -to- $2f$ interferometer

A schematic of the principle of this detection method is illustrated in Figure 5.3. A portion of the low frequency part of a coherent octave-spanning spectrum is frequency doubled and beated with the portion of the spectrum one octave longer in frequency. The signal observed consists of several peaks containing the information of f_{CEO} . In particular, one set of lines is exactly separated by f_{CEO} as illustrated in Figure 5.4. In this figure, we schematically illustrate the measurement concept with one line of the spectrum (f_n), which is frequency doubled ($2f_n$) and beated with the line separated exactly by one octave (f_{2n}). This results in the wanted information $f_{\text{CEO}} = 2f_n - f_{2n}$. In reality, many comb lines contribute to the measured signal (all lines that verify $f_{\text{CEO}} = 2f_{n+m} - f_{2(n+m)}$, where the largest m is dependent on the optical filter used for selecting the short-frequency

“slice” of the spectrum and on the spectral shape imposed by the frequency doubling.

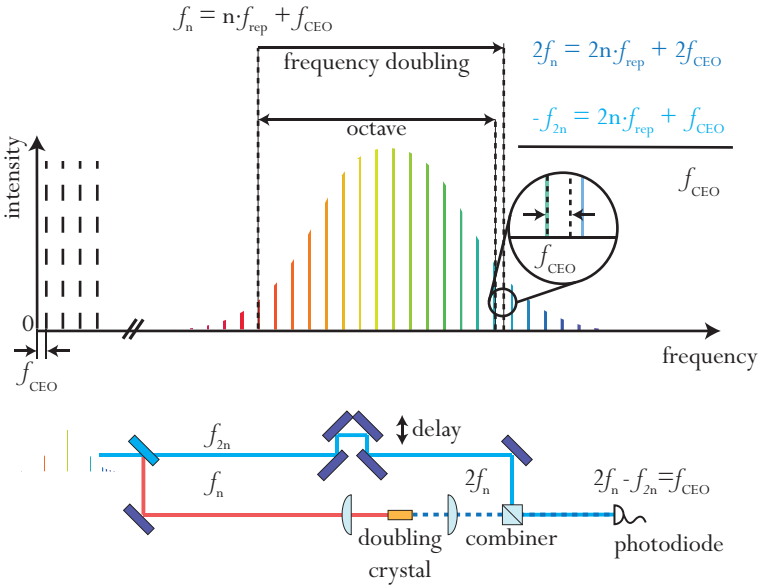


Figure 5.3: Principle of the f -to- $2f$ detection scheme [123] and interferometric setup for f_{CEO} detection.

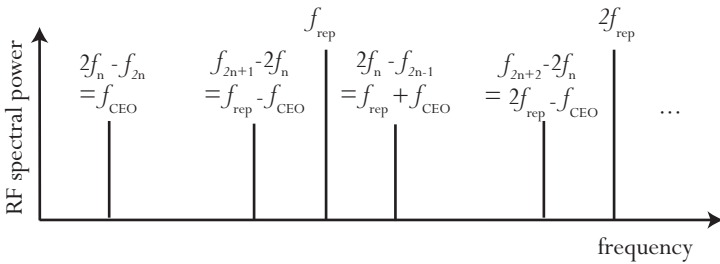


Figure 5.4: Beat signal observed by the detector in a standard f -to- $2f$ interferometer as a result of beating of lines with different spacing in the selected portion of the spectrum.

In addition to the beating signal at the frequency f_{CEO} , the beating signal also contains other lines with “indirect” information about f_{CEO} . For example, $f_{\text{CEO},2} = f_{\text{rep}} \cdot f_{\text{CEO}}$ that originates from the beating of the frequency

doubled components f_{2n} , but this time with f_{2n+1} . This is illustrated in Figure 5.4, in the case where $f_{\text{CEO}} < f_{\text{rep}}/2$, for some of the multiple beat components that can be observed.

One of the crucial requirements of this detection scheme is seeding the interferometer with a spectrum that is octave-spanning and coherent. Only few specialized systems based on Ti:sapphire exhibit such broad spectra directly from the oscillator. In particular, as we discussed in Chapter 4, TDLs are currently limited to pulse durations > 100 fs and the corresponding spectra are too narrow for directly seeding an f -to- $2f$ interferometer. Therefore, in order to make use of this detection scheme, external spectral broadening is required for detection of the CEO frequency. Supercontinuum generation (SC) in photonic crystal fibers (PCF) is an elegant way of reaching sufficient spectral broadening from standard femtosecond sources. However, the obtained SC needs to have sufficient degree of coherence to observe beating between its different parts. This poses extra challenges on the laser parameters and the fiber used for this purpose.

5.2.3 Supercontinuum generation and coherence properties

SC generation in PCFs is the result of several cascaded highly nonlinear processes, and the mechanisms involved in the broadening depend mainly on the input pulse parameters and the dispersion properties of the nonlinear fiber [140]. In some configurations, the spectral broadening can have a tendency to strongly amplify noise. In this case, even small pulse-to-pulse phase and amplitude fluctuations lead to strong differences in the generated SC, resulting in incoherent broadening. In order to achieve coherent broadening, the process generating the SC needs to have minimal noise amplification.

We focus here on SC generation obtained by soliton fission. In this regime, the pump wavelength is slightly longer than the zero dispersion wavelength of the fiber, in the negative dispersion regime. As its name indicates, this process is started with propagation of a high-order soliton in the fiber, resulting from the interplay of negative dispersion and self-phase modulation. The detailed description of soliton fission and the resulting properties of the generated SC have been extensively studied and lie

outside the scope of this thesis. However, recent simulations [140], show that the coherence of the generated supercontinuum is directly related to the soliton order N defined by:

$$N = \sqrt{0.283 \cdot \tau_p E_p \cdot \frac{\gamma}{|\beta_2|}} \quad (5.1)$$

where τ_p is the FWHM pulse duration of the input pulses, E_p the pulse energy of the pulses coupled into the highly-nonlinear fiber, γ the nonlinear coefficient of the fiber and β_2 the second order dispersion parameter of the fiber.

In particular, a soliton order $N < 10$ was predicted by simulations [140] to be sufficient for coherent broadening. For a given pulse energy and a given nonlinear fiber, this sets a lower limit in pulse duration to obtain a coherent SC. This was recently verified in the experimental results presented in [141]. However, a more thorough experimental study is still required to investigate this limit in the particular context of CEO detection. For example, the effect of the soliton order on the signal-to-noise ratio (SNR) of the detected CEO frequency has not yet been carefully studied. Other parameters such as a chirp of the input pulses, the length of the nonlinear fiber for different input peak powers, or temperature stabilization of the nonlinear fiber would also represent interesting points to investigate in more detail.

5.2.4 High-power frequency combs

Frequency combs with high average powers are attractive because an increase of the overall average power of the frequency comb, in combination with a high repetition rate, results in a higher power per comb tooth. This allows for higher SNR in spectroscopy experiments. Up-to-date, the highest average power demonstrated from a frequency comb is based on a fiber amplifier delivering 80 W [142].

Most efforts that were carried out in the past years to achieve frequency combs directly from DPSSLs were mostly focused on increasing the repetition rate to the GHz regime [143, 144]. Modelocked TDLs enable the highest average powers from any ultrafast oscillator, making them potentially interesting candidates for frequency comb applications.

However, prior to the work presented here, it was not clear whether pump-induced instabilities could potentially increase the noise level such that a stable frequency comb cannot be realized [137, 145]. TDLs are pumped by high-power diodes, which operate in a multimode transverse beam (the fiber-delivered pump beam typically has $M^2 > 100$). Furthermore, they require current drivers operating at several tens of amperes. Here, we investigate for the first time the carrier envelope phase properties of a modelocked TDL.

5.3 Carrier-envelope frequency of a modelocked thin-disk laser

5.3.1 Experimental Setup

The laser setup was described in Chapter 4, Paragraph 4.2.2. The laser delivers stable modelocked pulses up to an average power of 7 W. At this power level, the sech^2 shaped pulses are 142 fs. The laser operates at a repetition rate of 64 MHz, leading to a pulse energy of 0.1 μJ and a peak power of 0.7 MW. The pulses are close to the transform-limit of the spectrum with a time-bandwidth product of 0.34.

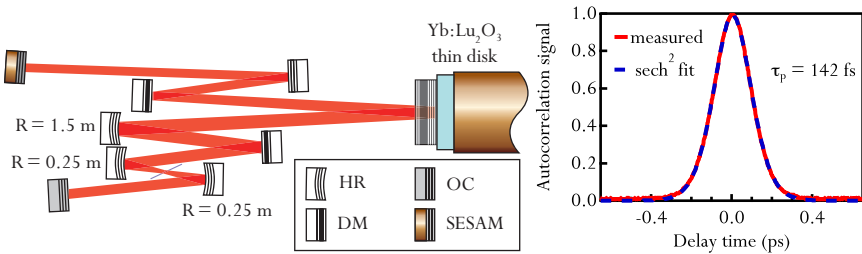


Figure 5.5: Left: Laser setup of the Yb:LuO laser used for the CEO frequency detection experiment. Right: Autocorrelation trace of the 142-fs long soliton pulses at the maximum available output average power of 7 W.

We generated a coherent SC in a 1-m long, highly nonlinear PCF using only 65 mW out of the available 7 W of our Yb:LuO TDL. The fiber used is a commercially available highly nonlinear PCF (NKT Photonics A/S, product NL-3.2-945) with a nonlinear parameter $\gamma = 23 \text{ W}^{-1}\text{km}^{-1}$,

and a zero dispersion wavelength at 945 nm. At the laser wavelength of 1034 nm, the fiber exhibits anomalous dispersion of $\approx -15.1 \text{ ps}^2/\text{km}$. Considering an estimated coupling efficiency of 50%, the corresponding soliton order launched into the nonlinear fiber is $N = 5.5$. According to numerical simulations [140], and recent experiments [141] a soliton order $N < 10$ is required for the generation of the coherent supercontinuum in this fiber.

5.3.2 Results

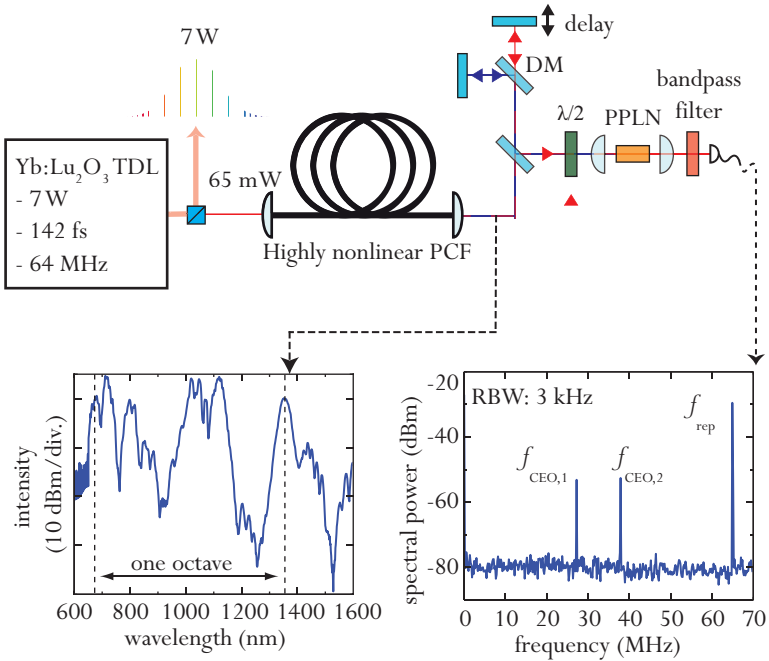


Figure 5.6: Top: Experimental setup with highly nonlinear PCF for SC generation and schematic of f -to- $2f$ interferometer used for f_{CEO} detection. Bottom, left: Measured spectral broadening after the PCF, right: Observed CEO frequency beats (RBW = 3 kHz).

The short pulses of our TDL enabled us to generate this coherent SC without the need for external pulse compression or amplification. The SC (Figure 5.6, bottom left) after the PCF covered more than an octave and

was launched into a standard f -to- $2f$ interferometer [123] for CEO beat detection. A schematic of the interferometer is shown on the right hand-side of Figure 5.6. At the input of the interferometer, a dichroic mirror (DM) separates the long- and short-wavelength part of the spectrum that will be used for the CEO beat detection. On one of the arms, a delay line enables temporal overlap of the pulses required to observe beating of the signals. After polarization adjustment, the long wavelength part of the spectrum is frequency-doubled in a 1-mm long PPLN crystal with a poling period of $13.8 \mu\text{m}$. The beat signal is then detected with a fast photodiode, after a bandpass filter that selects the desired spectral portion to be detected.

The detected CEO beats had a SNR of > 25 dB in a resolution bandwidth (RBW) of 3 kHz (Figure 5.6, bottom right) and > 30 dB in a RBW of 1 kHz. During the time of the experiment (approximately one hour) we did not observe significant frequency excursion or amplitude fluctuations of the beats. We believe that the achieved SNR is large enough for initial locking tests of the CEO beat, in particular given the high stability of the observed beats. Furthermore, significantly better SNR can be achieved by optimizing the laser performance. In particular, TDLs with shorter pulse durations, such as the ones described in Chapter 4 based on Yb:LuScO or Yb:ScYLO that deliver ≈ 100 fs pulses would be ideally suited to increase the SNR.

It is important to notice that the TDL used for this proof-of-principle experiment was built with standard optomechanics, and was not isolated in terms of external vibrations. Furthermore, the pump laser was operated at only 15% of its maximum optimum current. Therefore, we believe better performance is achievable by improving the mounting technique, boxing, and pump operation point of the oscillator. Furthermore, optimizing the CEO-beat detection scheme (fiber length, input peak power level, fiber design, shorter pulse duration, temperature stabilization of the highly nonlinear fiber, etc...) should also result in an improved SNR.

To investigate the influence of the pulse duration on the detected CEO beats, we increased the pulse duration to ≈ 172 fs according to the soliton formula (Formula (2.1)) by lowering the pump power and operating at 5.1 W of output power. We could still clearly detect the CEO

beats at this longer pulse duration, at the expense of a lower SNR (16 dB in 3 kHz RBW). As we discussed in the previous Paragraph, the maximum soliton order required to generate a coherent SC in a given nonlinear fiber sets a lower limit in terms of pulse duration of the source. For our system, this limit was calculated to be at a pulse duration of approximately 180 fs, which seems to be in accordance with our experiment. Further investigations will target to confirm this limit in pulse duration experimentally. In our experiment, further lengthening of the pulse duration was not possible without breaking into the Q-switched modelocking regime.

The CEO beat frequency was tunable by the pump current, with a slope of approximately 33 kHz/mA. This mechanism can be used for electronic stabilization of the CEO frequency to an external reference.

It is worth emphasizing that CEO detection was possible in spite of the strongly multimode pumping scheme of TDLs, usually associated with a high noise level. This seems to indicate that state-of-the-art high-power systems such as the one presented in [30] or the one presented in [14] and in Chapter 6, would already be suitable to achieve >100-W-level stabilized frequency combs. Taking into account the pulse duration of such state-of-the-art high-power systems, an external temporal pulse compression stage will be required to reach the necessary short pulse duration for CEO detection. Different pulse compression techniques will be discussed in Chapter 6. However, as we discussed in Chapter 4, we believe 100 W level sub-100 fs pulses will be feasible in the near future directly from a TDL, which will significantly simplify CEO detection.

5.3.3 Towards full stabilization of high-power thin-disk lasers

The necessary steps to fully stabilize a TDL are currently being carried out. In this goal, the Yb:ScYLO laser described in Chapter 4 delivering 100 fs pulses and 5 W of average power is a good candidate, and is currently being setup for this purpose.

In this goal, several critical points need further investigation. Current challenges in this direction include achieving a fast modulation of the high current driver sources used in TDLs. Another crucial point is to thoroughly investigate the amplitude and phase noise properties of TDLs. Although the

experiments demonstrated in this section indicate that this is not a limitation, this still needs to be confirmed at higher power levels, for example in the system presented in Chapter 6 with an additional compression stage.

Chapter 6 - Average power scaling of modelocked thin-disk lasers

Several issues have so far limited scaling of modelocked TDLs to average output powers in the kW range.

One challenge, which was already discussed in Chapter 2, is achieving fundamental transverse mode operation at sufficiently high average powers. Up-to-date, 500 W of average power have been demonstrated with a diffraction-limited beam quality from a single disk [25] based on the standard thin-disk gain material Yb:YAG. Large disks with excellent quality based on this material are commercially available. Therefore, for the results presented in this Chapter, we chose to use this well-established gain material. This enabled us to achieve sufficient power in fundamental-mode operation to perform the next step in power scaling of modelocked TDLs.

Another crucial issue for modelocking at high average power is that an excessive nonlinear phase shift due to SPM can destabilize the pulses in the soliton modelocking regime [34, 36]. In the past, the dominant source of unwanted SPM was caused by the nonlinearity of air. Here, we demonstrate a new approach to overcome this limitation in the context of modelocked TDLs. We operate the oscillator in a vacuum environment, therefore reducing the nonlinearity of the ambient environment by several orders of magnitude. In this way, high average powers and pulse energies can be achieved in simple oscillator geometries with a low number of passes through the gain medium and low outcoupling rates. Furthermore, only a small amount of dispersion is required even at very high intracavity pulse energies. With this approach, we were able to demonstrate a TDL with an average power of 275 W at a pulse duration of 580 fs using the well-established gain material Yb:YAG. The laser operates at a repetition rate of 16.3 MHz resulting in a pulse energy of 16.9 μ J and a peak power of 25.6 MW. To our knowledge, this is the highest average power ever demonstrated from a passively modelocked oscillator and represents an important step towards the kW level milestone.

This Chapter is organized as follows. In the first Paragraph, we will review different previously suggested methods to limit the unwanted effect of the nonlinearity of air in modelocked TDLs. In a second Paragraph, we will present the highest cw fundamental mode laser result that was obtained with this setup. In a third Paragraph, we will focus on the modelocking experiment that led to the demonstration of a modelocked oscillator with 275 W of average power. Finally, we will present a discussion and an outlook of the different possibilities opened by this result.

6.1 Harnessing intracavity nonlinearity

6.1.1 State-of-the-art: different suggested approaches

The different sources of nonlinearity in a typical TDL cavity have been discussed in Chapter 2. Historically, once the air in the resonator was identified as one of the most significant sources of SPM in the laser cavity, several approaches were suggested to overcome this limitation:

- Helium flooding

Helium has a nonlinear refractive index n_2 that is 8 times smaller than air [146]. Therefore, replacing the air in the cavity by helium enabled the demonstration of the $> 10\text{-}\mu\text{J}$ pulse energy milestone in 2008. In this result, 11 μJ were obtained at an average power of 44 W from a SESAM modelocked TDL based on Yb:YAG [41, 42]. The disk in this oscillator was used as a single-pass-gain folding mirror in the cavity, resulting in an intracavity pulse energy of $> 110 \mu\text{J}$. The required dispersion to generate the 791-fs pulses was, in this case, $-20\,000 \text{ fs}^2$.

- Multiple gain passes through the same disk

Another approach to lower the SPM in the cavity to reach higher pulse energy levels is to reduce the intracavity pulse energy by choosing a higher output coupler transmission. This has the additional advantage that the fluence on the SESAM and the thermal load on all intracavity components are reduced. Efficient laser operation with a higher output coupling transmission is only possible if the gain per cavity round trip is increased accordingly. In this approach, this is achieved by multiplying the number of

passes through the same gain disk, which results in an increased overall gain per roundtrip. This geometry, most commonly referred to as “active multi-pass cell” in a modelocked TDL has been introduced by Neuhaus et al. [45, 46]. In the first demonstration, the 13 passes through the gain medium allowed for an output coupling rate of 78% and an average output power of 78 W at a repetition rate of 2.9 MHz. This corresponds to a pulse energy of 26 μJ . In the meantime, this result has been improved to an average power of 145 W with a pulse energy of 41 μJ using a 72% output coupling transmission [147]. In the latest result, the intracavity pulse energy was below 60 μJ and operation in air was possible with a total GDD of $-236\,000\text{ fs}^2$. In contrast, the result mentioned above (11- μJ pulses in helium, corresponding to an intracavity pulse energy of 113 μJ) could be realized with more than 10 times less negative GDD ($-20\,000\text{ fs}^2$).

In addition, 13 passes through the thin disk significantly increase the demands on the disk quality, since the cavity stability zones shrink significantly with the number of passes (see Figure 2.12). Another potential disadvantage is the reduced Q -factor of the cavity, resulting in a higher intrinsic noise level for the resulting laser. Furthermore, Formula (2.2) indicates that a larger gain per roundtrip results in longer minimum achievable pulse durations. In fact, in the result presented in [147], the pulse duration was 1.1 ps. These picosecond pulse durations are not a problem for example for micromachining applications, where pulse energy is the main priority. In the case of the scientific applications aimed in this thesis, shorter pulse durations are beneficial - in particular because it simplifies further pulse compression schemes (see Chapter 7).

- Multiple gain passes through different disks

The combination of several laser heads in one cavity has already been demonstrated using several Yb:YAG disks in one resonator [17], but not in the context of modelocked TDLs. However, it is not straightforward to achieve fundamental mode operation as each disk can show a different thermal lensing behavior.

- Vacuum environment

Operating the oscillator at a medium vacuum level by placing it in a vacuum chamber allows to reduce the nonlinearity of the ambient environment by several orders of magnitude, since the nonlinear refractive index n_2 parameter varies linearly with air pressure [148]. This is the approach we will present in this Chapter, which enabled reaching a record-high average power of 275 W.

6.1.2 Oscillator in vacuum

In addition to a minimal nonlinear phase shift at very high intracavity peak power levels, the advantages of operating the oscillator in vacuum are many-fold:

- Fine adjustment of the air pressure inside the cavity enables one to tune the nonlinear phase shift and minimize the pulse duration at a given output power. This eliminates the need for a moving Brewster plate in the cavity that can introduce aberrations and small losses.
- The low amount of nonlinearities allows one to operate in simple oscillator geometries with low gain per cavity round-trip (one or two passes on the disk used as a folding mirror in the cavity). This relaxes the constraints on the disk thermal lensing, as we described in the previous Paragraph.
- Small amounts of negative GDD are required to compensate for the small resulting nonlinear phase shifts even at high intracavity peak powers. This results in lower parasitic losses and thermal effects that are commonly observed in the dispersive mirrors.
- Turbulence of air and related pointing instabilities are minimized.
- Operating in a vacuum environment allows keeping the oscillator optics clean, which is critical at high intracavity powers.
- In addition to the above-mentioned points, developing robust vacuum oscillator technology will facilitate future intracavity HHG experiments, for which operation in vacuum is essential to avoid UV-light absorption by air. Furthermore, for other nonlinear experiments, one could consider flooding the chamber with other gases.

On the other hand, heat convection due to air is nearly completely eliminated by operating the oscillator in vacuum. In our experiment, we observed increased thermal effects in critical optics such as the dispersive mirrors when the oscillator was operated in vacuum. Nevertheless, using thermally improved mirrors and/or actively cooling these critical elements in the cavity (in the same way the disk or the SESAM are cooled) can solve these issues.

6.2 High-power fundamental mode cavity

The gain element used for the experiments described in this Chapter is a commercial Yb:YAG thin disk glued on a water-cooled diamond heatsink (TRUMPF GmbH). The disk is $\approx 100 \mu\text{m}$ thick and the exact doping concentration was not provided. The thin-disk head was arranged for 24 pump passes through the disk and a pump spot diameter of 4.7 mm. The pump diode used for this experiment can deliver up to 1.2 kW of power at a central wavelength of 940 nm. In our experiment, we only used 70% of the available pump power ($\approx 850 \text{ W}$). In order to match the 940 nm absorption line of Yb:YAG at this operation point, we adjusted the temperature of the diode with an external chiller.

The measurement of the thermal lensing of this disk with a polarized Michelson interferometer was already presented in Chapter 2 (Figure 2.6, blue line) and showed no significant thermal lensing over the whole pump power range used throughout the experiment (approximately 850 W of pump power corresponding to a pump power density of $5.1 \text{ kW}/\text{cm}^2$).

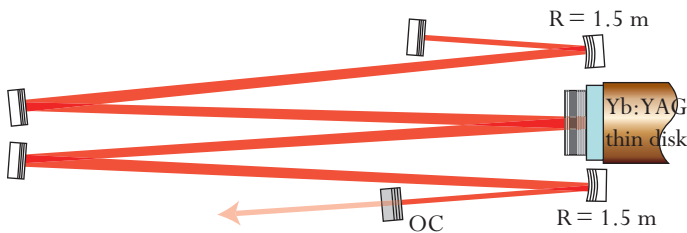


Figure 6.1: Schematic setup of the fundamental transverse mode cavity used for the high-power fundamental-mode experiment.

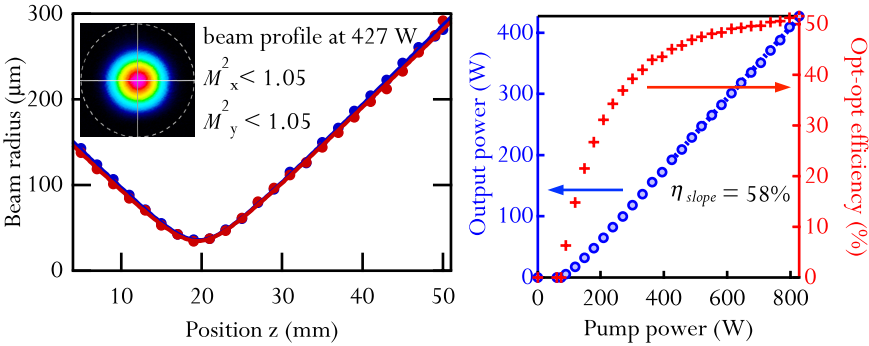


Figure 6.2: Cw fundamental mode results Left: M^2 measurement and beam profile of the beam at the maximum power of 427 W. Right: Output power and optical-to-optical efficiency of the laser in cw operation.

The outstanding thermal properties of this disk allowed for robust single mode operation up to 427 W of power in cw operation without any readjustment of the resonator length [26, 149]. A schematic of the laser cavity is presented in Figure 6.1 and the obtained experimental results in fundamental mode cw operation are shown in Figure 6.2. For this experiment, we used an optimum outcoupling rate for best slope efficiency of 6.4%.

6.3 Femtosecond modelocked oscillator with 275 W of average power

6.3.1 Experimental Setup

For the modelocking experiment, we used another disk with the same characteristics that delivered comparable performance than the disk described in the previous Paragraph. We used the same pump arrangement, but the layout of the laser cavity was slightly modified (Figure 6.3). Two expanding telescopes were added in the SESAM arm and the OC arm to expand the beam sizes on both components.

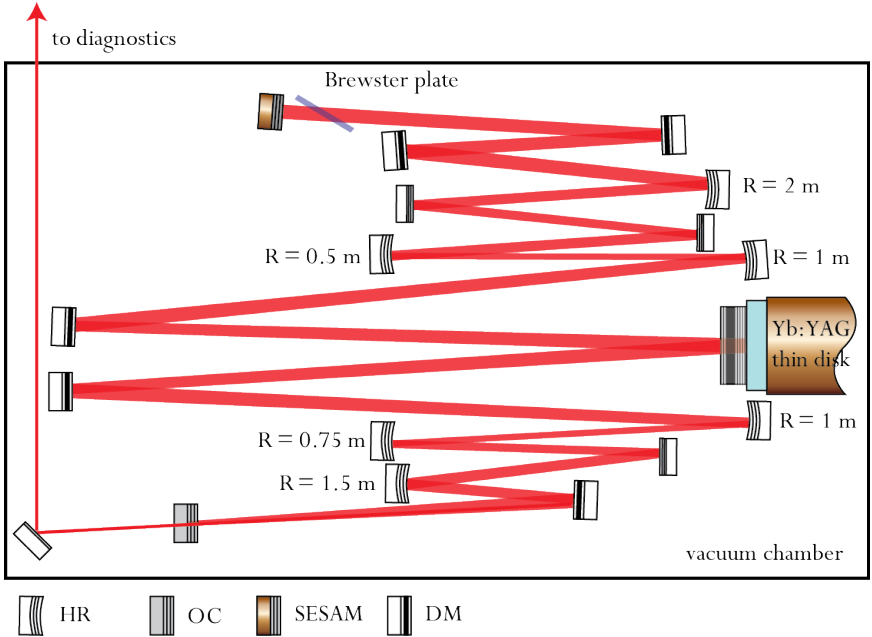


Figure 6.3: Schematic setup of the 16.3 MHz pulse repetition rate fundamental transverse mode cavity used for the high-power modelocking experiment.

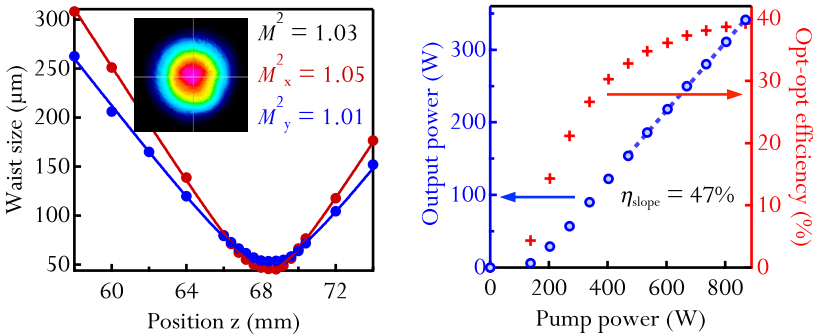


Figure 6.4: cw fundamental transverse-mode operation using the same output coupler as for the modelocking experiment and using only highly reflective mirrors as cavity mirrors and without polarization control of the laser. Left: M^2 measurement at the maximum power of 340 W. Inset: Picture of the laser mode at the maximum CW output power. Right: Output power and optical-to-optical efficiency.

We used a higher outcoupling rate of 11.4%, to lower the intracavity power. A lower intracavity power simplifies the cavity design because it allows for smaller spot sizes on the SESAM (in our experiment, the laser beam on the SESAM had a radius of ≈ 1.23 mm) and reduces thermal distortions from intracavity elements such as dispersive mirrors. The increased output coupling resulted in a slightly reduced slope and optical-to-optical efficiency. Nevertheless, we could obtain up to 340 W of cw power at an optical-to-optical efficiency of 39.2% with a diffraction-limited beam ($M^2 < 1.05$) (Figure 6.4).

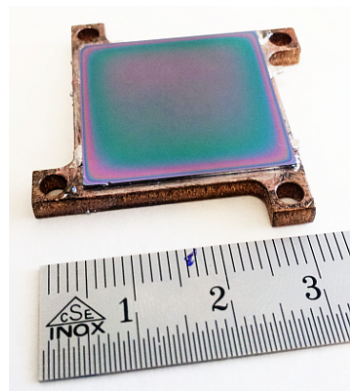
In order to obtain soliton modelocking, we introduced a set of five dispersive mirrors in the cavity that introduced approximately $-8'100$ fs² of negative GDD per roundtrip. A fused silica plate with a thickness of 700 μ m was inserted at Brewster's angle to select the p -polarization. It was introduced at a fixed position in the cavity where the beam had a large radius of ≈ 1.3 mm. This controls the laser polarization with minimal SPM. Fine control of the total SPM was achieved by changing the pressure in the vacuum chamber by introducing small amounts of nitrogen.

6.3.2 SESAM design

The SESAM used in this experiment (Figure 6.5) was designed for high damage threshold and high-power modelocking following the guidelines presented in reference [38] and in Chapter 3. Special attention was paid during fabrication to obtain a large homogeneous sample for future spot size scaling.

It consists of a distributed Bragg reflector and three 10-nm InGaAs QWs as absorbers embedded in AlAs in an antiresonant configuration. A dielectric topcoating that consists of 3 quarter-wave pairs of SiO₂/Si₃N₄ was deposited by PECVD. We measured the nonlinear reflectivity and recovery dynamics of this SESAM using the measurement setup and procedure described in Chapter 3. The measurements yielded a saturation fluence $F_{\text{sat}} = 140$ μ J/cm², a modulation depth $\Delta R = 0.95$ % and nonsaturable losses $\Delta R_{\text{ns}} = 0.1$ %. Furthermore, we measured a recovery time $\tau_{1/e} = 67$ ps. The SESAM in the cavity was actively stabilized to 15°C by cooling the copper heatsink using a Peltier element.

Figure 6.5: Picture of the large scale SESAM used for the experiment. The color variation is due to small differences in the PECVD topcoating and is accentuated at the edges of the sample.



6.3.3 Results

For the modelocking experiment presented here, the vacuum chamber (Figure 6.6) was operated at a constant pressure of 0.5 mbar, which was the lowest value that could be obtained in our setup and with the available pump.

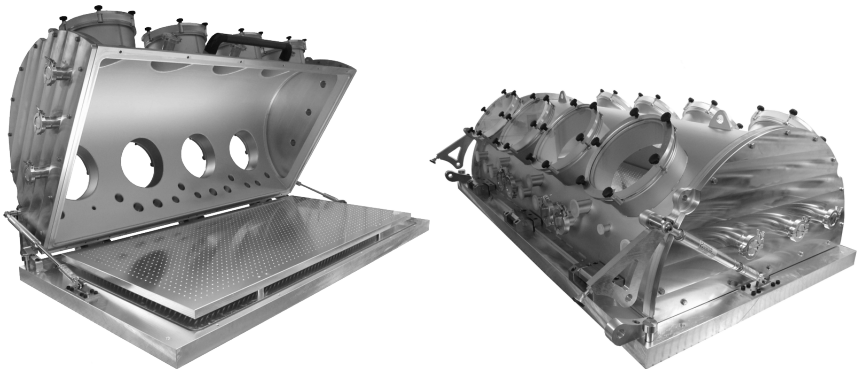


Figure 6.6: Picture of the vacuum chamber in which the modelocked laser was built.

Stable cw modelocking was obtained for average powers ranging from 135 W to 275 W. At the highest power level, the optical-to-optical efficiency decreased (by approximately 1%), but no modelocking instabilities were observed. In order to avoid possible damage of the thin disk, the pump power was not further increased. At the maximum power

of 275 W, the pulse duration was measured to be 583 fs (Figure 6.7). The optical-to-optical efficiency was 32.4%, corresponding to an incident pump power of 839 W. The pulses had a time bandwidth product of 0.329 (ideal sech^2 0.315), determined with the measured spectral bandwidth of 2 nm (Figure 6.7). The repetition rate of the pulses was 16.3 MHz, resulting in a pulse energy of 16.9 μJ . The corresponding peak power of the pulses is 25.6 MW. Operation with a single pulse circulating in the cavity was confirmed using a fast photodiode (25 GHz) and a sampling oscilloscope. Furthermore, the delay of the autocorrelator (80 ps) was scanned in search for cross-correlations of potential parasitic pulses with the main pulse. The beam at the maximum modelocked average power level was nearly diffraction limited with an $M^2 < 1.05$.

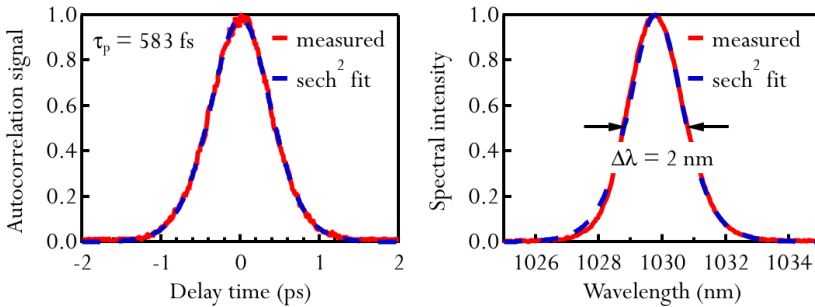


Figure 6.7: Left: Autocorrelation trace of the pulses at the maximum power of 275 W. Right: Optical spectrum of the pulses.

6.4 Discussion

6.4.1 Sources of nonlinearity

Inside the oscillator, the circulating pulses had an energy of 146 μJ , and a peak power of 220 MW. In contrast to previous high-power modelocked TDLs, the nonlinearity of the ambient environment was not the main contribution to the total SPM phase shift required for soliton modelocking. Assuming soliton pulses, the dispersion introduced in our cavity compensates for a nonlinear phase shift of approximately 75 mrad at the maximum power and for the obtained pulse duration. The atmosphere in

the cavity only contributes ≈ 8 mrad to this total phase shift. This value was calculated assuming a linear behavior of the nonlinear refractive index of air with the pressure in the vacuum chamber [146, 148]. The Brewster plate accounts for ≈ 17 mrad and the thin disk for ≈ 3 mrad. The remaining phase shift (≈ 47 mrad) seems to originate from nonlinearities due the high intensities on the different cavity mirrors. In our current layout, some of the dielectric mirrors used in the cavity withstand intensities > 50 GW/cm². At these high peak intensities, even a small penetration depth can lead to a significant phase shift. However, in order to precisely evaluate the contribution of each mirror to the total phase shift, the exact structure and material composition of these commercial mirrors needs to be precisely known, which is currently being investigated.

In spite of these very high intracavity intensities, no damage was observed on the SESAM. The main limitation to higher average powers in our current configuration was thermal effects and even damage that occurred in the dispersive mirrors. Improved dispersive mirror designs with better thermal properties will allow for higher average power in the future.

6.4.2 Mode degeneracies and beam quality degradation

As we pointed out in Chapter 2, beam degradation in standard TDLs originates, in most cases, from residual thermal distortions in the thin gain medium. In the case presented here, the disk was of sufficiently high quality for this not to represent the main limitation.

Nevertheless, at the high intracavity powers considered in this experiment, special attention has to be paid to any other possible source of beam degradation. In our experiment, we observed strong beam degradation and unusual modelocking instabilities in some specific cavity configurations. Small changes in the cavity were usually enough to solve these issues. We believe this originated in resonant coupling effects between the fundamental mode and higher order transverse modes. In fact, some cavity designs operated close to transverse mode degeneracies can have a strong tendency to couple power from the lowest fundamental transverse mode to high order modes [150-152]. An important practical consequence of this coupling is that small thermal effects can result in a

significant degradation of the beam quality and can also destabilize fundamental modelocked operation. These observations triggered the need for a simulation tool to avoid such “dangerous” cavities. In the following Paragraph, we will briefly explain the phenomena of resonant coupling of higher order modes to the fundamental transverse mode and the new tool implemented in our cavity design software to identify the cavities that can lead to such problems.

- Resonant coupling to high order modes

Most Formulas used in the following Paragraph can be found in [153]. The normalized expression of the electric field for a Gaussian beam as a function of the distance z from the waist is given by:

$$E(x, y, z) = \sqrt{\frac{2}{\pi}} \frac{q_0}{\omega_0 q(z)} \cdot \exp\left(-i \frac{(x^2 + y^2)}{2q(z)} - ikz\right) \quad (6.1)$$

where ω_0 is the waist radius and $q(z)$ the complex radius of curvature parameter. $q(z)$ is related to most common beam parameters by:

$$\frac{1}{q(z)} = \frac{1}{R(z)} - i \frac{\lambda}{\pi \omega^2(z)} \quad (6.2)$$

where $\omega(z)$ is the $1/e^2$ radius of the Gaussian beam and $R(z)$ its radius of curvature at a position z from the waist. The expression of the electric field can then be written:

$$E(x, y, z) = \sqrt{\frac{2}{\pi}} \frac{\exp\left(-ikz + i\phi_{\text{Gouy}}(z)\right)}{\omega(z)} \cdot \exp\left(\frac{-(x^2 + y^2)}{\omega^2(z)} - ik \frac{(x^2 + y^2)}{R(z)}\right) \quad (6.3)$$

The term ϕ_{Gouy} in this expression represents a small axial phase shift that occurs to a Gaussian beam when propagating through a waist, and that differentiates it from a spherical wave.

All relevant parameters in this expression can be related to waist spot size ω_0 and Rayleigh range z_R by:

$$\omega(z) = \omega_0 \sqrt{1 + \left(\frac{z}{z_R}\right)^2} \quad (6.4)$$

$$R(z) = z + \frac{z_R^2}{z} \quad (6.5)$$

$$\phi_{\text{Gouy}}(z) = \tan^{-1} \left(\frac{z}{z_R} \right) \quad (6.6)$$

The ABCD-law for the q -parameter allows propagating a Gaussian beam through ABCD type optics. This applies for the fundamental mode of a laser resonator, for example. For higher order transverse modes that can circulate in a resonator, the general expression of the electric field depends on the problem symmetry. In practice, a rectangular symmetry is most commonly used since in most cases some selection is present for the x - and y -axis. In this case, the general expression of the electric field is best described by the Hermite-Gauss modes, where a given higher transverse mode is characterized by two integer indices m and n . It can be shown that different transverse modes experience different Gouy phases and their expression is given by:

$$\phi_{\text{Gouy}}^{m,n} = (m+n+1) \cdot \phi_{\text{Gouy}}^{0,0} \quad (6.7)$$

An important consequence of this is that it is not necessary to propagate a given high-order mode to obtain its Gouy phase shift, since the value can be obtained from the one of the fundamental mode. It is worth noting that the higher the order of the mode, the stronger the axial phase shift. The presence of a non-zero Gouy phase shift causes the different transverse modes of the cavity to have different resonant frequencies ν , according to

$$\nu_{q_{\text{axial}},m,n} = \frac{c}{2L} \left[q_{\text{axial}} + \frac{\phi_{\text{Gouy}}^{m,n}}{2\pi} \right] \quad (6.8)$$

where L is the length of the resonator, q is the axial mode index. In this Formula, we neglected the small phase shift caused by frequency pulling due to the asymmetric gain and losses in the resonator. Formula (6.8) indicates that axial modes associated with a pair of transverse spatial modes become degenerate in frequency when their round-trip Gouy phases are the same (modulo 2π). If the fundamental transverse mode of the cavity is nearly degenerate with a higher-order transverse mode, and if there is a finite coupling between these modes due to a non-ideality in the cavity

(such as a thermal lens having a non-ideal phase profile), power can be resonantly coupled into the higher-order mode, leading to a reduction in beam quality.

In practice, a criterion can be added to cavity design software by computing the Gouy phase of the fundamental mode and deducing its value for higher order modes. A figure of merit can then be established to be in a “safe” distance from overlap with a certain set of higher order modes. However, the existence of an overlap does not indicate how strong the coupling would be between these modes or even if it will occur. For this, an exact determination of the modal coupling coefficients for each intracavity element would be required. This is a complex task, and the additional advantage would be small.

In cases where thermal lensing effects occur in the cavity, a single figure of merit for the “cold cavity” might be insufficient. We will treat this problem in the next Paragraph.

- Effect of thermal lensing

If there is a source of laser-induced thermal lensing in a laser cavity, this picture is slightly more complicated. The resonance frequencies of the different transverse modes now vary with the intracavity power. Therefore, modal coupling effects can become severe at a given intracavity power. In order to take this effect into account, it is necessary to determine the influence of the different sources of thermal lensing on the fundamental mode of the laser resonator, and subsequently the effect on the Gouy phases of the different transverse modes. Therefore, it is also necessary to correctly model the temperature distribution caused by a Gaussian beam, and the resulting lens. Numerous models have been used to evaluate the thermal lens resulting from an incident Gaussian beam taking into account the thermo-optic effect and the physical deformation of the mirror [154]. We use the simplified model of Winkler et al. where the change of a mirror with power is described as a linear variation of sagitta s due to the optical path length difference generated between the center of the Gaussian beam versus its wings [155]. Sagitta is related to the beam waist incident on the mirror and the radius of curvature of the mirror by:

$$s = \frac{\omega^2}{2R} \quad (6.9)$$

Therefore, the resulting change of the beam parameters at a given mirror can be calculated using the rate of this change (ds/dP).

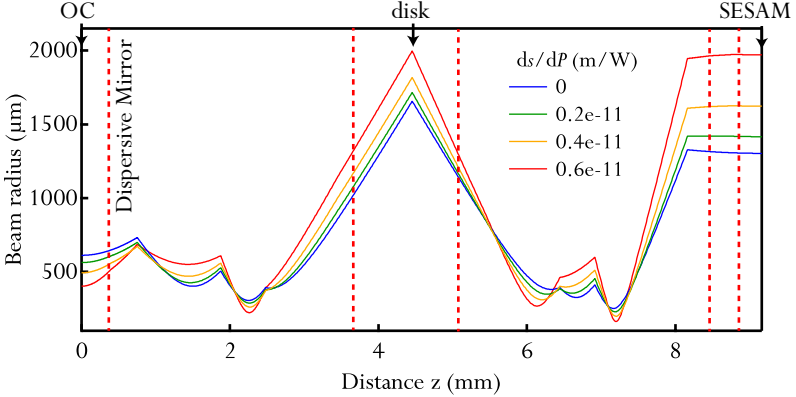


Figure 6.8: Influence of thermal lensing of different cavity elements on the beam radius of the fundamental mode cavity used for 275 W modelocked TDL.

We included these thermal effects in our simulation tool. In Figure 6.8, we illustrate the influence of thermal lensing of some cavity components on the fundamental mode resonator used for the 275 W modelocked TDL described in this Chapter. We applied a thermal lensing factor ds/dP at the exact positions in the cavity where 5 dispersive mirrors were introduced in the experiment (dashed red lines). The ds/dP factors applied were chosen for illustrating possible resonant coupling effects. The largest value chosen here ($ds/dP = 0.6 \cdot 10^{-11}$ m/W) is unrealistic given the resulting large spot size change, which would have been observable on a standard camera at the output of the laser. The values presented here are meant as an illustration and, the exact values remains to be determined empirically for each type of mirror.

In Figure 6.9, we illustrated the Gouy phase undergone during propagation in this cavity by different transverse modes verifying $m+n=p$, p being an integer < 7 .

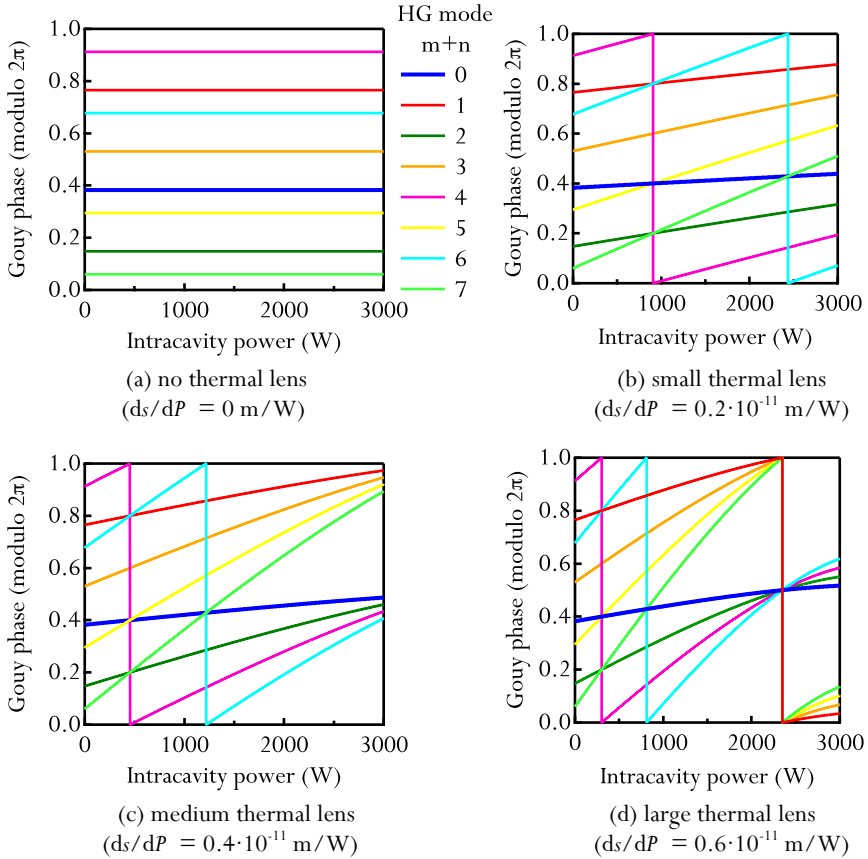


Figure 6.9: Influence of thermal lens on the Gouy phase for different transverse modes.

In Figure 6.9a, where no elements with thermal lensing are introduced in the cavity, the Gouy phases of the different transverse modes are well separated, and show naturally no dependence on the intracavity power. In Figure 6.9b, we apply a non-zero ds/dP at the 5 positions in the cavity where dispersive mirrors were introduced for the modelocked experiment (Figure 6.8, red dashed lines). The Gouy phases of different transverse modes have different slopes and crossing can occur already at a given intracavity power. We are interested in crossings with the fundamental mode ($m+n=0$, blue). For example, in this case, modes with

$m+n=7$ could potentially couple to the fundamental mode at an intracavity power of ≈ 2.5 kW. Possible coupling becomes dramatical for example in Figure 6.9d, where multiple modes intersect with the fundamental mode at an average power of 2.5 kW. At this point it is somehow important to stress that this does not necessarily mean that resonant coupling occurs, but gives a clear indication that it is more likely to happen.

- Discussion

Although the newly developed tool gives us a powerful instrument to evaluate the “quality” of a certain cavity for kW intracavity operation, several points still need to be investigated:

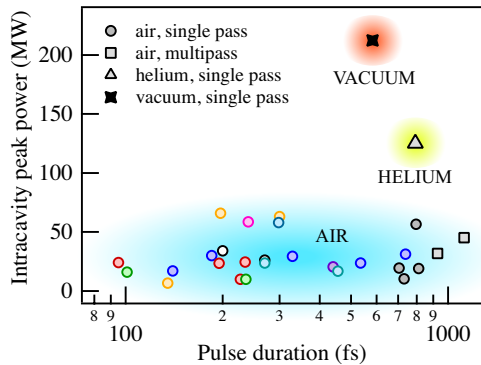
- Until now, the exact value of ds/dP remains an unknown parameter. This parameter is difficult to calculate without precise knowledge of the structure and material composition of the commercial mirrors used in our setup. In practice, an experimental determination of this parameter is crucial, which is currently being investigated.
- A figure of merit for determining how “dangerous” a certain cavity design is still needs to be defined. In order to do this, a careful experimental study needs to be made to evaluate how to characterize this coupling for such lasers.
- A more precise determination of the modes that need to be taken into account in search of Gouy-phase crossings (maximum p) is necessary by taking into account different apertures present in the laser cavity.
- A useful feature for cavity design would be to determine where in the laser cavity and how large would an aperture need to be to act as an efficient filter for the high-order modes, when a cavity is identified as having potential resonant coupling issues.
- Measuring and taking into account damage threshold of cavity optics would be an interesting feature to add to the software. In fact this could be useful additional information to know where to place “sensitive” optical elements in the laser cavity.

6.5 Conclusion and outlook

In this Chapter, we presented a femtosecond Yb:YAG TDL with 275 W of average power and 583 fs pulse duration. A large-scale SESAM with high damage threshold, which was especially designed for this experiment, was used for starting and stabilizing soliton modelocking. To the best of our knowledge, this is the highest average power obtained from a passively modelocked oscillator. The laser performance combines femtosecond pulses, high pulse energy (16.9 μJ) and record-high average power.

In order to reach this performance, the oscillator was operated in a vacuum environment. This allowed reducing the nonlinearity of the ambient environment by several orders of magnitude, enabling soliton modelocking at several hundreds of MW of intracavity peak power (Figure 6.10) with small nonlinear phase shifts and small amounts of dispersion. This approach represents a new approach that opens the door to power scaling of ultrafast oscillators to the kW range.

Figure 6.10: Intracavity peak power of modelocked TDLs demonstrated up-to-date. The result presented in this Chapter enabled operation of the oscillator at record high intracavity peak powers >200 MW and opens the door to future kW-level oscillators.



The main limitation to higher average powers was, in our experiment, thermal effects and even thermal damage observed on the dispersive mirrors. However, simulation tools were improved to consider beam degradation due to these effects and improved cavity design optimization guidelines are currently being developed in this goal.

Further average power scaling will require larger spot sizes on the disk and on the SESAM and improving the thermal properties of the dispersive

mirrors. In particular, dispersive mirror designs with improved substrates and higher damage threshold material composition for better heat removal are currently being investigated.

With the suggested improvements, we also expect to reach pulse energies in the 100 μJ range in the near future by increasing the length of the resonator using a Herriott-type passive multi-pass cell [41, 156].

Chapter 7 - Pulse compression of modelocked thin-disk lasers

In the previous chapters of this thesis, we saw that modelocked TDLs operate with output pulse energies up to tens of μJ and peak powers up to tens of MW. The systems with the highest output peak powers typically operate with pulse durations of >500 fs. Although the performance of such oscillators is moving in the direction of combining high peak powers (several tens of MWs) and short pulses (sub-100 fs), currently available sources do not reach this target yet. Therefore, numerous techniques have been investigated in the past years to efficiently reduce the pulse duration of state-of-the-art high-energy TDLs. Such techniques include spectral broadening using SPM in standard PCF fibers [71, 157], in fiber amplifiers [72, 73] and in HC-PCFs [74].

Temporal pulse compression in this range of pulse energies and peak powers is challenging because it lies in between the capabilities of two well-established technologies:

- On the one hand, typical TDLs operate at the damage limits of standard silica-based PCFs. The output pulse energies result in pulse fluences close to typical surface and bulk damage thresholds of silica. Using larger mode area (LMA) microstructured PCFs relaxes the pulse energy limits for damage, but the resulting weak guiding leads to high bending sensitivity and losses, which again limits the practical usability such fibers. In addition, the critical peak power for self-focusing in silica ultimately limits usable peak power. Threshold values in literature vary, but typical peak power threshold values are in the order of ≈ 4 MW [158].
- On the other hand, current state-of-the-art TDLs have insufficient peak powers for compression using standard techniques typically employed for Ti:Sapphire systems, such as filamentation in capillaries [159].

Previously, pulse compression of a SESAM modelocked high-power TDL was demonstrated using a short passive LMA fiber reaching 32 W and 24 fs pulses [71, 157]. In this experiment, the 760-fs long pulses were compressed by a factor of thirty and the peak power was increased by a factor of ten with an efficiency of 50%. This method enabled initial strong-field physics experiments driven directly at the multi-megahertz repetition rate of the femtosecond oscillator [6]. However, this passive compression system suffered from severe limitations. Damage in the 200- μm^2 LMA fiber limited the maximum achievable compressed pulse energy to less than 1 μJ , and it appears difficult to compress substantially higher pulse energies with standard microstructured fibers with larger mode areas because the weak guiding results in high bending sensitivity and losses.

For compression of medium power thin-disk oscillators, the use of active LMA rod-type fibers that also provides amplification represents an interesting approach. In this case, the bending sensitivity is reduced by surrounding the fiber with a glass rod, therefore allowing for stable single-mode operation with much larger mode sizes. Typically, commercially available rod-type fiber amplifiers have fundamental mode areas up to 4500 μm^2 , which is larger than most standard fiber technologies. Furthermore, these fibers are well suited for polarization-maintaining (PM) operation even at high peak power levels using stress-induced birefringence. Previously, pulse compression of medium power level oscillators using these rod-type fiber amplifiers has been demonstrated in different setups where MW peak powers at MHz repetition rates were achieved [73].

In the first Paragraph of this Chapter, we present two compression setups for a TDL oscillator based on two rod-type fiber amplifiers. In both cases, the high-power provided by the modelocked TDL was sufficient to directly saturate the single-pass amplifiers without the need for additional preamplifier stages, leading to relatively simple compression stages. In the first system, we used a 55-cm long rod with a core area of 2200 μm^2 , and achieved 55 W of compressed average power in 98-fs pulses, reaching pulse energy of 5.2 μJ at 10.6 MHz and a peak power of 32.7 MW. In a second stretcher-free system, a 36-cm rod-type fiber amplifier with a larger core area of 4500 μm^2 was used. With this setup, 34 W of average

power were demonstrated with 65-fs pulses, reaching a similar peak power of 32 MW. Although good performance was reached with both systems, they are ultimately also limited by self-focusing and damage in the silica-core [72]. We will discuss the performance and scaling limitations of these systems, in particular concerning damage and self-focusing.

For compression of state-of-the-art modelocked TDLs, gas-filled HC-PCFs appear to be an excellent alternative. They combine high self-focusing limits and damage thresholds with the possibility to tune the nonlinearity by varying the pressure and the composition of the used gas [160]. In particular, Kagome-type HC-PCFs exhibit low losses, very large transmission bandwidths and even higher damage thresholds than other HC-PCF technologies [10, 161, 162] due to the very low overlap between the propagating mode and the surrounding silica structure. During the time frame of this thesis, we performed the first proof-of-principle experiments using such fibers for pulse compression of modelocked TDLs. In the second Paragraph of this Chapter, we will present pulse compression of an Yb:YAG TDL that delivered a pulse duration of 860 fs and a pulse energy of 1.9 μJ down to sub-50 fs with an efficiency of 56%, using a Xenon-filled Kagome-type HC-PCF.

We will conclude this Chapter with a summary of the techniques studied here and an outlook towards pulse compression of high-power state-of-the-art thin-disk lasers to the 100 MW regime.

7.1 Rod-type fiber amplifier compression setup

7.1.1 Seed laser used for both experimental setups

The seed laser used for both amplifier systems consists of a standard Yb:YAG SESAM modelocked TDL similar to the one described in Chapter 3 for SESAM characterization. It delivers 16 W of average output power at a repetition rate of 10.6 MHz and at a central wavelength of 1030 nm. This corresponds to a pulse energy of 1.5 μJ in 1-ps-long pulses.

The average power obtained from this seed laser is sufficient to directly saturate the rod amplifiers used in both setups without the need for pre-amplifier stages. Therefore, the resulting compression and amplification setup is relatively simple. Furthermore, high average powers

at a low overall amplifier gain can be achieved, which is beneficial for low parasitic nonlinear effects and to achieve clean spectral broadening.

7.1.2 First amplifier system: 55-cm rod

- Experimental setup

We used the TDL described above to seed a 55-cm long PM Yb-doped rod-type LMA fiber amplifier (DC-200/70-PM-Yb-ROD, *NKT Photonics*). The rod was cleaved at 5 degrees at the input end to avoid parasitic lasing and had an uncleaved 8-mm-long end-cap on the output side. The rod core had a diameter of 70 μm and the pump cladding diameter was 200 μm . In order to avoid damage and self-focusing, the input pulses were stretched to 1.9 ps FWHM using two 1250 l/mm transmission gratings in a negative dispersion configuration. The pump used for amplification delivers 120 W at 976 nm and was used in a counter-propagating pumping configuration (Figure 7.1).

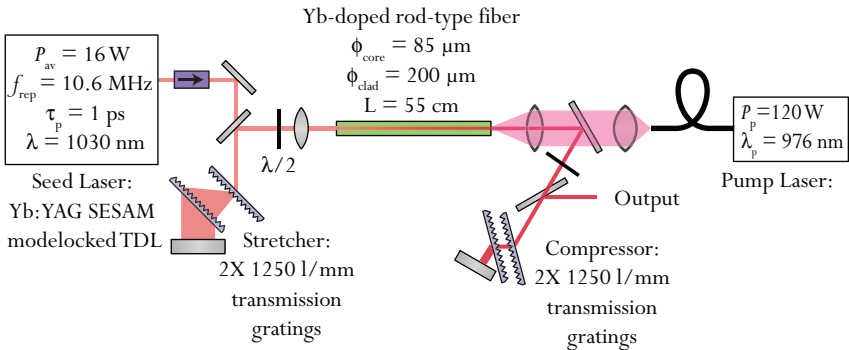


Figure 7.1: Experimental setup of the first rod-type fiber amplifier compression setup.

- Influence of the input chirp

In standard CPA systems, a positive chirp is usually preferred for stretching the input pulses. In this way, SPM broadening occurs over the entire length of the fiber, and the amount of accumulated SPM is easy to control since it is nearly linear. Negatively chirped pulses lead to an initial spectral and

temporal narrowing before the linear SPM broadening starts to occur. In Figure 7.2, we simulated the effect of the chirp of the input pulses on the spectral FWHM bandwidth over the length of the rod using a split-step Fourier nonlinear propagation software. In the case of negatively chirped pulses, the spectrum undergoes a minimum after a few centimeters of propagation through the fiber (Figure 7.2 bottom left, inset). The spectral narrowing that occurs in the first 10 cm of the rod is negligible. We chose to use negatively chirped pulses to simplify the grating stretcher since the two configurations result in similar compression factors (Figure 7.2 bottom, right). The total transmission through the 4-pass grating stretcher was measured to be 75% reducing the power launched into the fiber to 12 W.

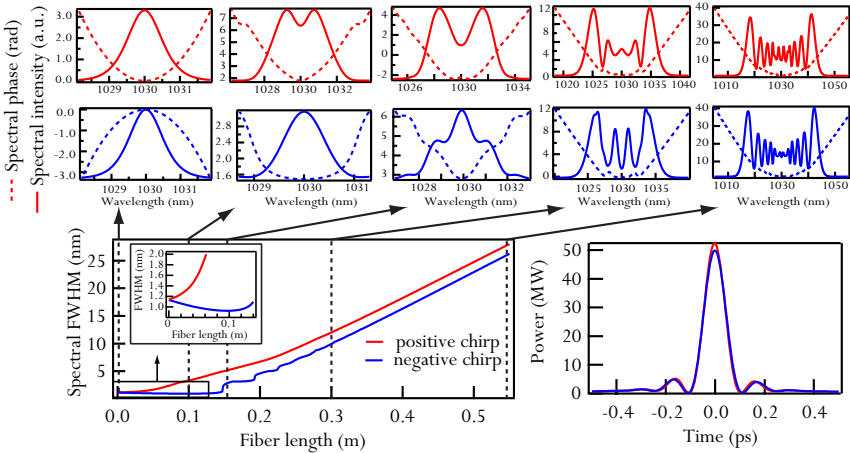


Figure 7.2: Simulation of the effect of the input sign of the chirp on the spectral broadening in the rod-type fiber amplifier. Bottom (left): Evolution of the spectral FWHM during propagation in the rod for negatively (blue) and positively (red) chirped pulses. Top (left to right): Evolution of the spectral intensity and the spectral phase during propagation in the fiber for positively and negatively chirped pulses. Bottom (right): resulting compressed power after 55 cm of propagation for negatively and positively chirped pulses. These simulations were performed with our home-programmed split-step Fourier propagation software.

- Results

The performance of the fiber amplifier is shown in Figure 7.3. We achieved 73 W of average output power, which corresponds to a pulse energy of 6.85 μJ . The output of the fiber amplifier was polarized with a polarization extinction ratio ($\text{PER} = -10\log(P_{\text{p-pol}}/P_{\text{s-pol}})$) of 15.8 dB. At this power level, an optical-to-optical efficiency $\eta_{\text{opt}} = P_{\text{out}}/(P_{\text{pump}} + P_{\text{seed}})$ of 52% was reached with a slope efficiency of 59%. Dispersion in such large core rod-type fibers is dominated by material dispersion. At the wavelength of our seed (1030 nm), the fiber exhibits ≈ -32 ps/km/nm of positive dispersion. Therefore, the pulses after amplification were slightly stretched to 2.7 ps. At the output of the rod, the peak power was 2.2 MW. At this peak power, no signs of self-focusing were observed and the beam quality stayed close to the diffraction limit with a measured $M^2 = 1.3$.

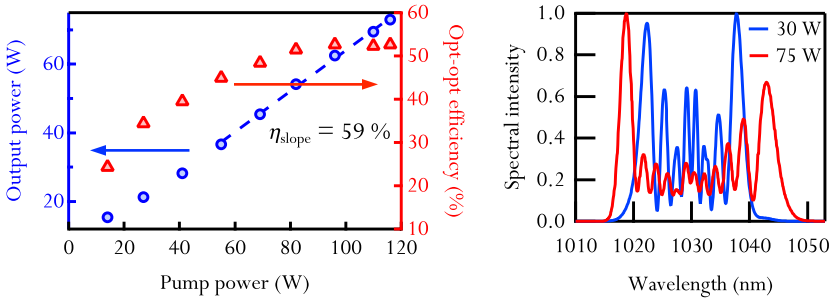


Figure 7.3: Left: Measured output power slope of the fiber amplifier. The maximum output power of 73 W corresponds to an optical-to-optical efficiency of 58%. Right: Observed spectral broadening with amplification.

The double-pass compression stage consists of two 1250 l/mm transmission gratings as used for the input stretcher. The transmission gratings are 100% fused silica and have low absorption, which is beneficial at the high power levels considered. The use of 1250 l/mm gratings enables a very compact compressor setup. The necessary dispersion was obtained with a grating distance of ≈ 3 mm. The total transmission through the 4-pass compressor was measured to be 75.4%. The resulting output

power after compression was 55 W, corresponding to a pulse energy of 5.2 μJ .

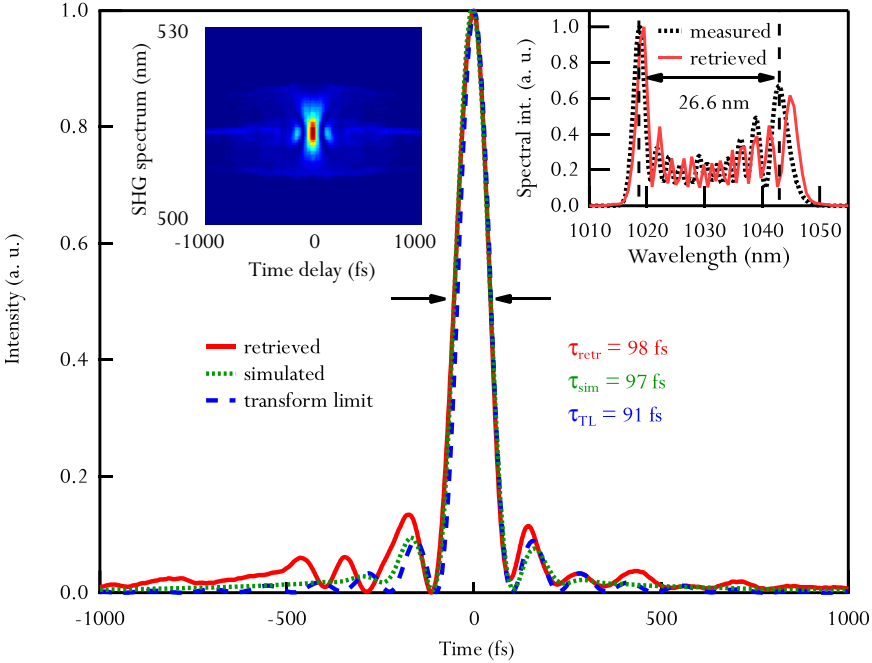


Figure 7.4: SHG-FROG characterization of the compressed pulses at the maximum compressed output power of 55 W (retrieved, simulated and transform-limit of the independently measured spectrum). Top left inset: Measured FROG trace. The FROG grid used was 256x256, and the retrieved error was $7 \cdot 10^{-3}$. Top right inset: measured spectrum at maximum output power with an independent optical spectrum analyzer and retrieved spectrum with FROG algorithm.

	Retrieved	Transform-limit	Simulated
Pulse FWHM	98 fs	91 fs	97 fs
Peak Power	32.7 MW	43.2 MW	37.9 MW
Energy in the main pulse	66%	81%	77%
Strehl ratio	0.76	-	0.87

Table 7.1: Different pulse characteristics of the retrieved, simulated and transform-limited pulses for the 55-cm rod-type fiber amplifier system.

The compressed pulses were characterized using second-harmonic generation frequency resolved optical gating (SHG-FROG) and the obtained results are presented in Figure 7.4. The retrieved FROG trace shows a FWHM pulse duration of 98 fs and a peak power of 32.7 MW (taking into account the energy distribution of the exact pulse shape as shown in Figure 7.4). The retrieved pulses are compared to the Fourier limit of the measured spectra after the amplifier and to simulations performed using a home-programmed split-step Fourier nonlinear propagation software. The values used for coupling efficiencies were typical values of $\eta_{\text{pump}} = 70\%$ and $\eta_{\text{seed}} = 80\%$. The simulated compression stage is done using only negative second order dispersion and optimizing for peak power. A comparison of the different parameters obtained is presented in Table 7.1.

As we can see in Figure 7.4, a residual picosecond background in the pulse limits the amount of energy in the main pulse to only 66%. This leads to a temporal Strehl ratio (corresponding to the ratio between the peak power obtained and the peak power of the transform-limited pulse of the measured spectrum) of 0.76. According to our simulations a Strehl ratio of 0.87 could be achieved with the measured spectrum considering only second-order dispersion for the compression. Part of the difference to the transform-limit is therefore probably due to the uncompensated higher order dispersion. We can see in the top-right inset of Figure 7.4, that the retrieved spectrum and the independently measured spectrum using an optical spectrum analyzer are in good agreement. The system was operated for around one hour before damage was observed. This made precise optimization of the gratings difficult at this power level. Nevertheless, the pulses obtained are in good agreement with the performed simulations and peak powers > 30 MW were obtained. On the other hand, two rods were damaged at this output power level, indicating that the system is operating close to its damage limit, and is not suitable for further amplification and/or compression to shorter pulses in the current layout. More details on the observed damage behavior will be discussed in a next Paragraph.

7.1.3 Second stretcher-free amplifier system: 36-cm rod

- Experimental setup

The second fiber amplifier system consisted of a shorter (36 cm) PM rod-type fiber with a larger core diameter of 100 μm and a resulting mode field area of 4500 μm^2 , which is two times larger than in the previous setup (DC-285/100-PM-Yb-ROD, *NKT Photonics*). The pump cladding is also larger with a diameter of 285 μm . The rod has two flat 8-mm end-caps at the input and output facets. Although the input end-cap is beneficial to prevent damage of the rod due to the seed laser pulses, the peak power levels at the input of the rod should not reach critical levels. At the output facet, the presence of an end-cap is crucial to avoid damage of the rod. The larger core size should limit the probability for bulk and surface damage of the rod by operating at lower intensities for a given peak power. Furthermore, the combination of the large core diameter and the shorter fiber length allows for enough spectral broadening to generate sub-100 fs pulses in a simpler setup where no stretching of the seed laser pulses is necessary. The setup is shown in Figure 7.5.

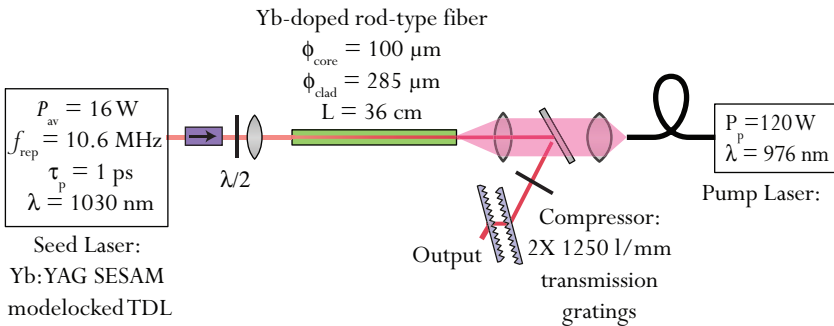


Figure 7.5: Second compression amplifier system: the 36-cm rod amplifier with a core area of 4500 μm^2 is seeded directly with the high-power TDL oscillator. The compressor stage consists of a single pass through two transmission gratings.

- Results

We launched the full seed laser power into the fiber (15 W). The performance of the fiber amplifier is shown in Figure 7.6. The full power of the pump was not used in order to avoid damage of the rod and/or self-focusing effects that were observed in the previous system. We therefore limited the output power to approximately 40 W, corresponding to 3 MW of peak power at the end of the rod. This value is to be compared to the reported approximate critical self-focusing peak power of 4 MW.

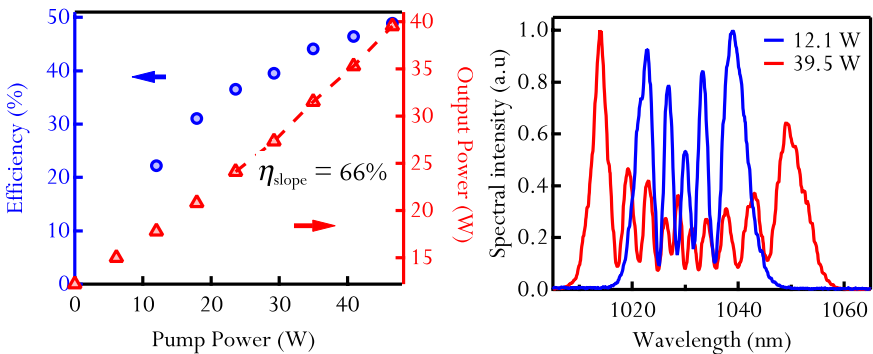


Figure 7.6: Left: Measured output power slope of the fiber amplifier. Right: Observed spectral broadening with no amplification (blue) and at full power (red). We also observe some spectral shaping, probably due to the limited gain bandwidth of the fiber.

At an output power of 39.5 W, the optical-to-optical efficiency reaches 48.8%. The amplified beam was close to the diffraction-limit with a measured $M^2 < 1.2$ at the maximum output power level and was linearly polarized with a measured PER of 10 dB. The slight degradation of the PER observed at these high peak powers compared to the previous system is probably due to remaining mechanical stress from the fiber mount on the rod, which can degrade the PM feature for the extremely large core areas considered. Although the amplifier is not totally saturated at this power level, we limited ourselves to this output power to avoid damage of the rod. The 1-ps input pulses are slightly stretched to 1.5 ps at the maximum power level due to dispersion in the fiber. The spectral broadening that occurs with amplification is shown in Figure 7.6 (right). Without any

amplification, propagation of the seed pulses already generates more than 20 nm of spectrum due to SPM. At the maximum output power we observed over 35 nm of spectral broadening and some spectral shaping probably due to the gain spectrum of the fiber, which makes the spectrum asymmetric at higher output powers.

The compression stage consists of a single-pass two-grating compressor. The gratings used are 1250 l/mm transmission gratings. In order to compress the pulses at the maximum output power, the negative dispersion needed is approximately $-16\,000\text{ fs}^2$, which corresponds to a grating distance of approximately 1.3 mm in a double-pass configuration. At the expense of some spatial chirp that can be neglected, the compression scheme used was a one-pass two-grating compressor with a distance between the gratings of 2.6 mm. In this case, the measured spectrum at full power extends spatially over 170 μm . This can be neglected over a total beam diameter of 1.9 mm. With this compression scheme we achieved a compression efficiency of 86% at full power, and a resulting compressed power of 34 W. The compressed pulses were characterized using an SHG-FROG. The retrieved pulses can be seen in Figure 7.7 and are compared to the transform-limited pulse of the measured spectrum and the simulated pulses using the same software described for the first setup. The different pulse parameters are summarized in Table 7.II.

The retrieved pulses had a duration of 65 fs (FWHM), with 65% of the total amount of energy within the main pulse, resulting in 32 MW of peak power. Although the pulse energy is significantly lower than the one obtained in the previous setup, we obtain a similar peak power. This is partly due to the shorter pulses obtained, but also to the better Strehl-ratio of 81%, showing that we are closer to the transform-limited case. An even better Strehl ratio could be obtained by carefully optimizing third-order dispersion of the system. We can see in the top-right inset of Figure 7.7 that the retrieved spectrum and the independently measured spectrum using an optical spectrum analyzer are in good agreement. Furthermore, the retrieved pulses show a good agreement with our simulations. The small difference observed could probably be explained by the spectral asymmetry observed in the measured spectrum that is not present in the

simulations, since the software does not take into account the gain bandwidth of the rod.

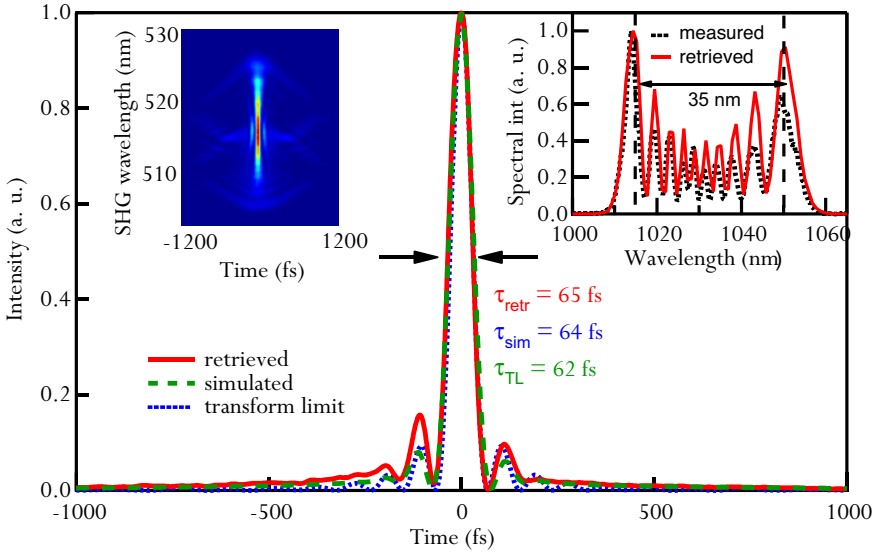


Figure 7.7: SHG-FROG characterization of the compressed pulses for the stretcher-free system at the maximum compressed power of 34 W (retrieved, simulated and transform-limit of the independently measured spectrum). Top right inset: Measured FROG trace. The FROG grid used was 256x256, and the retrieved error was $4 \cdot 10^{-3}$. Top right inset: measured spectrum at maximum output power.

	Retrieved	Transform-limit	Simulated
Pulse FWHM	65 fs	62 fs	64 fs
Peak Power	32 MW	39.3 MW	37.5 MW
Energy in the main pulse	65%	79%	72%
Strehl ratio	0.81	-	0.91

Table 7.II: Different pulse characteristics of the retrieved, simulated and transform-limited pulses.

7.1.4 Discussion on further scaling of these systems

- Damage and self-focusing limits

The main limitations of the systems described in this Paragraph are due to operation at high peak powers, close to intrinsic damage and self-focusing thresholds. Many investigations on fiber damage have been carried out in order to establish guidelines on how to avoid these detrimental effects [158, 163]. However, threshold values are always strongly dependent on experimental conditions such as pulse parameters, coupling conditions, and doping concentration (which is of particular importance to fiber amplifiers). We have summarized the different relevant operation parameters of our two fiber amplifier systems (Table 7.III), which identify the different mechanisms that currently limit further power scaling.

	2200 μm^2 core rod	4500 μm^2 core rod	Critical threshold
Peak power (output of the rod)	~ 2.2 MW	~ 3 MW	~ 4 MW [158]
Peak intensity (before end-cap)	~ 2 kW/ μm^2 (= $2 \cdot 10^{11}$ W/ cm^2)	~ 1.2 kW/ μm^2 (= $1.2 \cdot 10^{11}$ W/ cm^2)	> 2 kW/ μm^2 [164] (= $2 \cdot 10^{11}$ W/ cm^2)
Peak intensity (after end-cap)	~ 40 W/ μm^2 (= $4 \cdot 10^9$ W/ cm^2)	~ 44 W/ μm^2 (= $4.4 \cdot 10^9$ W/ cm^2)	
Pulse fluence (end of rod)	$2.4 \cdot 10^{-3}$ $\mu\text{J}/\mu\text{m}^2$	$6.4 \cdot 10^{-4}$ $\mu\text{J}/\mu\text{m}^2$	$1.9 \cdot 10^{-2}$ $\mu\text{J}/\mu\text{m}^2$ [165]*
Observations	Damage	No Damage	

* Tests performed using bulk undoped fused silica

Table 7.III: Operation points at maximum output power and reported damage parameters.

There are mainly three possible reasons for damage or beam degradation in fiber systems operated at high peak power levels:

- Self-focusing: The critical peak power threshold commonly used for silica fibers is 4 MW [158].

-
- Surface damage: The manufacturer reported values in the order of several hundred $\text{W}/\mu\text{m}^2$ for the surface damage threshold peak intensity of similar Yb-doped cores without an end-cap [164].
 - Bulk damage: Damage threshold values of bulk silica of $1.9 \text{ J}/\text{cm}^2$ were measured at similar pulse parameters as the ones used in this thesis [165].

In the case of the 55-cm rod with a core area of $2200 \mu\text{m}^2$, damage was observed at the same intensity level in two different occasions. In both cases, the damaged area was inside the rods and close to the interface between the end-cap and the rod where the maximum intensity reaches $\approx 2 \text{ kW}/\mu\text{m}^2$ (on the output side). The peak power of 2.2 MW does not reach values where significant beam degradation due to self-focusing was observed. This seems to indicate that the bulk damage threshold was reached, even though the values are far from the reported bulk damage thresholds [165]. However, the reported damage thresholds are for undoped silica, which differs from our experiment. A more detailed investigation is necessary to confirm these rod damage values. Nevertheless, they represent a good reference point to avoid damage in future experiments.

In the case of the 36-cm rod with a core area of $4500 \mu\text{m}^2$, neither damage nor beam degradation was observed at an even higher peak power of 3 MW. At this level, self-focusing does not seem to affect the beam quality at the output of the amplifier. The corresponding maximum intensity is $1.2 \text{ kW}/\mu\text{m}^2$, which is 60% lower than the value where damage was observed for the previous fiber. However, if we consider further power scaling of this system, beam degradation due to self-focusing might be apparent before surface or bulk damage are reached. Therefore, further scaling of the compressed peak power in this stretcher-free configuration requires an increase of the spectral broadening at this fixed maximum output power level.

- Possibilities for higher peak powers

- Input power of the seed

In both compression systems presented here, we clearly benefit from the initially high average and peak power of the oscillator, which directly saturates the one-pass amplifier and generates sufficient spectral broadening. We focus here on the second more compact stretcher-free system, where no damage was observed in our experiment.

In Figure 7.8 (left) we simulated the influence of the average power of the seed laser on the peak power of the compressed pulses for a constant average output power and constant rod length. The output power is kept constant by adapting the input pump power level. A higher input power corresponds to a lower overall gain in the rod. We can see that the compressed peak power is increased for a higher input average power. This is due to the lower accumulated nonlinear phase required to reach a certain pulse duration at the output, which leads to cleaner, more contrasted pulses (corresponding to a better achievable Strehl ratio). Higher average power from the modelocked TDL are clearly beneficial, and the ideal configuration would be passive broadening using an undoped rod-type fiber. However, to-date, passive rod-type fibers are not commercially available.

- Fiber length

Another possibility would be to increase the peak power by increasing the length of the rod. In Figure 7.8 (right), we simulated an increase of the length of the rod at a fixed pump and input power. As we can see, an increase of a factor of two in fiber length (from 300 mm to 600 mm) results in an output power increase of approximately 10%. We experience a higher benefit for the compressed peak power by more than a factor of two, because of the additional SPM accumulated in the longer rod. However, at the time of the experiment, only a 36-cm-long rod was available. Furthermore, increasing the length of the rod might lead to parasitic nonlinear effects such as Raman scattering.

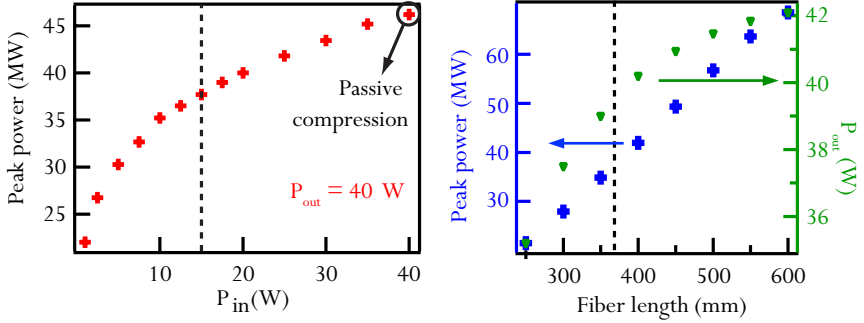


Figure 7.8: Simulations performed with home-programmed split-step Fourier propagation software. Left: Compressed peak power as a function of the input average power for a fixed average output power and fiber length. Right: Compressed peak power and average output power as a function of the fiber length.

7.1.5 Summary and outlook

We presented two systems for pulse compression of medium-energy TDLs and discussed the performance as well as the main limitations of these systems. The results are summarized in Table 7.IV.

	System 1	System 2
Length of fiber amplifier	55 cm	36 cm
Core diameter	70 μm	100 μm
Input average power (launched)	12 W	15 W
Input pulse duration	1.9 ps	1 ps
Maximum output average power	73 W	39.5 W
Output pulse duration	2.7 ps	1.5 ps
Output peak power	2.2 MW	3 MW
Compressed average power	55 W	34 W
Compressed pulse duration	98 fs	65 fs
Compressed energy	5.2 μJ	3.2 μJ
Compressed peak power	32.7 MW	32 MW
Strehl ratio	0.76	0.81
Limitation	Damage	-

Table 7.IV: Summary of the results obtained with the two rod-type fiber amplifier systems.

For both experiments, we used an Yb:YAG TDL seed with 16 W of average power, a pulse repetition rate of 10.6 MHz and a laser wavelength of 1030 nm. The resulting pulse energy is 1.6 μJ in 1-ps long pulses.

The first compression system consists of a 55-cm-long polarization-maintaining rod-type fiber amplifier with a core size diameter of 70 μm . We used the minimum stretching factor of the input pulses to avoid damage of the rod. We obtained, in this case, 55 W of compressed average power in 98-fs pulses, corresponding to a peak power of 32.7 MW and a pulse energy of 5.2 μJ . The main limitation of this system was damage observed at the highest average output power, which seems to indicate operation close to the bulk damage threshold of silica.

In the second compression setup, we used a shorter rod-type fiber (36 cm) with a larger core diameter of 100 μm , leading to a core area 2 times larger than for the 55-cm rod. This allowed us to directly seed the amplifier without stretching the input pulses. With this setup we achieved 34 W of compressed average power and pulses with a duration of 65-fs, leading to 32 MW of peak power. The larger core size allowed us to use a simpler stretcher-free configuration, where damage could be avoided at similar peak power levels in the rod. Nevertheless, self-focusing may be apparent in this case before damage can occur, which is one of the reasons why we limited the amplifier output average power to < 40 W. Stretching the input pulses to generate a lower peak power at the output facet of the fiber would represent an alternative to safely increase the output average power. However, this would be at the expense of simplicity of the setup, and of the quality of the compressed pulses.

In both amplifiers a compromise in peak power in the rod had to be made. In order to reach a high compression factor, significant peak power in the fiber was needed. The maximum applicable peak power is set by damage and/or self-focusing. Furthermore, the goal was to achieve high pulse energies (typically > 3 μJ) after compression in the simplest possible configuration. Therefore the stretcher-free approach was preferred.

In both cases, we achieved peak power levels > 30 MW at several μJ pulse energy. The high-power SESAM modelocked TDL used as a seed for both amplifiers allowed for simple setups where the oscillator directly

saturates the main amplifier and generates enough spectral broadening to support sub-100 fs pulses.

One could think of operating such an amplifier system in the parabolic regime where the obtained chirp due to the spectral broadening is quasi-linear and the quality of the compressed pulses is higher. However, for the picosecond source and sech^2 -shaped seed pulses this would require the use of long fibers, and parasitic nonlinear effects such as Stimulated Raman scattering (SRS) might degrade the convergence to the parabolic regime [166]. In this case, the use of a TDL as a seed with shorter pulses would be beneficial. Furthermore, the gain bandwidth limitation makes the compression schemes in this amplifying regime more challenging [167, 168].

Another approach would consist of extending the work on passive LMA fiber compression, with passive large mode area rod-type fibers directly seeded by higher peak power seeds. However, this would require stretched pulses of approximately 3 ps in order to avoid self-focusing. This larger stretching ratio makes compression to clean pulses with sub-100-fs challenging. Furthermore, in the past years, passive rod-type fiber development did not receive the same attention as rod-type fiber amplifiers, which limits their commercial availability.

Although high peak powers were obtained with the approach demonstrated in this Paragraph, the limitations of these systems seem to indicate that further peak power scaling to sub-50 fs pulses and/or higher energies require other compression schemes such as compression in gas-filled HC-PCFs.

7.2 Gas-filled hollow-core photonic-crystal fiber compression setup

The damage limitations of solid core fibers can be overcome by spectral broadening inside a gas-filled HC-PCF [160]. This technology offers a combination of long effective interaction length and small mode areas, which has resulted in several major breakthroughs in low-power nonlinear optics [169-171]. Furthermore, it offers the additional advantage of choosing different gases as the nonlinear medium.

Kagome-type HC-PCFs [172] are particularly promising since they exhibit a more than ten times lower field overlap with the surrounding silica structure [171]. In contrast to photonic bandgap-type fibers, the guiding mechanism is based on inhibited coupling between the core and cladding modes [171] and not the bandgap-effect. This type of fiber is immune to core-mode and surface-mode coupling [173], which represents one of the major sources of optical overlap with the silica surrounding the fiber core. Furthermore, typical core sizes of Kagome-type HC-PCF are larger than 30 μm . Since the damage threshold scales with the inverse of the optical overlap on one hand and with the modal effective area on the other, guidance of very high pulse energies and peak power levels becomes feasible [10, 161, 162]. In addition, Kagome-type HC-PCFs are advantageous because they exhibit very low dispersion and an ultrabroad guiding bandwidth, which are two particularly important features for applications with ultrashort laser pulses [171]. These advantages were recently confirmed by the demonstration of HHG inside a Kagome-PCF at peak intensities above 10^{14} W/cm² and peak powers of approximately 300 MW [10].

In this section, we present first proof-of-principle experiments that show the suitability of Kagome-type HC-PCF for pulse compression of μJ -class pulse energies using Xenon as the nonlinear medium. We temporally compressed a TDL generating 860 fs down to 48 fs with an average output power of 4.2 W at 3.9 MHz. After compression, we obtained a pulse energy of 1.1 μJ and over 10 MW of peak power, enhancing the input peak power by a factor of 5.

7.2.1 Experimental setup

The pulse compression experiments were driven by an Yb:YAG TDL similar to the system used in the previous section for amplification and compression in rod-type fiber amplifiers. Its cavity length was extended with a passive multi-pass cell [174] to achieve lower repetition rate and higher pulse energy. The system delivered up to 8 W of average power at 3.91 MHz. Out of these 8 W, 7.3 W of average power were available to launch into the HC-PCF, resulting in a pulse energy of 2 μJ and a pulse

duration of 860 fs at the input of the fiber. The experimental setup for the compression experiments is presented in Figure 7.9.

The Kagome-type fiber used in our experiment consists a 7-cell, 3-ring hypocycloid-core Kagome-cladding HC-PCF designed for operation at 1030 nm. Figure 7.9 (bottom middle) shows two near field images of this fiber. The fiber hypocycloid-shaped core has a diameter of 41 μm for the inner circumscribing circle and 48 μm for the outer one. The pitch is 13 μm , and the fiber outer diameter is 175 μm . We measured a mode field diameter of 30 μm for the input beam. The ideal fiber design has a perfect 6-folded symmetry without any distortion in the core structure, which should avoid detrimental depolarization effects.

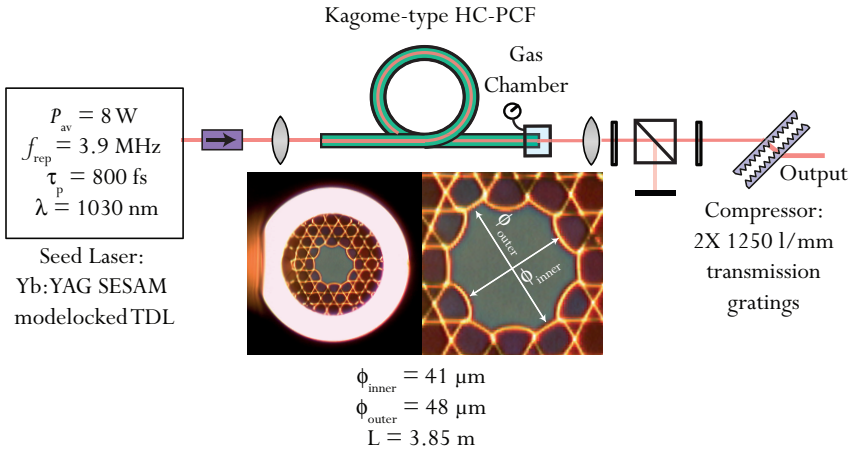


Figure 7.9: Experimental setup of the Kagome-type HC-PCF compression stage. Insets: 7-cell 3-ring hypocycloid-core Kagome-cladding HC-PCF used in these experiments: (left) image of the whole fiber (right) zoom into the hypocycloid-core Kagome HC-PCF exhibiting a core of 41/48 μm and a pitch of 13 μm .

The output of the laser was launched into the Kagome fiber with a set of lenses to ensure optimal mode matching to the fundamental mode of the fiber. The theoretical coupling efficiency for Kagome fibers is 94%, corresponding to the overlap between a TEM_{00} mode and the fundamental mode guided by the fiber (HE_{11}). In this experiment, we measured an approximate coupling efficiency of 86% using a short piece of fiber.

Furthermore, the losses in the fiber at 1030 nm were measured to be 283 dB/km, using a cutback measurement from 15 m to 5 m with a supercontinuum source. A gas chamber was placed on the back of the fiber using the same sealing technique as the one described in reference [175]. With this chamber, different gases can be injected into the fiber with adjustable pressure, and a stationary gradient of pressure over time can be achieved [176]. The input face was left open in order to avoid stress on the fiber structure, which could result in a reduced damage threshold [10, 175]. The fiber was coiled with a radius of approximately 50 cm.

7.2.2 Experimental results

In a preliminary experiment, we verified that no significant SPM was generated in air when the full power of the laser was launched into the fiber. This confirms a very low overlap of the field with the surrounding silica structure, and a good coupling into the fundamental mode. In addition, we measured the depolarization losses of this fiber and measured a PER of 9 dB over the 2.8 m length of fiber used for the compression experiment, which was independent of the power launched into the fiber. The small depolarization observed is probably due to residual stress in the coiled fiber and an imperfect mode matching to the fundamental mode of the fiber. As a result of these depolarization losses and the regular losses in the fiber, the resulting polarized power transmission through the 2.8 m of fiber was 63%.

In order to generate enough nonlinearity to spectrally broaden the spectrum of our TDL, we used Xenon, a single-atom gas with a significantly higher nonlinear refractive index than air (for Xenon, $n_2 = 8.1 \cdot 10^{-23} \text{ m}^2/\text{W}/\text{bar}$ at 800 nm [146]; for air, $n_2 = 2.9 \cdot 10^{-23} \text{ m}^2/\text{W}/\text{bar}$ at 800 nm [146]). Figure 7.10 shows the spectral broadening occurring on the main polarization of the output of the fiber when 15 bar of Xenon are applied on the chamber. The measured spectrum shows good agreement with the simulated spectrum using a split-step Fourier propagation software. In this case the polarized output power was 4.8 W, corresponding to a transmission of 63%. The output spectrum is 58 nm broad (FWHM).

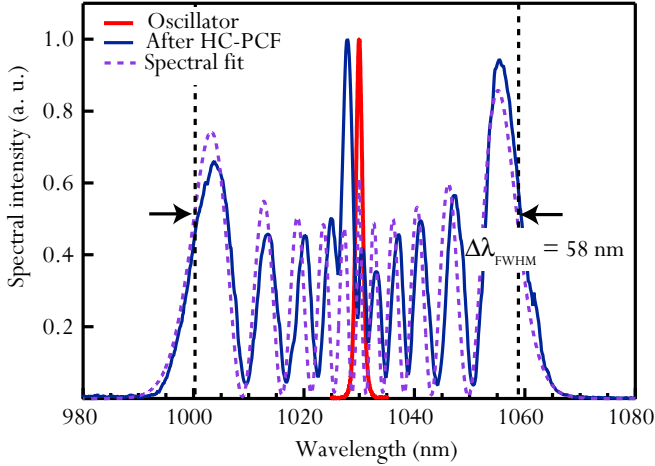


Figure 7.10: Spectral broadening observed after the Xenon-filled HC-PCF. The measurement shows good agreement with the simulated spectral broadening.

We compressed the pulses using a single stage compressor that consists of two diffractive gratings [177] with 1250 lines/mm used in a single-pass configuration. The compression efficiency through these two gratings is 89%, leading to 4.2 W of compressed average power. Figure 7.11 (top left inset) shows an SHG-FROG measurement of the pulses after the compression stage. The reconstructed intensity profile shows a pulse duration of 48 fs (FWHM). Based on this reconstruction, the peak power is 10 MW. The spectrum after the compressor was measured with an independent optical spectrum analyzer and shows good agreement with the spectrum retrieved by the FROG algorithm. The Fourier transform of the spectrum measured with the spectrum analyzer indicates a pulse duration of 44 fs (Figure 7.11, green), whereas the retrieved pulse has a FWHM of 48 fs (Figure 7.11, red). The peak power of the transform-limited pulse is 20 MW, i.e. double than that of the compressed pulse. This indicates that further optimization of our compression stage could potentially lead to higher peak powers, for example by including compensation of third-order dispersion.

Although higher peak power could have been achieved with an optimized compression setup, we achieved a large compression factor of

≈ 18 . We compressed 860 fs sech^2 pulses down to sub-50 fs pulses at an average power of 4.2 W. The pulse energy was 1.1 μJ , corresponding to a peak power of 10 MW. The overall compression efficiency of the system in terms of average power was 56%. In spite of the large residual energy in the wings of the pulse, the peak power could be increased by a factor of 5. The transform limit of the obtained broadened spectrum suggests that an increase of the peak power by nearly a factor of two could be obtained by optimizing our compression stage.

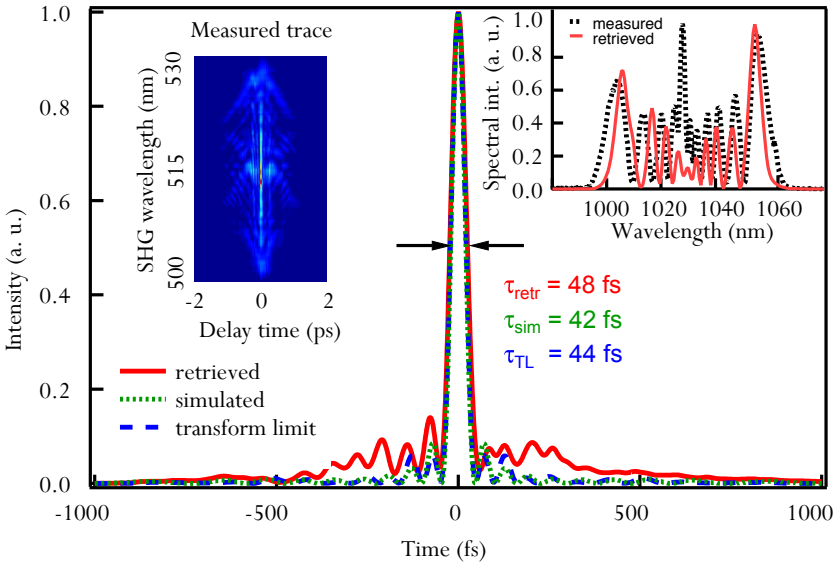


Figure 7.11: SHG-FROG characterization of the compressed pulses (retrieved, simulated and transform-limit of the independently measured spectrum). Top left inset: Measured FROG trace with a grid of 256x256. Top right inset: measured and retrieved spectrum.

7.3 Conclusion and outlook

In this Chapter, we presented two systems for compression of modelocked TDLs to the sub-100 fs range.

In the first Paragraph, we presented two systems based on rod-type fiber amplifiers that combined spectral broadening and amplification to higher average power levels of a medium-energy TDL. In both systems, we

achieved large peak power enhancement >10 , reaching pulse durations < 100 fs and peak powers > 30 MW. These systems proved useful to enhance the peak power of a standard medium-power TDL using commercially available rod-type-fibers. However, they were limited by operation close to the damage and self-focusing threshold of fused silica. Although a small improvement of the output peak power can be achieved up to some extent, these systems are ultimately limited by the necessary compromise between staying below the self-focusing/damage of silica and the desired large compression factor. In fact, much higher pulse energies could be guided by stretching the input pulses, but spectral broadening would lead in this case to uncompressible features that limit the achievable peak power.

These limitations can be overcome by using gas-filled HC-PCFs. In particular, Kagome-type HC-PCFs promise to be scalable to much higher pulse energies and peak powers, due to the extremely low field overlap between the propagating mode and the surrounding silica structure, which results in fibers with low losses and high damage and self-focusing thresholds. During the time frame of this thesis, we realized the first proof-of-principle experiments of pulse compression based on this type of fibers. In the latest results, we temporally compressed a TDL generating 860 fs down to 48 fs with an average output power of 4.2 W at 3.9 MHz in a Xenon-filled Kagome-type HC-PCF. This resulted in an enhancement of the peak power of this source by a factor >5 and a reduction of its pulse duration by a factor of 18.

Another promising approach that is currently being investigated, but that lies outside of the scope of this thesis, is to compress the pulses by using optical parametric chirped pulse amplification (OPCPA) schemes [76, 178]. Thin-disk lasers are ideal pump systems for such parametric amplification schemes, where in theory the amplification process takes place with no deposited heat. However, OPCPA at hundreds of watts of average power with high efficiency has never been demonstrated, and the challenges of such schemes still remain to be investigated.

Chapter 8 - Conclusion

During the timeframe of this thesis, different limits of modelocked TDLs were explored. As a result, cutting-edge ultrafast sources were developed that will open the door to exciting applications, for example, in strong-field physics. In addition to these future experiments, we expect to further push the limits of modelocked TDLs in the near future.

An important number of the results that we presented in this thesis were achieved thanks to an extensive study on damage limits and crucial parameters of SESAMs for high-power oscillators. As a result of this investigation, SESAMs with ideal parameters and high-damage thresholds were achieved that enabled us to push the technology to these new frontiers.

The first important achievement was the demonstration of TDLs with nearly bandwidth-limited pulses that reach pulse durations as short as 96 fs. Although in these preliminary experiments we achieve moderate output powers (5 W), we expect further power scaling to the 100-W level to be within reach, in particular with the improved SESAM designs developed during this thesis, and given the latest power scaling results obtained by operating the oscillator in a vacuum environment. Furthermore, these results seem to indicate that promising materials with significantly larger emission bandwidths than the ones used in this experiment should yield even shorter pulses at high average powers. This opens the door to highly nonlinear optics experiments driven directly by table-top oscillators, at high repetition rates and with high efficiency. Another promising possibility that is opened by these results is to exploit the high intracavity peak powers inside TDLs to drive highly nonlinear experiments.

The record short pulses demonstrated in the context of this work enabled us to perform the first CEO frequency measurement of a modelocked TDL. The detection of this characteristic frequency is the first crucial step towards full stabilization of this type of laser source. This seems to indicate that modelocked TDLs will be ideal unamplified high-power frequency combs, which are of interest in applications such as spectroscopy

or metrology.

In addition to pushing the pulse duration limits of TDLs, we extended the frontiers in terms of average power of ultrafast oscillators. Previous to the experiments presented in this thesis, the nonlinearity of air was recognized as one of the main contributions to the total phase shift experienced by the pulses within one round trip in the cavity. At high peak power, this phase shift can become too large and destabilize the modelocking mechanism. In this experiment, we reduced the influence of the nonlinearity of the ambient environment by operating the oscillator in a medium-vacuum environment. In this way, we could achieve 275 W of average power and a pulse energy of 16.9 μJ at a pulse duration of 583 fs. In the near future, we expect to further increase the pulse energy of our laser by further reducing the repetition rate of the laser. Currently, the main limitation to higher average powers appears to be thermal effects that occur in the dispersive mirrors. Future thermally improved mirror designs that are currently being investigated will allow us to reach higher average powers.

In order to use this system for future experiments, pulse compression will be the next key step. Several approaches appear suitable for pulse compression at this energy and average power level. HC-PCFs appear as one of the most promising approaches to reach sub-50 fs pulse durations at hundreds of MWs of peak power, which should be sufficient, for example, for initial HHG experiments.

References

- [1] M. Bronski, "Life without lasers?" (2010), retrieved <http://www.photonics.com/Article.aspx?AID=42747>.
- [2] T. H. Maiman, "Stimulated Optical Radiation in Ruby," *Nature* **187**, 493-494 (1960).
- [3] W. Sibbett, A. A. Lagatsky, and C. T. A. Brown, "The development and application of femtosecond laser systems," *Opt Express* **20**, 6989-7001 (2012).
- [4] U. Keller, "Ultrafast solid-state laser oscillators: a success story for the last 20 years with no end in sight," *Appl. Phys. B* **100**, 15-28 (2010).
- [5] U. Keller, "Recent developments in compact ultrafast lasers," *Nature* **424**, 831-838 (2003).
- [6] T. Südmeyer, S. V. Marchese, S. Hashimoto, C. R. E. Baer, G. Gingras, B. Witzel, and U. Keller, "Femtosecond laser oscillators for high-field science," *Nature Photonics* **2**, 599-604 (2008).
- [7] A. McPherson, G. Gibson, H. Jara, U. Johann, T. S. Luk, I. A. McIntyre, K. Boyer, and C. K. Rhodes, "Studies of multiphoton production of vacuum-ultraviolet radiation in the rare gases," *J. Opt. Soc. Am. B* **4**, 595-601 (1987).
- [8] M. Ferray, A. L'Huillier, X. F. Li, L. A. Lompré, G. Mainfray, and C. Manus, "Multiple-harmonic conversion of 1064 nm radiation in rare gases," *J. Phys. B: At. Mol. Opt. Phys.* **21**, L31-L35 (1988).
- [9] U. Keller, "Femtosecond to Attosecond Optics," *IEEE Photon. J.* **2**, 225-228 (2010).
- [10] O. H. Heckl, C. R. E. Baer, C. Kränkel, S. V. Marchese, F. Schapper, M. Holler, T. Südmeyer, J. S. Robinson, J. W. G. Tisch, F. Couny, P. Light, F. Benabid, and U. Keller, "High harmonic generation in a gas-filled hollow-core photonic crystal fiber," *Appl. Phys. B* **97**, 369-373 (2009).
- [11] S. Kim, J. H. Jin, Y. J. Kim, I. Y. Park, Y. Kim, and S. W. Kim, "High-harmonic generation by resonant plasmon field enhancement," *Nature* **453**, 757-760 (2008).
- [12] P. Russbuedt, T. Mans, J. Weitenberg, H. D. Hoffmann, and R. Poprawe, "Compact diode-pumped 1.1 kW Yb:YAG Innoslab femtosecond amplifier," *Opt. Lett.* **34**, 4169-4171 (2010).
- [13] T. Eidam, S. Hanf, E. Seise, T. V. Andersen, T. Gabler, C. Wirth, T. Schreiber, J. Limpert, and A. Tünnermann, "Femtosecond fiber CPA system emitting 830 W average output power," *Opt. Lett.* **35**, 94-96 (2010).
- [14] C. J. Saraceno, F. Emaury, O. H. Heckl, C. R. E. Baer, M. Hoffmann, C. Schriber, M. Golling, T. Südmeyer, and U. Keller, "275 W average output power from a femtosecond thin disk oscillator operated in a vacuum environment," *Opt Express* **20**, 23535-23541 (2012).
- [15] T. Metzger, A. Schwarz, C. Y. Teisset, D. Sutter, A. Killi, R. Kienberger, and F. Krausz, "High-repetition-rate picosecond pump laser based on a Yb:YAG disk amplifier for optical parametric amplification," *Opt. Lett.* **2009**, 2123-2125 (2009).
- [16] A. Giesen, H. Hügel, A. Voss, K. Wittig, U. Brauch, and H. Opower, "Scalable Concept for Diode-Pumped High-Power Solid-State Lasers," *Appl. Phys. B* **58**, 365-372 (1994).
- [17] A. Giesen and J. Speiser, "Fifteen Years of Work on Thin-Disk Lasers: Results and Scaling Laws," *IEEE J. Sel. Top. Quantum Electron.* **13**, 598-609 (2007).
- [18] U. Keller, K. J. Weingarten, F. X. Kärtner, D. Kopf, B. Braun, I. D. Jung, R. Fluck, C. Hönninger, N. Matuschek, and J. Aus der Au, "Semiconductor saturable absorber mirrors (SESAMs) for femtosecond to nanosecond pulse generation in solid-state lasers," *IEEE J. Sel. Top. Quantum Electron.* **2**, 435-453 (1996).
- [19] U. Keller, D. A. B. Miller, G. D. Boyd, T. H. Chiu, J. F. Ferguson, and M. T. Asom, "Solid-state low-loss intracavity saturable absorber for Nd:YLF lasers: an antiresonant semiconductor Fabry-Perot saturable absorber," *Opt. Lett.* **17**, 505-507 (1992).
- [20] J. Aus der Au, G. J. Spühler, T. Südmeyer, R. Paschotta, R. Hövel, M. Moser, S. Erhard, M. Karszewski, A. Giesen, and U. Keller, "16.2 W average power from a diode-pumped femtosecond Yb:YAG thin disk laser," *Opt. Lett.* **25**, 859-861 (2000).
- [21] D. Bauer, I. Zawischa, D. H. Sutter, A. Killi, and T. Dekorsy, "Mode-locked Yb:YAG thin-disk
-

- oscillator with 41 μJ pulse energy at 145 W average infrared power and high power frequency conversion," *Opt Express* **20**(2012).
- [22] R. J. Jones, K. D. Moll, M. J. Thorpe, and J. Ye, "Phase-Coherent Frequency Combs in the Vacuum Ultraviolet via High-Harmonic Generation inside a Femtosecond Enhancement Cavity," *Phys. Rev. Lett.* **94**, 193201 (2005).
- [23] R. Peters, *Ytterbium-dotierte Sesquioxide als hocheffiziente Lasermaterialien* (Shaker Verlag, Hamburg, Germany, 2009).
- [24] T. Y. Fan, "Heat Generation in Nd:YAG and Yb:YAG," *IEEE J. Quantum Elect.* **29**, 1457-1459 (1993).
- [25] A. Killi, C. Stolzenburg, I. Zawischa, D. Sutter, J. Kleinbauer, S. Schad, R. Brockmann, S. Weiler, J. Neuhaus, S. Kalfhues, E. Mehner, D. Bauer, H. Schlueter, and C. Schmitz, "The broad applicability of the disk laser principle - from CW to ps," *Proceedings of the SPIE - The International Society for Optical Engineering*, 71931T (71939 pp.) (2009).
- [26] V. Magni, "Multielement stable resonators containing a variable lens," *J. Opt. Soc. Am. A* **4**, 1962-1969 (1987).
- [27] M. Huonker, C. Schmitz, and A. Voss, "Laser Amplifying System," US Patent 6,963,592 (August 25, 2004 2005).
- [28] G. B. Venus, A. Sevan, V. I. Smirnov, and L. B. Glebov, "High-brightness narrow-line laser diode source with volume Bragg-grating feedback," in *Conference on High-Power Diode Laser Technology and Applications III*, 2005), 166-176.
- [29] E. Schmid, J. Speiser, and A. Giesen, "Characterisation of a Deformable Mirror for Compensation of the Thermal Lens in High Power Thin-Disk Lasers," in *Europhoton Conference 2010*, (Hamburg, Germany, 2010).
- [30] C. R. E. Baer, C. Kränkel, C. J. Saraceno, O. H. Heckl, M. Golling, R. Peters, K. Petermann, T. Südmeyer, G. Huber, and U. Keller, "Femtosecond thin disk laser with 141 W of average power," *Opt Lett* **35**, 2302-2304 (2010).
- [31] J. Czochralski, "A new method of measuring the speed of crystallisation in metals," *Z. Phys. Chem. Stoechiom. Verwandtschafts. F.* **92**, 219-221 (1917).
- [32] C. Hönninger, R. Paschotta, F. Morier-Genoud, M. Moser, and U. Keller, "Q-switching stability limits of continuous-wave passive mode locking," *J. Opt. Soc. Am. B* **16**, 46-56 (1999).
- [33] L. F. Mollenauer and R. H. Stolen, "The soliton laser," *Optics Lett.* **9**, 13-15 (1984).
- [34] F. X. Kärtner and U. Keller, "Stabilization of soliton-like pulses with a slow saturable absorber," *Opt. Lett.* **20**, 16-18 (1995).
- [35] F. X. Kärtner, I. D. Jung, and U. Keller, "Soliton Mode-Locking with Saturable Absorbers," *IEEE J. Sel. Top. Quant.* **2**, 540-556 (1996).
- [36] R. Paschotta and U. Keller, "Passive mode locking with slow saturable absorbers," *Appl. Phys. B* **73**, 653-662 (2001).
- [37] R. Grange, M. Haiml, R. Paschotta, G. J. Spuhler, L. Krainer, M. Golling, O. Ostinelli, and U. Keller, "New regime of inverse saturable absorption for self-stabilizing passively mode-locked lasers," *Appl. Phys. B* **80**, 151-158 (2005).
- [38] C. J. Saraceno, C. Schriber, M. Mangold, M. Hoffmann, O. H. Heckl, C. R. E. Baer, M. Golling, T. Südmeyer, and U. Keller, "SESAMs for high-power oscillators: design guidelines and damage thresholds," *IEEE J. Sel. Top. Quantum Electron.* **18**, 29-41 (2012).
- [39] M. Haiml, U. Siegner, F. Morier-Genoud, U. Keller, M. Luysberg, R. C. Lutz, P. Specht, and E. R. Weber, "Optical nonlinearity in low-temperature-grown GaAs: Microscopic limitations and optimization strategies," *Appl. Phys. Lett.* **74**, 3134-3136 (1999).
- [40] C. J. Saraceno, O. H. Heckl, C. R. E. Baer, C. Schriber, M. Golling, K. Beil, C. Kränkel, T. Südmeyer, G. Huber, and U. Keller, "Sub-100 femtosecond pulses from a SESAM modelocked thin disk laser," *Appl. Phys. B* **106**, 559-562 (2012).
- [41] S. V. Marchese, C. R. E. Baer, A. G. Engqvist, S. Hashimoto, D. J. H. C. Maas, M. Golling, T. Südmeyer, and U. Keller, "Femtosecond thin disk laser oscillator with pulse energy beyond the 10-microjoule level," *Opt. Express* **16**, 6397-6407 (2008).

References

- [42] S. V. Marchese, T. Südmeyer, M. Golling, R. Grange, and U. Keller, "Pulse energy scaling to 5 μ J from a femtosecond thin disk laser," *Opt. Lett.* **31**, 2728-2730 (2006).
- [43] J. Kuhl and J. Heppner, "Compression of Femtosecond Optical Pulses with Dielectric Multilayer Interferometers," *IEEE Transactions of Quantum Electronics* **QE-22**, 182-185 (1986).
- [44] J. Heppner and J. Kuhl, "Intracavity chirp compensation in a colliding pulse mode-locked laser using thin-film interferometers," *Appl. Phys. Lett.* **47**, 453 (1985).
- [45] J. Neuhaus, D. Bauer, J. Zhang, A. Killi, J. Kleinbauer, M. Kumkar, S. Weiler, M. Guina, D. H. Sutter, and T. Dekorsy, "Subpicosecond thin-disk laser oscillator with pulse energies of up to 25.9 microjoules by use of an active multipass geometry," *Opt. Express* **16**, 20530-20539 (2008).
- [46] J. Neuhaus, J. Kleinbauer, A. Killi, S. Weiler, D. Sutter, and T. Dekorsy, "Passively mode-locked Yb:YAG thin-disk laser with pulse energies exceeding 13 μ J by use of an active multipass geometry," *Opt. Lett.* **33**, 726-728 (2008).
- [47] G. J. Spühler, K. J. Weingarten, R. Grange, L. Krainer, M. Haiml, V. Liverini, M. Golling, S. Schon, and U. Keller, "Semiconductor saturable absorber mirror structures with low saturation fluence," *Appl. Phys. B* **81**, 27-32 (2005).
- [48] D. J. H. C. Maas, A. R. Bellancourt, M. Hoffmann, B. Rudin, Y. Barbarin, M. Golling, T. Südmeyer, and U. Keller, "Growth parameter optimization for fast quantum dot SESAMs," *Opt. Express* **16**, 18646-18656 (2008).
- [49] R. Paschotta, R. Häring, U. Keller, A. Garnache, S. Hoogland, and A. C. Tropper, "Soliton-like pulse-shaping mechanism in passively mode-locked surface-emitting semiconductor lasers," *Appl. Phys. B* **75**, 445-451 (2002).
- [50] L. Krainer, R. Paschotta, S. Lecomte, M. Moser, K. J. Weingarten, and U. Keller, "Compact Nd:YVO₄ lasers with pulse repetition rates up to 160 GHz," *IEEE J. Quantum Electron.* **38**, 1331-1338 (2002).
- [51] A. E. H. Oehler, T. Südmeyer, K. J. Weingarten, and U. Keller, "100 GHz passively mode-locked Er:Yb:glass laser at 1.5 μ m with 1.6-ps pulses," *Opt. Exp.* **16**, 21930-21935 (2008).
- [52] D. J. H. C. Maas, A.-R. Bellancourt, B. Rudin, M. Golling, H. J. Unold, T. Südmeyer, and U. Keller, "Vertical integration of ultrafast semiconductor lasers," *Appl. Phys. B* **88**, 493-497 (2007).
- [53] E. Innerhofer, T. Südmeyer, F. Brunner, R. Häring, A. Aschwanden, R. Paschotta, U. Keller, C. Hönninger, and M. Kumkar, "60 W average power in 810-fs pulses from a thin-disk Yb:YAG laser," *Opt. Lett.* **28**, 367-369 (2003).
- [54] T. R. Schibli, E. R. Thoen, F. X. Kärtner, and E. P. Ippen, "Suppression of Q-switched mode locking and break-up into multiple pulses by inverse saturable absorption," *Appl. Phys. B* **70**, S41-S49 (2000).
- [55] D. J. H. C. Maas, B. Rudin, A.-R. Bellancourt, D. Iwaniuk, S. V. Marchese, T. Südmeyer, and U. Keller, "High precision optical characterization of semiconductor saturable absorber mirrors," *Opt. Express* **16**, 7571-7579 (2008).
- [56] M. Haiml, R. Grange, and U. Keller, "Optical characterization of semiconductor saturable absorbers," *Appl. Phys. B* **79**, 331-339 (2004).
- [57] D. Maas, *MIXSELS - a new class of ultrafast semiconductor lasers*, Series in Quantum Electronics (Dissertation at ETH Zurich, Nr. 18121, Hartung-Gorre Verlag, Konstanz, 2009), Vol. 48.
- [58] E. W. Van Stryland, M. A. Woodall, H. Vanherzeele, and M. J. Soileau, "Energy band-gap dependence of two-photon absorption," *Opt. Lett.* **10**, 490-492 (1985).
- [59] K. J. Weingarten, Time Bandwidth Products (personal communication, 2010).
- [60] S. Gupta, M. Y. Frankel, J. A. Valdmanis, J. F. Whitaker, G. A. Mourou, F. W. Smith, and A. R. Calawa, "Subpicosecond carrier lifetime in GaAs grown by molecular beam epitaxy at low temperatures," *Appl. Phys. Lett.* **59**, 3276-3278 (1991).
- [61] G. L. Witt, "LTMBE GaAs: present status and perspectives," *Mater. Sci. Eng.* **B22**, 9 (1993).
- [62] A. J. Lochtefeld, M. R. Melloch, J. C. P. Chang, and E. S. Harmon, "The role of point defects and arsenic precipitates in carrier trapping and recombination in low-temperature grown GaAs," *Appl. Phys. Lett.* **69**, 1465-1467 (1996).
- [63] U. Siegner, R. Fluck, G. Zhang, and U. Keller, "Ultrafast high-intensity nonlinear absorption dynamics in low-temperature grown gallium arsenide," *Appl. Phys. Lett.* **69**, 2566-2568 (1996).
- [64] H. S. Loka, S. D. Benjamin, and P. W. E. Smith, "Optical Characterization of Low-Temperature-
-

-
- Grown GaAs for Ultrafast All-Optical Switching Devices," *IEEE J. Quantum Electron.* **34**, 1426-1437 (1998).
- [65] C. J. Saraceno, O. H. Heckl, C. R. E. Baer, M. Golling, T. Südmeyer, K. Beil, C. Kränkel, K. Petermann, G. Huber, and U. Keller, "SESAMs for high-power femtosecond modelocking: power scaling of an Yb:LuScO₃ thin disk laser to 23 W and 235 fs," *Opt Express* **19**(2011).
- [66] S. Kivisto, T. Hakulinen, A. Kaskela, B. Aitchison, D. P. Brown, A. G. Nasibulin, E. I. Kauppinen, A. Harkonen, and O. G. Okhotnikov, "Carbon nanotube films for ultrafast broadband technology," *Opt Express* **17**, 2358-2363 (2009).
- [67] Z. P. Sun, T. Hasan, F. Torrisi, D. Popa, G. Privitera, F. Q. Wang, F. Bonaccorso, D. M. Basko, and A. C. Ferrari, "Graphene Mode-Locked Ultrafast Laser," *Acs Nano* **4**, 803-810 (2010).
- [68] M. R. Brozel and G. E. Stillman, eds., *Properties of Gallium Arsenide* (Inspec, London, 1996).
- [69] V. J. Wittwer, O. D. Sieber, M. Mangold, M. Hoffmann, C. J. Saraceno, M. Golling, B. Tilma, T. Südmeyer, and U. Keller, "First MIXSEL with a quantum well saturable absorber: shorter pulse durations and higher repetition rates," in *Conference on Lasers and Electro-Optics (CLEO 2012)*, (2012),
- [70] U. Keller and A. C. Tropper, "Passively modelocked surface-emitting semiconductor lasers," *Phys. Rep.* **429**, 67-120 (2006).
- [71] T. Südmeyer, F. Brunner, E. Innerhofer, R. Paschotta, K. Furusawa, J. C. Baggett, T. M. Monro, D. J. Richardson, and U. Keller, "Nonlinear femtosecond pulse compression at high average power levels by use of a large-mode-area holey fiber," *Opt. Lett.* **28**, 1951-1953 (2003).
- [72] C. J. Saraceno, O. H. Heckl, C. R. E. Baer, T. Südmeyer, and U. Keller, "Pulse compression of a high-power thin disk laser using rod-type fiber amplifiers," *Opt Express* **19**, 1395-1407 (2011).
- [73] Y. Zaouter, D. N. Papadopoulos, M. Hanna, J. Boulet, L. Huang, C. Aguergaray, F. Druon, E. Mottay, P. Georges, and E. Cormier, "Stretcher-free high energy nonlinear amplification of femtosecond pulses in rod-type fibers," *Opt Lett* **33**, 107-109 (2008).
- [74] O. H. Heckl, C. J. Saraceno, C. R. E. Baer, T. Südmeyer, Y. Y. Wang, Y. Cheng, F. Benabid, and U. Keller, "Temporal pulse compression in a xenon-filled Kagome-type hollow-core photonic crystal fiber at high average power," *Opt Express* **19**, 19142-19149 (2011).
- [75] J. Rothhardt, S. Hadrich, H. Carstens, N. Herrick, S. Demmler, J. Limpert, and A. Tunnermann, "1 MHz repetition rate hollow fiber pulse compression to sub-100-fs duration at 100 W average power," *Opt Lett* **36**, 4605-4607 (2011).
- [76] J. Rothhardt, S. Hadrich, E. Seise, M. Krebs, F. Tavella, A. Willner, S. Dusterer, H. Schlarb, J. Feldhaus, J. Limpert, J. Rossbach, and A. Tunnermann, "High average and peak power few-cycle laser pulses delivered by fiber pumped OPCPA system," *Opt Express* **18**, 12719-12726 (2010).
- [77] B. Deppe, "Ytterbium dotierte oxidische Lasermaterialien mit breitbandiger Emission (Diplomarbeit)," (Institute for Laser Physics, University of Hamburg, 2012).
- [78] T. Südmeyer, C. Kränkel, C. R. E. Baer, O. H. Heckl, C. J. Saraceno, M. Golling, R. Peters, K. Petermann, G. Huber, and U. Keller, "High-power ultrafast thin disk laser oscillators and their potential for sub-100-femtosecond pulse generation," *Appl. Phys. B* **97**, 281-295 (2009).
- [79] P. Lacovara, H. K. Choi, C. A. Wang, R. L. Aggarwal, and T. Y. Fan, "Room-temperature diode-pumped Yb:YAG laser," *Opt. Lett.* **16**, 1089-1091 (1991).
- [80] F. Brunner, E. Innerhofer, S. V. Marchese, T. Südmeyer, R. Paschotta, T. Usami, H. Ito, S. Kurimura, K. Kitamura, G. Arisholm, and U. Keller, "Powerful red-green-blue laser source pumped with a mode-locked thin disk laser," *Opt. Lett.* **29**, 1921-1923 (2004).
- [81] C. Hönninger, R. Paschotta, M. Graf, F. Morier-Genoud, G. Zhang, M. Moser, S. Biswal, J. Nees, A. Braun, G. A. Mourou, I. Johannsen, A. Giesen, W. Seiber, and U. Keller, "Ultrafast ytterbium-doped bulk lasers and laser amplifiers," *Appl. Phys. B* **69**, 3-17 (1999).
- [82] C. Hönninger, G. Zhang, U. Keller, and A. Giesen, "Femtosecond Yb:YAG laser using semiconductor saturable absorbers," *Opt. Lett.* **20**, 2402-2404 (1995).
- [83] O. Pronin, J. Brons, C. Grasse, V. Pervak, G. Boehm, M. C. Amann, V. L. Kalashnikov, A. Apolonski, and F. Krausz, "High-power 200 fs Kerr-lens mode-locked Yb:YAG thin-disk oscillator," *Opt Lett* **36**, 4746-4748 (2011).
- [84] C. R. E. Baer, C. Kränkel, C. J. Saraceno, O. H. Heckl, M. Golling, T. Südmeyer, R. Peters, K. Petermann, G. Huber, and U. Keller, "Femtosecond Yb:Lu₂O₃ thin disk laser with 63 W of average power,"
-

References

Opt. Lett. **34**, 2823-2825 (2009).

[85] C. J. Saraceno, S. Pekarek, O. H. Heckl, C. R. E. Baer, C. Schriber, M. Golling, K. Beil, C. Kränkel, G. Huber, U. Keller, and T. Südmeyer, "Self-referenceable frequency comb from an ultrafast thin disk laser," *Opt. Express* **20**(2012).

[86] C. J. Saraceno, C. Schriber, O. H. Heckl, C. R. E. Baer, M. Golling, K. Beil, C. Kränkel, T. Südmeyer, G. Huber, and U. Keller, "25 W, 185 fs pulses from an Yb:Lu₂O₃ modelocked thin disk laser," in *Europhoton 2012*, 2012),

[87] G. Palmer, M. Schultze, M. Siegel, M. Emons, U. Bunting, and U. Morgner, "Passively mode-locked Yb:KLu(WO₄)₂ thin-disk oscillator operated in the positive and negative dispersion regime," *Opt. Lett.* **33**, 1608-1610 (2008).

[88] F. Brunner, T. Südmeyer, E. Innerhofer, R. Paschotta, F. Morier-Genoud, J. Gao, K. Contag, A. Giesen, V. E. Kisel, V. G. Shcherbitsky, N. V. Kuleshov, and U. Keller, "240-fs pulses with 22-W average power from a mode-locked thin-disk Yb:KY(WO₄)₂ laser," *Opt. Lett.* **27**, 1162-1164 (2002).

[89] C. J. Saraceno, O. H. Heckl, C. R. E. Baer, M. Golling, T. Südmeyer, K. Beil, C. Kränkel, K. Petermann, G. Huber, and U. Keller, "CW and Modelocked Operation of an Yb:(Sc,Y,Lu)(2)O(3) Thin-disk Laser," 2011 Conference on Lasers and Electro-Optics (CLEO) (2011).

[90] S. Ricaud, A. Jaffres, K. Wentsch, A. Sugauma, B. Viana, P. Loiseau, B. Weichelt, M. Abdou-Ahmed, A. Voss, T. Graf, D. Rytz, C. Hönninger, E. Mottay, P. Georges, and F. Druon, "Femtosecond Yb:CaGdAlO₄ thin-disk oscillator," *Opt Lett* **37**, 3984-3987 (2012).

[91] O. H. Heckl, C. Kränkel, C. R. E. Baer, C. J. Saraceno, T. Südmeyer, K. Petermann, G. Huber, and U. Keller, "Continuous-wave and modelocked Yb:YCOB thin disk laser: first demonstration and future prospects," *Opt. Exp.* **18**, 19201-19208 (2010).

[92] C. R. E. Baer, C. Kränkel, O. H. Heckl, M. Golling, T. Südmeyer, R. Peters, K. Petermann, G. Huber, and U. Keller, "227-fs Pulses from a Mode-Locked Yb:LuScO₃ Thin Disk Laser," *Opt. Express* **17**, 10725-10730 (2009).

[93] O. Pronin, J. Brons, C. Grasse, V. Pervak, G. Boehm, M. C. Amann, V. L. Kalashnikov, A. Apolonski, and F. Krausz, "High-power 200 fs Kerr-lens mode-locked Yb:YAG thin-disk oscillator," *Opt. Lett.* **36**, 4746-4748 (2011).

[94] N. V. Kuleshov, A. A. Lagatsky, V. G. Shcherbitsky, V. P. Mikhailov, E. Heumann, T. Jensen, A. Diening, and G. Huber, "CW laser performance of Yb and Er,Yb doped tungstates," *Appl. Phys. B* **64**, 409-413 (1997).

[95] N. V. Kuleshov, A. A. Lagatsky, A. V. Podlipensky, V. P. Mikhailov, and G. Huber, "Pulsed laser operation of Yb-doped KY(WO₄)₂ and KGd(WO₄)₂," *Opt. Lett.* **22**, 1317-1319 (1997).

[96] C. Kränkel, J. Johannsen, R. Peters, K. Petermann, and G. Huber, "Continuous-wave high power laser operation and tunability of Yb:LaSc₃(BO₃)₄ in thin disk configuration," *Appl. Phys. B* **87**, 217-220 (2007).

[97] C. Kränkel, R. Peters, K. Petermann, P. Loiseau, G. Aka, and G. Huber, "Efficient continuous-wave thin disk laser operation of Yb:Ca₄YO(BO₃)₃ in EIIZ and EIIX orientations with 26 W output power," *J. Opt. Soc. Am. B* **26**, 1310-1314 (2009).

[98] A. Agnesi, A. Greborio, F. Pirzio, G. Reali, J. A. D. Au, and A. Guandalini, "40-fs Yb³⁺:CaGdAlO₄ laser pumped by a single-mode 350-mW laser diode," *Opt Express* **20**(2012).

[99] A. Greborio, A. Guandalini, and J. A. D. Au, "Sub-100 fs pulses with 12.5-W from Yb:CALGO based oscillators," *Proc Spie* **8235**(2012).

[100] J. Liu, M. Rico, U. Griebner, V. Petrov, V. Peters, K. Petermann, and G. Huber, "Efficient room temperature continuous-wave operation of an Yb³⁺:Sc₂O₃ crystal laser at 1041.6 and 1094.6 nm," *Phys. Stat. Sol. (a)* **202**, R19-R21 (2005).

[101] R. Peters, C. Kränkel, K. Petermann, and G. Huber, "Broadly tunable high-power Yb:Lu₂O₃ thin disk laser with 80% slope efficiency," *Opt. Express* **15**, 7075-7082 (2007).

[102] L. Fornasiero, E. Mix, V. Peters, K. Petermann, and G. Huber, "New Oxide Crystals for Solid State Lasers," *Cryst. Res. Technol.* **34**, 255-260 (1999).

[103] R. H. Hoskins and B. H. Soffer, "Stimulated Emission from Y₂O₃:Nd³⁺," *Applied Physics Letters* **4**, 22-& (1964).

-
- [104] J. Stone and C. A. Burrus, "Nd-Y₂O₃ single-crystal fiber laser - room-temperature cw operation at 1.07- μ m and 1.35- μ m wavelength," *Journal of Applied Physics* **49**, 2281-2287 (1978).
- [105] R. Peters, C. Kränkel, K. Petermann, and G. Huber, "Crystal growth by the heat exchanger method, spectroscopic characterization and laser operation of high-purity Yb:Lu₂O₃," *J. Cryst. Growth* **310**, 1934-1938 (2008).
- [106] C. Barta, F. Petru, and B. Hajek, "Über die Darstellung des Einkristalls von Scandiumoxid," *Naturwissenschaften* **45**, 36-36 (1958).
- [107] K. Petermann, L. Fornasiero, E. Mix, and V. Peters, "High melting sesquioxides: crystal growth, spectroscopy, and laser experiments," *Opt. Mater.* **19**, 67-71 (2002).
- [108] K. Petermann, G. Huber, L. Fornasiero, S. Kuch, E. Mix, V. Peters, and S. A. Basun, "Rare-earth-doped sesquioxides," *J. Lumin.* **87-89**, 973-975 (2000).
- [109] K. Petermann, D. Fagundes-Peters, J. Johannsen, M. Mond, V. Peters, J. J. Romero, S. Kutovoi, J. Speiser, and A. Giesen, "Highly Yb-doped oxides for thin-disc lasers," *Journal of Crystal Growth* **275**, 135-140 (2005).
- [110] P. Klopp, V. Petrov, U. Griebner, K. Petermann, V. Peters, and G. Erbert, "Highly efficient mode-locked Yb:Sc₂O₃ laser," *Opt. Lett.* **29**, 391-393 (2004).
- [111] S. V. Marchese, C. R. E. Baer, A. G. Engqvist, M. Golling, D. J. H. C. Maas, T. Südmeyer, U. Keller, R. Peters, C. Kränkel, K. Petermann, and G. Huber, "Efficient femtosecond Yb:Lu₂O₃ thin disk laser," in *Advanced Solid-State Photonics (ASSP)*, (2008), paper ME5.
- [112] R. Peters, K. Beil, C. Kränkel, K. Schenk, K. Petermann, and G. Huber, "Ytterbium-doped Sesquioxides for High-Power Solid-State Lasers: Recent Progress in Crystal Growth and Laser Operation," in *Conference on Lasers and Electro-Optics (Europe)*, (2009), paper CA9.1.
- [113] R. Peters, K. Petermann, and G. Huber, "A New Mixed Sesquioxide Yb:LuScO₃: Spectroscopic Properties and Highly Efficient Thin-Disk Laser Operation," in *Advanced Solid-State Photonics (ASSP)*, (2009), paper MC4.
- [114] R. Peters, C. Kränkel, S. T. Fredrich-Thornton, K. Beil, K. Petermann, G. Huber, O. H. Heckl, C. R. E. Baer, C. J. Saraceno, T. Südmeyer, and U. Keller, "Thermal analysis and efficient high power continuous-wave and mode-locked thin disk laser operation of Yb-doped sesquioxides," *Appl Phys B-Lasers O* **102**, 509-514 (2011).
- [115] B. Weichelt, A. Voss, M. A. Ahmed, and T. Graf, "Enhanced performance of thin-disk lasers by pumping into the zero-phonon line," *Opt Lett* **37**, 3045-3047 (2012).
- [116] S. V. Marchese, C. R. E. Baer, R. Peters, C. Kränkel, A. G. Engqvist, M. Golling, D. J. H. C. Maas, K. Petermann, T. Südmeyer, G. Huber, and U. Keller, "Efficient femtosecond high power Yb:Lu₂O₃ thin disk laser," *Opt. Express* **15**, 16966-16971 (2007).
- [117] M. Huonker, A. Voss, and C. Schmitz, "aserverstärkersystem: Offenlegungsschrift des deutschen Patent- und Markenamts (DE 100 61 424 A 1)," (2000).
- [118] C. R. E. Baer, O. H. Heckl, C. J. Saraceno, C. Schriber, C. Kränkel, T. Südmeyer, and U. Keller, "Frontiers in passively mode-locked high-power thin disk laser oscillators," *Opt Express* **20**, 7054-7065 (2012).
- [119] C. J. Saraceno, O. H. Heckl, C. R. E. Baer, M. Golling, T. Südmeyer, C. Kränkel, K. Beil, K. Petermann, G. Huber, and U. Keller, "SESAMs for high-power femtosecond modelocking: power scaling of an Yb:LuScO₃ thin disk laser to 23 W and 235 fs," *Opt Express* **19**, 20288-20300 (2011).
- [120] C. J. Saraceno, O. H. Heckl, C. R. E. Baer, C. Schriber, M. Golling, K. Beil, C. Kränkel, T. Südmeyer, G. Huber, and U. Keller, "Sub-100 femtosecond pulses from a SESAM modelocked thin disk laser," *Appl. Phys. B (Rapid Communication)* **Online First**, 1-4 (2012).
- [121] M. J. Weber, *Handbook of optical materials*, The CRC Press laser and optical science and technology series (CRC Press, Boca Raton, 2003), p. 512 p.
- [122] J. Wang, M. Sheikbahaee, A. A. Said, D. J. Hagan, and E. W. Vanstryland, "Time-Resolved Z-Scan Measurements of Optical Nonlinearities," *J Opt Soc Am B* **11**, 1009-1017 (1994).
- [123] H. R. Telle, G. Steinmeyer, A. E. Dunlop, J. Stenger, D. H. Sutter, and U. Keller, "Carrier-envelope offset phase control: A novel concept for absolute optical frequency measurement and ultrashort pulse generation," *Appl. Phys. B* **69**, 327-332 (1999).
-

-
- [124] D. J. Jones, S. A. Diddams, J. K. Ranka, A. Stentz, R. S. Windeler, J. L. Hall, and S. T. Cundiff, "Carrier-envelope phase control of femtosecond mode-locked lasers and direct optical frequency synthesis," *Science* **288**, 635-639 (2000).
- [125] C. Gohle, T. Udem, M. Herrmann, J. Rauschenberger, R. Holzwarth, H. A. Schuessler, F. Krausz, and T. W. Hänsch, "A frequency comb in the extreme ultraviolet," *Nature* **436**, 234-237 (2005).
- [126] R. Jason Jones, K. D. Moll, M. J. Thorpe, and J. Ye, "Phase-Coherent Frequency Combs in the Vacuum Ultraviolet via High-Harmonic Generation inside a Femtosecond Enhancement Cavity," *Phys. Rev. Lett.* **94**, 193201 (2005).
- [127] I. Hartl, T. R. Schibli, A. Marcinkevicius, D. C. Yost, D. D. Hudson, M. E. Fermann, and J. Ye, "Cavity-enhanced similariton Yb-fiber laser frequency comb: 3×10^{14} W/cm² peak intensity at 136 MHz," *Opt. Lett.* **32**, 2870-2872 (2007).
- [128] A. Ozawa, J. Rauschenberger, C. Gohle, M. Herrmann, D. R. Walker, V. Pervak, A. Fernandez, R. Graf, A. Apolonski, R. Holzwarth, F. Krausz, T. W. Hansch, and T. Udem, "High harmonic frequency combs for high resolution spectroscopy," *Phys Rev Lett* **100**(2008).
- [129] I. Pupeza, T. Eidam, J. Rauschenberger, B. Bernhardt, A. Ozawa, E. Fill, A. Apolonski, T. Udem, J. Limpert, Z. A. Alahmed, A. M. Azzeer, A. Tunnermann, T. W. Hansch, and F. Krausz, "Power scaling of a high-repetition-rate enhancement cavity," *Opt Lett* **35**, 2052-2054 (2010).
- [130] D. C. Yost, A. Cingoz, T. K. Allison, A. Ruehl, M. E. Fermann, I. Hartl, and J. Ye, "Power optimization of XUV frequency combs for spectroscopy applications," *Opt Express* **19**, 23483 - 23493 (2011).
- [131] M. Herrmann, M. Haas, U. D. Jentschura, F. Kottmann, D. Leibfried, G. Saathoff, C. Gohle, A. Ozawa, V. Batteiger, S. Knunz, N. Kolachevsky, H. A. Schussler, T. W. Hansch, and T. Udem, "Feasibility of coherent xuv spectroscopy on the 1S-2S transition in singly ionized helium," *Phys Rev A* **79**(2009).
- [132] W. G. Rellergert, D. D., G. R. R., H. M. P., T. J. P., and H. E. R., "Constraining the evolution of the fundamental constants with a solid-state optical frequency reference based on the 229Th nucleus," *Phys Rev Lett* **104**(2010).
- [133] A. Cingoz, D. C. Yost, T. K. Allison, A. Ruehl, M. E. Fermann, I. Hartl, and J. Ye, "Direct frequency comb spectroscopy in the extreme ultraviolet," *Nature* **482**, 68-71 (2012).
- [134] D. C. Yost, T. R. Schibli, and J. Ye, "Efficient output coupling of intracavity high-harmonic generation," *Opt. Lett.* **33**, 1099-1101 (2008).
- [135] Y. Y. Yang, F. Sussmann, S. Zherebtsov, I. Pupeza, J. Kaster, D. Lehr, H. J. Fuchs, E. B. Kley, E. Fill, X. M. Duan, Z. S. Zhao, F. Krausz, S. L. Stebbings, and M. F. Kling, "Optimization and characterization of a highly-efficient diffraction nanograting for MHz XUV pulses," *Opt Express* **19**, 1954-1962 (2011).
- [136] K. D. Moll, R. J. Jones, and J. Ye, "Output coupling methods for cavity-based high-harmonic generation," *Opt Express* **14**, 8189-8197 (2006).
- [137] J. J. McFerran, W. C. Swann, B. R. Washburn, and N. R. Newbury, "Suppression of pump-induced frequency noise in fiber-laser frequency combs leading to sub-radian f (ceo) phase excursions," *Appl Phys B-Lasers O* **86**, 219-227 (2007).
- [138] F. Lücking, A. Assion, A. Apolonski, F. Krausz, and G. Steinmeyer, "Long-term carrier-envelope-phase-stable few-cycle pulses by use of the feed-forward method," *Opt Lett* **37**, 2076-2078 (2012).
- [139] P. Jojart, A. Borzsonyi, B. Borchers, G. Steinmeyer, and K. Osvay, "Agile linear interferometric method for carrier-envelope phase drift measurement," *Opt Lett* **37**, 836-838 (2012).
- [140] J. M. Dudley, G. Genty, and S. Coen, "Supercontinuum generation in photonic crystal fiber," *Reviews of Modern Physics* **78**, 1135-1184 (2006).
- [141] S. Pekarek, T. Südmeyer, S. Lecomte, K. Stefan, J. M. Dudley, and U. Keller, "Self-referencable frequency comb from a gigahertz diode-pumped solid state laser," *Opt. Express* **19**, 16491-16497 (2011).
- [142] A. Ruehl, A. Marcinkevicius, M. E. Fermann, and I. Hartl, "80 W, 120 fs Yb-fiber frequency comb," *Opt Lett* **35**, 3015-3017 (2010).
- [143] M. C. Stumpf, S. C. Zeller, A. Schlatter, T. Okuno, T. Südmeyer, and U. Keller, "Fiber-Broadened Passively Modelocked Er:Yb:Glass Laser for High-Resolution Optical Coherence Tomography," *Opt. Express* **16**, 10572-10579 (2008).
- [144] S. Pekarek, C. Fiebig, M. C. Stumpf, A. E. H. Oehler, K. Paschke, G. Erbert, T. Südmeyer, and U. Keller, "Diode-pumped gigahertz femtosecond Yb:KGW laser with a peak power of 3.9 kW," *Opt. Express*
-

18, 16320-16326 (2010).

[145] R. Paschotta, A. Schlatter, S. C. Zeller, H. R. Telle, and U. Keller, "Optical phase noise and carrier-envelope offset noise of mode-locked lasers," *Appl. Phys. B* **82**, 265-273 (2006).

[146] E. T. J. Nibbering, G. Grillon, M. A. Franco, B. S. Prade, and A. Mysyrowicz, "Determination of the inertial contribution to the nonlinear refractive index of air, N₂, and O₂ by use of unfocused high-intensity femtosecond laser pulses," *J. Opt. Soc. Am. B* **14**, 650-660 (1997).

[147] D. Bauer, F. Schättiger, J. Kleinbauer, D. Sutter, A. Killi, and T. Dekorsy, "Energies above 30 μ J and average power beyond 100 W directly from a mode - locked thin - disk oscillator," in *Advanced Solid-State Photonics* (Istanbul, Turkey, 2011).

[148] Y. Shimoji, A. T. Fay, R. S. F. Chang, and N. Djeu, "Direct Measurement of the Nonlinear Refractive-Index of Air," *J Opt Soc Am B* **6**, 1994-1998 (1989).

[149] C. R. E. Baer, O. H. Heckl, C. J. Saraceno, C. Schriber, C. Krankel, T. Sudmeyer, and U. Keller, "Frontiers in passively mode-locked high-power thin disk laser oscillators," *Optics Express* **20**, 7054-7065 (2012).

[150] J. A. Arnaud, "Degenerate Optical Cavities," *Appl. Opt.* **8**, 189-195 (1969).

[151] Q. Zhang, B. Ozygus, and H. Weber, "Degeneration effects in laser cavities," *Eur. Phys. J. AP* **6**, 293-298 (1999).

[152] R. Paschotta, "Beam quality deteriorations of lasers caused by intracavity beam distortions," *Opt. Exp.* **14**, 6069-6074 (2006).

[153] A. E. Siegman, *Lasers* (University Science Books, Mill Valley, California, 1986).

[154] A. Bullington, "Thermal loading and modal frequency degeneracy in optical resonators for the laser interferometer gravitational-wave observatory (LIGO)," (Stanford University, 2009).

[155] W. Winkler, K. Danzmann, A. Rudiger, and R. Schilling, "Heating by Optical-Absorption and the Performance of Interferometric Gravitational-Wave Detectors," *Phys Rev A* **44**, 7022-7036 (1991).

[156] D. Herriott, H. Kogelnik, and R. Kompfner, "Off-Axis Paths in Spherical Mirror Interferometers," *Appl. Opt.* **3**, 523-526 (1964).

[157] E. Innerhofer, F. Brunner, S. V. Marchese, R. Paschotta, U. Keller, K. Furusawa, J. C. Baggett, T. M. Monro, and D. J. Richardson, "32 W of average power in 24-fs pulses from a passively mode-locked thin disk laser with nonlinear fiber compression," in *Advanced Solid-State Photonics (ASSP)*, (2005), paper TuA3.

[158] A. V. Smith, B. T. Do, G. R. Hadley, and R. L. Farrow, "Optical Damage Limits to Pulse Energy From fibers," *Ieee J Sel Top Quant* **15**, 153-158 (2009).

[159] C. P. Hauri, W. Kornelis, F. W. Helbing, A. Heinrich, A. Courairon, A. Mysyrowicz, J. Biegert, and U. Keller, "Generation of intense, carrier-envelope phase-locked few-cycle laser pulses through filamentation," *Appl. Phys. B* **79**, 673-677 (2004).

[160] F. Benabid and P. J. Roberts, "Linear and nonlinear optical properties of hollow core photonic crystal fiber," *J Mod Optic* **58**, 87-124 (2011).

[161] Y. Y. Wang, N. V. Wheeler, F. Couny, P. J. Roberts, and F. Benabid, "Low loss broadband transmission in hypocycloid-core Kagome hollow-core photonic crystal fiber," *Opt. Lett.* **36**, 669-671 (2011).

[162] B. Beaudou, F. Gerome, Y. Y. Wang, M. Alharbi, T. D. Bradley, G. Humbert, J. L. Auguste, J. M. Blondy, and F. Benabid, "Millijoule laser pulse delivery for spark ignition through kagome hollow-core fiber," *Opt Lett* **37**, 1430-1432 (2012).

[163] A. V. Smith and B. T. Do, "Bulk and surface laser damage of silica by picosecond and nanosecond pulses at 1064 nm," *Applied Optics* **47**, 4812-4832 (2008).

[164] K. Hansen, NKT Photonics (personal communication, 2010).

[165] S. Marchese, *Towards high field physics with high power thin disk laser oscillators* (Dissertation at ETH Zurich, Nr. 17583, Hartung-Gorre Verlag, Konstanz, 2007).

[166] M. E. Fermann, V. I. Kruglov, B. C. Thomsen, J. M. Dudley, and J. D. Harvey, "Self-similar propagation and amplification of parabolic pulses in optical fibers," *Phys Rev Lett* **84**, 6010-6013 (2000).

[167] D. N. Papadopoulos, Y. Zaouter, M. Hanna, F. Druon, E. Mottay, E. Cormier, and P. Georges, "Generation of 63 fs 4.1 MW peak power pulses from a parabolic fiber amplifier operated beyond the gain bandwidth limit," *Opt Lett* **32**, 2520-2522 (2007).

[168] Y. Zaouter, D. N. Papadopoulos, M. Hanna, F. Druon, E. Cormier, and P. Georges, "Third-

References

order spectral phase compensation in parabolic pulse compression," *Opt Express* **15**, 9372-9377 (2007).

[169] P. S. J. Russell, "Photonic-crystal fibers," *Journal of Lightwave Technology* **24**, 4729-4749 (2006).

[170] F. Benabid, J. C. Knight, G. Antonopoulos, and P. S. J. Russell, "Stimulated Raman Scattering in Hydrogen-Filled Hollow-Core Photonic Crystal Fiber," *Science* **298**, 399-402 (2002).

[171] F. Couny, F. Benabid, P. J. Roberts, P. S. Light, and M. G. Raymer, "Generation and photonic guidance of multi-octave optical-frequency combs," *Science* **318**, 1118-1121 (2007).

[172] X. Wang and J. H. Eberly, "Multielectron Effects in Sequential Double Ionization with Elliptical Polarization," arXiv:1102.0221v1 (2011).

[173] J. West, C. Smith, N. Borrelli, D. Allan, and K. Koch, "Surface modes in air-core photonic band-gap fibers," *Opt. Express* **12**, 1485-1496 (2004).

[174] A. M. Kowalevich, A. Sennaroglu, A. T. Zare, and J. G. Fujimoto, "Design principles of q -preserving multipass-cavity femtosecond lasers," *J. Opt. Soc. Am. B* **23**, 760-770 (2006).

[175] O. H. Heckl, C. J. Saraceno, C. R. E. Baer, T. S. dmeyer, Y. Y. Wang, Y. Cheng, F. Benabid, and U. Keller, "Temporal pulse compression in a xenon-filled Kagome-type hollow-core photonic crystal fiber at high average power," *Opt. Express* **19**, 19142-19149 (2011).

[176] J. Henningsen and J. Hald, "Dynamics of gas flow in hollow core photonic bandgap fibers," *Appl. Opt.* **47**, 2790-2797 (2008).

[177] E. B. Treacy, "Optical Pulse Compression with Diffraction Gratings," *IEEE J. Quantum Electron.* **5**, 454-458 (1969).

[178] C. Heese, C. R. Phillips, L. Gallmann, M. M. Fejer, and U. Keller, "Ultrabroadband, highly flexible amplifier for ultrashort midinfrared laser pulses based on aperiodically poled Mg:LiNbO₃," *Opt. Lett.* **35**, 2340-2342 (2010).

Curriculum Vitæ

Name: Clara J. Saraceno
Date of Birth: September 13, 1983 (Buenos Aires, Argentina)
Nationality: Argentina, Italy, United States

Education:

Jan. 2009 – Dec. 2012: PhD studies in the group of Prof. Dr. Ursula Keller, Institute of Quantum Electronics, Physics Department, ETH Zurich, Switzerland.
Sept. 2004 – Sept. 2007: Master of Science and “Diplôme d’ingénieur” (Dual diploma), Institut d’Optique Graduate School, Palaiseau, France.
Sept. 2002 – Sept. 2004: Preparation for entrance exams to French engineering schools (“Grandes Ecoles”), Lycée du Parc, Lyon, France.

Research Experience:

Jan. 2009 – Dec. 2012: PhD studies at the Institute of Quantum Electronics, Physics Department, ETH Zurich, Switzerland (development of high-power ultrafast thin-disk lasers).
Sept. 2007 – Sept. 2008: Engineering Trainee in the Ultrafast Laser Division (RLS), Coherent Inc., Santa Clara, California (R&D on ultrafast oscillators based on Ti:Sapphire).
Feb. 2007 – Sept. 2007: Master thesis in the R&D department of Teem Photonics Inc., Grenoble, France (development of a new product based on fiber amplification of nanosecond microchip Q-switched lasers).
May. 2006 – Aug. 2006: Internship in the R&D department of Tenaris Inc., Campana, Argentina. (feasibility of an optical setup for in-situ optical measurement of the temperature of steel in production lines).

Awards and Honors:

Jun. 2012: Department of Physics (ETH Zurich) award for most innovative contribution to the Advanced Physics Laboratory 2012 for the experiment “Solid-state laser”.
Jan. 2012: Best poster award, Advanced Solid State Photonics (ASSP), San Diego, 2012.
Sept. 2002 – Sept. 2007: Awarded two merit scholarships (“Bourse d’Excellence” and “Bourse Major”) by the French Government to pursue studies in France.

Acknowledgements

This thesis wouldn't have been possible without the help of an important number of persons that contributed directly or indirectly to this work.

I believe that one of the key elements to success in a PhD is to have the energy to always stay motivated in spite of so many defeats and frustrations, and to never give up if you believe in your experiment. It appears obvious to me that this is only possible in the context of a certain personal well-being, which can only happen if one is surrounded by people we love. In these lines, I would have to thank such a large number of persons that they would not fit into these few pages, I therefore apologize in advance if anyone is missing in this short list.

I would like to thank Ursi for her never-ending energy for reasearch, for her (sometimes controversial) enthusiasm and her infinite support to my career. In particular, her love for outstanding ultrafast laser technology has been an inspiration.

A big thank you to Patrick Georges, for accepting to be my external co-referee for my PhD exam, and for introducing me to the field of lasers in his inspiring laser technology Masters lecture.

I would also like to thank Thomas for being an important mentor for my career, for teaching me that science works best when it's combined with fun and also for being a good friend. In all my future jobs, I will always have champagne stored to properly celebrate outstanding results.

A very special thank you to the PhD students with which we shared lab work, deadlines, and a few beers: Cyrill and Oli for such a warm welcome into the high-power team, for teaching me everything about the coolest lasers in the world, and in general for being good friends. Working in that lab with you guys really felt like family. A special thank you to Christian Kränkel (the most honest guy I know, and also a good friend) and the whole ILP in Hamburg for a successful collaboration on fantastic thin-disk crystals.

A big thank you to the current PhD students of the thin-disk team: Cinia for her patience and dedication and Florian for the craziest deadline-times in the lab ("là, ça va modelocker, je le sens!"), always ending in MaiTais or Mojitos. I hope you will keep pushing the frontiers of ultrafast oscillators!

Thank you to the VECSEL and high-rep teams for teaching us high-power people that bigger is not always better (in terms of laser cavities): the "old" VECSEL team Aude-Reine, Deran and Beni and the not-so-old VECSEL team Yohan (tandem partner), Martin (...we can simulate it with COMSOL!), Valentin (for always enhancing RF peaks to see what is under the instrument noise level), Siebero (Python pulse propagation master, for the running tips and for being infinitely patient with computer problems), Wolfgang (for so many nice parties and barbeques), Mario (my first semester student!), Christian Zaugg (for his contagious constant good-mood, motivation and nice beer talks), Matthias (for growing all the SESAMs for the cool thin-disk lasers), Bauke (for always staying calm).

Thank you to high-rep team, starting from Max (for showing me that when people speak German slowly, I can understand!), Andi Oehler (Oscar), Selina (for teaching me about frequency combs), and Alex (for his never-exhausting energy to work in the lab, and for many coffees during the weekend at work).

I would also like to thank the high-field group (different members come and gone) for contributing to such a positive and rich research environment: Lukas, Adrian, Matthias, Clemens, Bene, Chris, Reto, Robert, Jens, Mazyar, Sebastian, André, Hiro, Claudio, Matteo, Jochen, Sasha and Cornelia.

Big thanks to Anna for all the nice coffees shared with good advice and positive spirit. Thank you also to Sandra for always making sure everything runs smoothly in the ULP group.

Thanks to my family for always supporting me in every step I have taken until now. None of this would have been possible without their love and support.

Last but not least, thanks to Martin for being such a wonderful life partner. I could never have done it without you.